EAU CLAIRE DE LA LUNE: CLARIFYING THE ORIGIN AND DISTRIBUTION OF WATER ON THE MOON

By Christian J. Tai Udovicic

A Dissertation

Submitted in Partial Fulfillment

of the Requirements for the Degree of

Doctor of Philosophy

in Astronomy and Planetary Science

Northern Arizona University

December 2022

Approved:

Christopher S. Edwards, Ph.D., Chair

Cristina A. Thomas, Ph.D.

Lillian R. Ostrach, Ph.D.

Rebecca R. Ghent, Ph.D.

ABSTRACT

EAU CLAIRE DE LA LUNE: CLARIFYING THE ORIGIN
AND DISTRIBUTION OF WATER ON THE MOON

CHRISTIAN J. TAI UDOVICIC

Water is an essential resource to life as we know it. On the Moon, water is scarce and should not be able to survive on its harsh airless surface. However, several spacecraft measurements and samples returned from the Moon indicate that water exists across the entire lunar surface. There is active debate surrounding the origin, location, and abundance of water on the Moon. Using a three-pronged approach centered on spacecraft observations and computational modeling, the work presented here seeks to answer fundamental questions about where water is found on the Moon and how it got there. One hypothesis suggests that water could be produced by space weathering, the combination of processes that alter the lunar surface due to its exposure to space. I use spacecraft imagery to investigate the rate of space weathering on the Moon to investigate it as a possible source of lunar hydration. I then test whether the spacecraft-observed widespread hydroxyl (OH) / water (H_2O) signature migrates across the surface daily. Finally, I update a simulation of ice delivery to the lunar polar regions to predict where and how deep ancient ice may be buried near the south pole. I find that space weathering alters the lunar surface at a predictable rate for the first 1 billion years of exposure to space. However, the widespread OH / H_2O signature is inherent, or develops on much shorter timescales, and I find no evidence of its daily migration. Finally, I show that the majority of ice that may be buried near the poles has likely been disrupted by impact events and that any remaining ice is most likely 10s to 100s of meters below the surface. I discuss these findings in the context of active and future lunar space exploration. With a new era of lunar exploration on the horizon, the three investigations herein provide key constraints on the origin and distribution of water on the Moon.

Copyright

Acknowledgements

Note: Manuscript-specific acknowledgements are found at the end of each corresponding chapter.

In Memoriam

In memoriam J. L. Bandfield (Space Science Institute) and Nadine G. Barlow (Northern Arizona University).

Land Acknowledgement

All of the work described in this dissertation took place on unceded lands important to many different Indigenous Peoples. In particular, the land at the base of the San Francisco Peaks in so-called Flagstaff, Arizona, USA have been sacred to Indigenous Peoples throughout the region for millenia. An incomplete list of Peoples whose land I completed this dissertation work on include the Havasupai, Hopi, Hualapai, Kaibab Paiute, the Diné (Navajo), San Juan Southern Paiute, Zuni Tribe, Yavapai-Prescott, the Anasazi, the Illini confederation (Kaskaskia, Cahokia, Peoria, Tamaroa, Moingwena, Michigamea, Chepoussa, Chinkoa, Coiracoentanon, Espeminkia, Maroa, Tapouara), Osage, Missouria, Mississaugas of the Credit, Anishnabeg, Chippewa, Haudenosaunee and Wendat peoples. I honor their claim and relationship to the land and encourage all readers in settler colonized nations to research and contribute to Land Back efforts in your area.

Individuals and Groups

I am sincerely grateful to have had numerous kind, loving, and supportive people in my life who have helped me get to this point. If I forgot to mention you, please know that reflects more on my poor memory and I appreciate your contributions nonetheless. First and foremost I thank my partner Allison for the constant encouragement, unwavering support, frequent feedback, and aesthetic eye. I thank my mom Jackie for instilling in me a sense of curiosity and awe at the universe, a sense of pride in my work, and for role modeling how to persist through hardship by carving her own path. I thank my dad Aldo for showing me how much can be achieved through hard work and determination while also prioritizing personal growth,

relationships and service to one's community. Thank you also to my aunt Martina who taught me that there is more to life than work, that being nerdy is cool, and the value of quality time and good food among friends. Thank you to Aldo, Nujat and Ava, Grandma and the whole Tai family, Nonna and the Granzottos for always supporting me and keeping me well fed whenever I visit.

Huge thanks to Christopher for chairing my committee, championing many of my ideas and initiatives while improving them through helpful feedback, and for aiding with the professional and personal challenges of navigating the academy through some particularly tough times. Many thanks also to my committee members: Becky for starting me down the path of planetary and treating me as a collaborator and mentoring me each step of the way, Lillian for the helpful feedback on proposals and projects and for reminding me to strive for better work-life balance, and Cristina for the helpful feedback, support and conversations about life in academia. Thank you to my co-authors who made these projects possible, in particular, Emily, Alissa, Katelyn, Kristen, Tyler, Chris H., and Bill. Thanks to my mentees, Sarah, Johnelle, and Juan, who kept me on track through challenging times and were a joy to work with.

Thank you to Schuyler who has been an immense source of support, feedback, and comraderie throughout my years at NAU. Thank you also to Catherine, Lori, and Chris W. for the constant support, encouragement, work sessions, and feedback. I also thank Aaron for all the help navigating the end of this degree and the helpful feedback on my defense presentation. Thanks to Colin for the helpful chats about high performance computing and this beautiful LaTeXtemplate. Thanks to Shih-Yun and Ryleigh for all the help with the Scientific Programming In Real Life (SPIRL) course. I am also grateful to Patrick, James, Nathan, and Ehren for the food and drinks, and for being great roommates and friends. Thank you to Tony, Audrey, Diego, and DJ for being huge sources of support, inspiration and for being stellar travel, hiking, and climbing buddies. Thanks to Sacha and Roberta, my #1 fans, and to Carter, Kalvin, David, and Phil, Stu, Callie, Liam, and Brian, John Cho and Charlotte, Alexis and Troy, Alex B., Alister, Cailin, Sara, Tasha and Alex V. for all being there for me over the years.

Thanks to the entire Planetary Instrumentation Experimentation and Exploration Laboratory (PIXEL) who have given feedback on papers and presentations along the way, especially Jennifer who has always been a source of great and honest feedback over the years and helped me write my first proposal. Thanks also to the rest of my Department of Astronomy and Planetary Science (DAPS) grad cohort who have helped make grad school more fun and less daunting. I am grateful to Ty for being a great informal mentor and graduate program coordinator and who taught me to write proposals and well enough to have one funded as a grad student. Thank you to Lisa who helped me through my first time as a teaching assistant and who was always genuine, kind and fun to develop curriculum with. Thanks to the DAPS for supporting me through travel funding, and thanks to supporters of the Richard Hayes Memorial Scholarship for supporting my open

science short course, SPIRL. Thank you to Judene and Jagoda for all the seen and unseen administrative work they've done to make this degree possible (Jagoda in particular for going up against a full classroom to ensure I had a place to defend).

And thank you, Josh. We didn't get to work together for long, but your insights, quick witty humor, and friendly disposition are dearly missed. I aspire to one day be a fraction of the scientist and human that you were to so many.

Funding

This material is based upon work supported by the National Aeronautics and Space Administration (NASA) Lunar Data Analysis Program (LDAP) program under grant No. (15-LDAP15_2-0023, PI: Bandfield), the Future Investigators in NASA Earth and Space Science and Technology (FINESST) program under grant No. (80NSSC21K1549, PI: Edwards; FI: Tai Udovicic), and the Exploration Science Summer Internship hosted by Lunar and Planetary Institute (LPI) run by the NASA Solar System Exploration Research Virtual Institute (SSERVI) Center for Lunar Science and Exploration (CLSE) node under grant No. (NNXA14AB07A, PI: Kring).

General Acknowledgements

Several open source software tools developed largely by volunteers and non-profit foundations were used in this work. Most code was developed in the Python programming language (Van Rossum & Drake, 2009). Plots were primarily created using the Python tool `Matplotlib` (Hunter, 2007). Python mathematical and array operations were frequently executed using the Python `NumPy` tool (Harris et al., 2020) and/or stored in Pandas dataframes (Reback et al., 2022). We made use of the `SciPy` Python suite (Virtanen et al., 2020) as well as the `Xarray` Python package (Hoyer & Hamman, 2017) and `Rasterio` (Gillies et al., 2013). Mapping was conducted in QGIS (QGIS, 2021). The KRC thermal model was used to model lunar surface temperatures (Kieffer, 2013). Consider contributing to open source non-profits like NumFOCUS[1] which allow the open source ecosystem to remain free for all users.

[1] https://numfocus.org/

Table of Contents

Abstract ii

Acknowledgements iv

List of Tables ix

List of Figures x

Dedication xvii

Preface xix

1 Introduction 1
- 1.1 The Lunar Surface . . . 2
- 1.2 Space Weathering . . . 4
- 1.3 Lunar Polar Water . . . 6
- 1.4 Widespread Lunar Water . . . 8
- 1.5 Water and Hydroxyl in the Lunar Regolith . . . 11
- 1.6 Methodological Approach . . . 12
- 1.7 Manuscript Summaries . . . 15
- 1.8 Open Science Philosophy . . . 16

2 Manuscript I: New Constraints on the Lunar Optical Space Weathering Rate 19
- 2.1 Abstract . . . 19
- 2.2 Introduction . . . 20
- 2.3 Methods . . . 21
  - 2.3.1 Nanophase and Microphase Iron abundance . . . 23
  - 2.3.2 Crater Populations . . . 23
- 2.4 Results . . . 26
  - 2.4.1 Global Analysis . . . 26
  - 2.4.2 Highlands Analysis . . . 26
- 2.5 Discussion . . . 27
  - 2.5.1 Global Constraints . . . 27
  - 2.5.2 Highlands Constraints . . . 29
  - 2.5.3 A Broken Link Between Nanophase and Microphase Iron Accumulation . . . 30
- 2.6 Conclusions . . . 31
- 2.7 Acknowledgments . . . 32

3 Manuscript II: Roughness Reveals Persistent OH/H_2O on the Moon from Equatorial to High Latitudes 33
- 3.1 Abstract . . . 33
- 3.2 Introduction . . . 34
- 3.3 Methods . . . 35
  - 3.3.1 Roughness Shadowing Model . . . 36
  - 3.3.2 Thermal Model . . . 37

3.3.3 Model Validation Approach . . . 41
3.3.4 Application to M^3 data . . . 41
3.4 Results . . . 42
3.4.1 Model Validation . . . 42
3.4.2 Corrected M^3 Data . . . 44
3.5 Discussion . . . 44
3.5.1 Lunar Surface Roughness and Directional Emissivity . . . 44
3.5.2 Limitations of predicting temperature at 3 µm . . . 46
3.5.3 Comparison with previous 3 µm predictions . . . 48
3.5.4 The nature of widespread lunar OH / H_2O . . . 48
3.6 Conclusions . . . 49
3.7 Open Research . . . 49
3.8 Acknowledgements . . . 50

4 Manuscript III: Buried Ice Deposits in Lunar Polar Cold Traps were Disrupted by Ballistic Sedimentation 51
4.1 Abstract . . . 51
4.2 Introduction . . . 52
4.3 Methods & Modules . . . 55
4.3.1 Main model . . . 55
4.3.2 Ejecta deposition . . . 55
4.3.3 Ballistic sedimentation . . . 57
4.3.4 Impact ice delivery . . . 63
4.3.5 Volcanic ice delivery . . . 65
4.3.6 Solar wind H^+ deposition . . . 65
4.3.7 Ice loss by impact gardening . . . 66
4.3.8 Randomness and reproducibility . . . 67
4.4 Results . . . 68
4.4.1 Effects of ballistic sedimentation . . . 69
4.4.2 Gigaton ice deposits . . . 69
4.4.3 Gardened layer . . . 72
4.5 Discussion . . . 74
4.5.1 Gigaton ice deposit distribution . . . 74
4.5.2 Ice disruption in gardened layers . . . 75
4.5.3 The nature of buried ice below polar cold traps . . . 76
4.5.4 Implications for lunar ice exploration . . . 77
4.6 Conclusion . . . 78
4.7 Open Research . . . 79
4.8 Acknowledgements . . . 79

5 Discussion & Conclusion 81
5.1 Conclusion . . . 84

Acronyms 87

A Supplementary Information for Chapter 2: Manuscript I 89

B Supplementary Information for Chapter 3: Manuscript II 97

C Supplementary Information for Chapter 4: Manuscript III 99

References 105

List of Tables

2.1 The five impact crater databases, the ages they provide, and the final counts used in this study (see Data Sets S1 & S2 for full tables). 25

4.1 Cratering Regimes. Regimes A-E are defined following (Cannon et al., 2020). Regime F, representing basin impactors, was added for this work. 64

B.1 Model parameters used to run surface temperature predictions in KRC. Case-sensitive parameter names correspond to the named parameters in the Davinci KRC interface (https://krc.mars.asu.edu/). 98

List of Figures

1.1 An astronaut footprint photographed with a 70 mm camera during the Apollo 11 mission (NASA Photo AS11-40-5878). 2

1.2 The full Moon photographed on the trip back from the Moon during the Apollo 11 mission. Light toned areas are the lunar highlands, while darker areas are the lunar maria (NASA Photo AS11-44-6667). 3

1.3 Left: A scanning electron microscope image of a lunar agglutinate from Apollo regolith sample 10084 (NASA Photo S87-38811). Right: A scanning electron microscope image of a thin section of a lunar agglutinate. White spots are smFe^0 (NASA Photo S87-38816). Detail of Lunar Sourcebook Figure 7.2 McKay et al. (1972). 4

1.4 Apollo 17 photograph of Bandfield crater, a young 1 km crater on the eastern limb of the Moon. Bright ejecta rays show recently excavated regolith which is still immature, i.e. it has not yet been exposed to space weathering long enough to darken and fade into the background mature regolith (NASA Photo AS17-P-2889). 5

1.5 The south polar region of the Moon as seen by the Lunar Reconnaissance Orbiter Camera (Robinson et al., 2010). Several of the labelled craters, including Shackleton nearest to the pole, contain permanently shadowed regions (PSRs) which remain dark throughout the lunar day. The Lunar Crater Observation and Sensing Satellite (LCROSS) impact site into the Cabeus permanently shadowed region (PSR) is indicated in the upper left quadrant. The NASA Artemis program has targeted 84°–90° S as its target for upcoming human and robotic missions. This mosaic was generated by NASA/GSFC/ASU (`https://www.lroc.asu.edu/posts/237`). 7

1.6 Artist rendition of the LCROSS spacecraft and Centaur rocket shortly after separation (NASA; `https://www.nasa.gov/mission_pages/LCROSS/overview`). The Centaur rocket impact into Cabeus crater in October 2009 provided the first direct evidence of buried water ice at the lunar poles (Colaprete et al., 2010). 9

2.1 Four craters of decreasing model age (descending order) shown in the Lunar Reconnaissance Orbiter Wide Angled Camera 643 nm mosaic, Kaguya Optical Maturity (OMAT) parameter, nanophase iron abundance and microphase iron abundance (left to right; Speyerer et al. 2011; Lemelin et al. 2016; Trang & Lucey 2019). Ejecta annuli extending from each crater rim to 4 crater radii are denoted in green. Mean OMAT, nanophase iron abundance, and microphase iron abundance computed within the annulus are shown in each respective inset as μ_{ejecta}. . . 22

2.2 Box plots of mean nanophase iron (top) and microphase iron (bottom) in the crater annuli of the OMAT (left) and LPI databases (right), grouped by relative age. Cold spot craters are included as a young endmember population. The central orange bar of each population denotes the median and the whiskers denote 1.5*IQR (interquartile range). Circles denote outliers outside 1.5*IQR). Nanophase and microphase iron abundances increase with relative ages of OMAT craters. Copernican craters exhibit a paucity of nanophase iron relative to Eraotsthenian and Imbrian craters, but this contrast is less apparent for microphase iron. . . 24

2.3 Mean abundances of microphase iron (black) and nanophase iron (red) in highlands crater annuli plotted over crater age. **a** Log-log axes and straight-line power law fits. **b** Linear-log axes and straight-line linear-logarithmic fits. Saturation ranges (shaded regions) denote the mean $\pm 1\sigma$ of non-Copernican highlands LPI craters. Ordinary least squares regression fits (Equations 2.1–2.3), prediction intervals and 95% confidence intervals are shown. 28

3.1 Top: Reflected M^3 L1 radiance (black; extrapolated via exponential decay >2.5 µm) and sum of reflected and blackbody emission curves 300–400 K (the 400 K blackbody curve shown in red for reference). Bottom: the same synthetic spectra (solid lines) with a broad 5% absorption feature centered at 3 µm). Errorbars estimated at 10% of radiance (maximum M^3 radiometric uncertainty Green et al. 2011). 35

3.2 Bolometric temperatures (top) and residuals from Diviner (bottom) predicted by the roughness thermal model. Points indicate model predictions while lines and errors indicate global mean and standard deviation Diviner bolometric temperature (Williams et al., 2017). The model may underpredict temperature at low incidence angles ($i \leq 15°ee$; triangles), where Diviner temperatures have been noted to be higher than anticipated (Vasavada et al., 2012), and the model overpredicts at high incidence ($i \geq 70°ee$; squares), where cast shadows are more influential. 38

3.3 Equatorial model predicted (morning, blue; afternoon, orange) over Diviner observed (black) anisothermality (channel 4 – channel 7 brightness temperature;Williams et al. 2017). The roughness thermal model accurately predicts the onset of anisothermal effects with increasing incidence well within Diviner standard deviations. 40

3.4 Residuals of modeled 3 µm brightness temperature from this work and 3 previous studies relative to Diviner 8.25 µm (channel 4) brightness temperature. The roughness thermal model predicts higher brightness temperatures at 3 µm relative to 8.25 µm, consistent with a negative trend in brightness temperature with increasing wavelength (Bandfield et al., 2015). Brightness temperatures computed by three previous M^3 thermal corrections are consistently lower than those predicted here (Clark et al., 2011; Li & Milliken, 2017; Wöhler et al., 2017). . . . 43

3.5 $IBD_{3\mu m}$ at multiple local times in M^3 data thermally corrected by Li & Milliken 2017 (left) and this work (right). Regions with large topographic slopes (>15°) are excluded. Mean spectra across the scene show deeper 3 µm absorptions in roughness-corrected spectra at all local times. 45

3.6 $IBD_{3\mu m}$ from roughness-corrected M^3 spectra averaged across latitude and local time. We find no significant increase in $IBD_{3\mu m}$ with latitude, local time, or solar incidence angle. . . . 46

3.7 Equatorial model-predicted brightness temperatures at 3, 4.5, and 4.85 µm over local time. The surface is nearly isothermal (< 1 K) for incidence angles < 45° in the 4.5–4.85 µm range (black line). However, larger anisothermality is predicted between 4.5 and 3 µm, increasing with incidence (dashed line). 47

4.1 Sequence of events resulting in layered stratigraphy in lunar south pole craters. Greyed out stratigraphy columns indicate that the column/crater does not yet exist. Notice how the presence and thickness of layers change with time as craters are formed and geologic events occur. We do not include ice modification processes in this figure or in the MoonPIES model. 54

4.2 Absolute model ages of craters and basins (inset) incorporated within the MoonPIES model. The ages of polar craters were drawn from Deutsch et al. (2020) and Cannon et al. (2020). Lunar epochs were defined by the ages of the basins, drawn from (Orgel et al., 2018). 56

4.3 Modeled ejecta speed (A), thickness (B), kinetic energy (C), and ballistic mixing depth (D) with distance from primary crater for multiple craters ranging in size from simple to basin-sized impacts. Horizontal dashed lines are present on panels A through C, indicating relevant calculated values for the Bunte Breccia unit of the Ries basin impact structure. 58

4.4 Ballistic sedimentation melt fraction as a function of initial ejecta fraction (f_{ejecta}) and ejecta temperature. Melt fraction is expressed as the mean (upper left) and standard deviation (upper right) cold trap material exceeding 110 K in model simulations, computed over 50 runs with random initial ejecta positions. High temperatures and ejecta fractions result in high melt fractions, as expected. Ranges of melt fractions are indicated for ballistic sedimentation events resulting from craters (blue) and basins (orange, present-cold-moon; red, warm-ancient-moon) modeled in this work. 62

4.5 Cumulative Kinetic Energy (left) from each of the large age-dated craters, excluding basins. The kinetic energy contours are plotted over an average solar illumination map of the south pole (AVGVISIB_75S_120M_201608.LBL; Mazarico et al. 2011). Water ice cold trap extents (right; Landis et al. 2022). 63

4.6 Average ice deposited in each timestep across lunar geologic eras spanned by a MoonPIES model run (log scale). The bars represent the total ice thickness (blue) as well as ice originating from non-basin impactors (orange), basin impactors (green), volcanic (red), and solar wind (yellow). Whiskers denote the maximum and minimum ice delivered in a particular timestep. Shaded regions represent the maximum ballistic sedimentation depth and impact gardening possible in each era, though on average less than this is removed because ballistic sedimentation is sporadic and ejecta layers will preserve ice underlying ice. 66

4.7 A comparison of Fautini, Haworth and Cabeus over 3 different Monte Carlo model runs (all including ballistic sedimentation effects). We note that the cold trap ages and stratigraphic sequence of a particular run differs due to random variation in ejecta ages and ice delivery. Runs A and B show typical columns for all three cold traps. In run C, the large ice layer in Faustini and Haworth is the result of a basin-scale cometary impact, while the absence of layering in Cabeus indicates that it formed later than all possible ejecta sources. 68

4.8 Model stratigraphy columns for the same model run with A) ballistic sedimentation and B) no ballistic sedimentation. When ballistic sedimentation was accounted for, large pure ice layers were lost from the base of the oldest cold traps (Faustini, Haworth and Shoemaker). Shallower layers retain a similar ice % in both cases. Although this is a representative outcome, it should be noted that the absolute quantity of ice and stratigraphic sequence changes from run to run (Figures 4.7-4.9). 70

4.9 Total ice thickness retained across 10,000 runs for each cold trap grouped by geologic era and sorted by latitude. The width of each violin is scaled by the total number of runs retaining at least 1 m of ice. Median and quartiles are indicated as dashed lines. Without ballistic sedimentation, total ice thickness is greater, particularly for Pre-Nectarian and Nectarian cold traps. The difference in ice retention is smaller for Imbrian cold traps where few basins and local impacts disturb ice. About 1000 runs retained > 1 m for Wiechert J and only 3 runs retained > 1 m of ice in Shackleton. 71

4.10 Thickness of ice layers with depth for 10,000 model runs, represented as kernel density estimation (KDE) contour plots for Faustini, Haworth, Amundsen, Cabeus, de Gerlache, and Slater craters. Blue contours represent model runs without ballistic sedimentation, and brown contours represent model runs with ballistic sedimentation and contour centers represent the most likely thicknesses with depth. Shaded regions indicate "gigaton" zones, where layer thickness exceeds 10 m. For Cabeus, horizontal lines denote LCROSS maximum excavation depth (Schultz et al., 2010; Luchsinger et al., 2021). 73

4.11 Boxplot of ice retained in each modeled cold trap to a depth of 6 m (the LCROSS impact is thought to have excavated 6–10 m into Cabeus crater; Schultz et al. 2010; Luchsinger et al. 2021). Boxes denote the first and third quartiles and whiskers denote the 99th percentile. Points denote outliers above the 99th percentile value. At least 75% of runs predicted 0 m ice retention in the upper 6 m for all cold traps except Faustini and de Gerlache. 75

A.1 Distribution of dated highlands craters in our sample shown on the Lunar Reconnaissance Orbiter (LRO) Wide Angle Camera (WAC) mosaic (Speyerer et al., 2011). Stacked histograms show the number of cold spot, chronology, and rocky highlands craters in each 20^o longitude bin (top) and each 15^o latitude bin (right). 91

A.2 Linear-linear axis plots of fits in Fig. 3. **a** Power law fits in Fig. 3a shown on linear axes. **b** Logarithmic fits in Fig. 3b shown on linear axes. 92

A.3 We test the influence of ejecta anomalies on the mean annular nanophase and microphase iron of four craters. We find that digitizing asymmetric ejecta and excluding small superposed craters may reduce the mean and standard error nanophase iron of smaller craters in our sample. Digitizing ejecta anomalies of larger craters appears to have negligible effects. 93

A.4 We test the influence of craters with asymmetric ejecta on our logarithmic fits (Fig. 3b). We plot in purple the 7/75 asymmetric ejecta craters in our highlands sample (9%); 0 are chronology craters, 2/12 are cold spot craters (17%), and 5/75 are rock abundance craters (9%). We note that nanophase and microphase iron of asymmetric ejecta craters systematically plot above our fits, consistent with the ejecta annulus incorporating mature background material in these cases. Despite being systematically enhanced, the overall effect of removing these points is negligible and the new fits are well within the 95% confidence intervals of the presented in Fig. 3b. 94

A.5 Studentized residuals of the linear-logarithmic fits (Fig. 3b) with longitude, latitude, crater radius, and age. We observe no systematic bias in the residuals of our fit with location, crater size, or age. 95

C.1 Ballistic hop efficiency for each cold trap in this work. Blue points are values reported by Moores (2016) and orange squares are those derived here. The average value used in Cannon et al. (2020) is shown in gray. 101

C.2 Comet velocities drawn from bimodal distribution approximating speeds and relative abundances of Jupiter Family Comets and Oort Cloud Comets (Ong et al., 2010). 102

C.3 Mass of impactor retained on the lunar surface vs impact speed from simulations by Ong et al. (2010). The best fit power law is $1.66 \times 10^4 v^{-4.16}$ (excluding the reported outlier at 60 km/s). Our model is insensitive to to the fit at high velocity since high velocity impacts are rare in the model (see Figure C.2) and these velocities correspond to smaller impactors which deliver less ice. Asteroid retention is capped at 50% for consistency with the previous model by Cannon et al. (2020) while comets never have less than 10 km/s. 103

C.4 Ice delivered by asteroidal (grey) and cometary (blue) basins in each 10 Myr timestep over 500 runs. A 30 Myr moving window average (solid) and 99.7th percentile (dashed) show typical and 3 σ basin ice at each timestep. 104

Dedication

For me. And for you. And for every implausible instant it took to get these words from me to you.

Preface

This dissertation consists of five chapters: Introduction (chapter 1), three manuscript chapters (chapter 2, chapter 3, chapter 4), and the Discussion & Conclusion (chapter 5). Chapters 2–4 were prepared as manuscripts to appear in peer-reviewed scientific journals. As of this writing, *Manuscript I: New Constraints on the Lunar Optical Space Weathering Rate* was published as Tai Udovicic et al. (2021a) in Geophysical Research Letters (doi: `https://doi.org/10.1029/2020GL092198`), chapter *Manuscript III: Buried Ice Deposits in Lunar Polar Cold Traps were Disrupted by Ballistic Sedimentation* was recently submitted to a journal for peer review, and chapter *Manuscript II: Roughness Reveals Persistent OH/H_2O on the Moon from Equatorial to High Latitudes* is being prepared for submission. During the review process, the contents of Manuscript II and III may change such that their published versions differ from the contents of chapter 3 and chapter 4, respectively. Additionally, there may be some redundancy in the contents of the three manuscript chapters which were written to appear as standalone works in the literature.

Chapter 1

Introduction

Water is essential to life as we know it. Thus far, Earth is unique in its water diversity, being the only Solar System object where water naturally exists on the surface and in the atmosphere in its three main phases: ice (solid), water (liquid), and vapor (gas). However, as we explore more of the Solar System, we continue to find water in a variety of phases and in unexpected places. Water ice is found at the poles of Mercury, water vapor erupts from Enceladus in plumes, and a liquid water mantle on Pluto likely drives the motion of its icy crust. Once thought a rarity, we now know that water was one of the first molecules that formed in the outer Solar System 4.5 billion years ago. As the planets formed and migrated to their current positions, icy asteroids and comets were flung throughout the Solar System, from Mercury to the furthest reaches of the Oort Cloud. These icy projectiles are thought to have delivered most of the water on Earth and, as our closest neighbor, the Moon would have accumulated a significant amount of water as well. Unfortunately, the Moon lacks a protective atmosphere and global magnetic field to protect its water from rapidly escaping to space and is therefore mostly dry. However, interest in lunar water has surged in the last decade following the discovery of buried water ice revealed by the first impact experiment into a lunar crater near the south pole. Recent spacecraft missions have also revealed surprising water signatures in direct sunlight across most of the lunar surface where it should be much too warm for surface water to survive for long. As a result, there is now significant debate about how much water exists on the harsh lunar surface, how it survives, and where it originated. Tracking down the source of the lunar water could help us understand how water came to be so abundant on Earth. Determining the location and abundance of water on the Moon could revolutionize space exploration since the hydrogen and oxygen that make up H_2O can be repurposed as rocket propellant, making the Moon a potential launchpad for further space exploration. As we prepare to return humans to the Moon for the first time in five decades, it is critical to understand how much water is on the Moon and where it is located.

Fundamental unanswered questions about water on the Moon could be keys to understanding the history of water on Earth, while preparing us for future exploration in space. *Did lunar water come from the same*

source as water on Earth? How much water is on the Moon and can it be used in future human exploration? Is lunar water restricted to the polar regions or is it spread across the entire surface? In this dissertation, I sought to answer these questions to better understand the origin and abundance of water on the lunar surface. With a wealth of recent spacecraft imagery of the Moon combined with unprecedented ease of access to computation power, it is now possible to study the lunar surface in greater detail and with much greater data volumes than ever before. In this work, I combine spacecraft observations, computational modeling, and statistical analysis to explore key outstanding mysteries about water on the Moon.

1.1 The Lunar Surface

The lunar surface is an excellent laboratory for understanding the historical and present-day space environment in the Earth's planetary neighborhood. The Moon lacks many of the major drivers of surface change that are encountered on Earth, including liquid water, wind, plate tectonics, and it has not seen major volcanic activity for many millions to billions of years. As such, the heavily cratered lunar surface is an alien landscape compared to Earth, where terrestrial erosion and crustal recycling over billions of years have erased nearly all evidence of impact craters. Global change on the Moon is primarily due to its lack of a protective atmosphere and global magnetic field, leaving its surface exposed to solar irradiation and meteor impacts which have shaped on the surface over time. Over billions of years of meteor impacts, the rocky lunar crust has been pulverized into tiny rock fragments known in aggregate as *regolith*. The lunar regolith blankets virtually the entire surface and is estimated to be at least several meters thick globally. Individual grains of regolith are typically less than 1 mm in size, with most being less than 100 µm, making these rock fragments even finer than household baking flour (∼200 µm). Regolith grains are irregularly shaped and loosely stacked, making the lunar surface very low in density. It is also highly compressible, meaning an astronaut's boot easily makes a footprint, but does not sink through (Figure 1.1). Though it appears visually similar to terrestrial soil, lunar regolith has no organic material or soil moisture, making it a unique material with different physical

Figure 1.1: An astronaut footprint photographed with a 70 mm camera during the Apollo 11 mission (NASA Photo AS11-40-5878).

properties than any dust, sand or rock found on Earth. In this work, unique regolith optical properties (how it interacts with visible light) are central to using spacecraft observations to understand how quickly the regolith evolves over time (chapter 2). Accounting for unique regolith thermal properties is also critical to understanding global lunar water signatures (chapter 3) and to estimate the amount of heat required to melt ice during impact events at the poles (chapter 4).

Figure 1.2: The full Moon photographed on the trip back from the Moon during the Apollo 11 mission. Light toned areas are the lunar highlands, while darker areas are the lunar maria (NASA Photo AS11-44-6667).

The lunar regolith can be divided into two main types which are found in the two primary terrains on the Moon, the *highlands* and the *maria*. Easily identifiable by-eye on a clear night, the lunar highlands are the lighter-toned (higher albedo) parts of the surface which represent the original lunar crust (c. 4.3 Ga; Figure 1.2). Early in lunar history, a global magma ocean covered the entire surface and its slow cooling led to lighter-toned, less dense minerals crystallizing early and floating to the surface to form the lighter rocks of the lunar highlands. Highlands rock is primarily anorthosite which is described as *felsic* due to its high silica content. Lunar anorthosite contains minerals like the calcium-aluminum silicate anorthite (the calcium-rich variety of plagioclase), and the iron-magnesium silicates orthopyroxine and olivine. By contrast, the maria are the darker (lower albedo) regions of the Moon that formed from denser magma which erupted onto the surface after the highlands crust was formed (c. 3.2–2.8 Ga; Figure 1.2). The maria are composed of basalt which is *mafic* due to its lower silica content. Like the highlands, mare basalts also contain anorthite and olivine, but they differ in their inclusion of clinopyroxine (a calcium-iron-magnesium silicate) and the addition of the dark iron-titanium oxides, ilmenite and spinel. Since iron absorbs large amounts of visible light, relatively small amounts of ilmenite and spinel cause basalt to be much darker than anorthosite, allowing us to tell the lighter highlands from the darker maria at a glance. The availability of iron in the regolith also determines how quickly the regolith is altered by space weathering, which is discussed in chapter 2.

1.2 Space Weathering

Space weathering describes how airless surfaces are continuously altered due to their direct exposure to space. The main space weathering processes on the Moon are solar wind irradiation, micrometeorite bombardment, and galactic cosmic radiation. Space weathering operates at the regolith grain scale (<10s of micrometers), where micrometeorites can melt and vaporize individual crystalline mineral grains which then rapidly cool into non-crystalline (amorphous) glass or weld together into heterogenous agglutinates (Figure 1.3). The solar wind can alter regolith grains on the molecular level, removing atoms and molecules through sputtering while implanting hydrogen and helium ions that can react with or become trapped in irregular crystal defect sites introduced by space weathering. Galactic cosmic rays penetrate deeper into the surface, leaving tracks of damage to crystalline mineral grains encountered along the way. Samples collected on the Moon during the Apollo missions have been dated by the number of cosmic ray tracks visible in the regolith, a proxy for exposure time near the surface. When sorted by cosmic ray exposure age, predictable trends in regolith optical properties emerge.

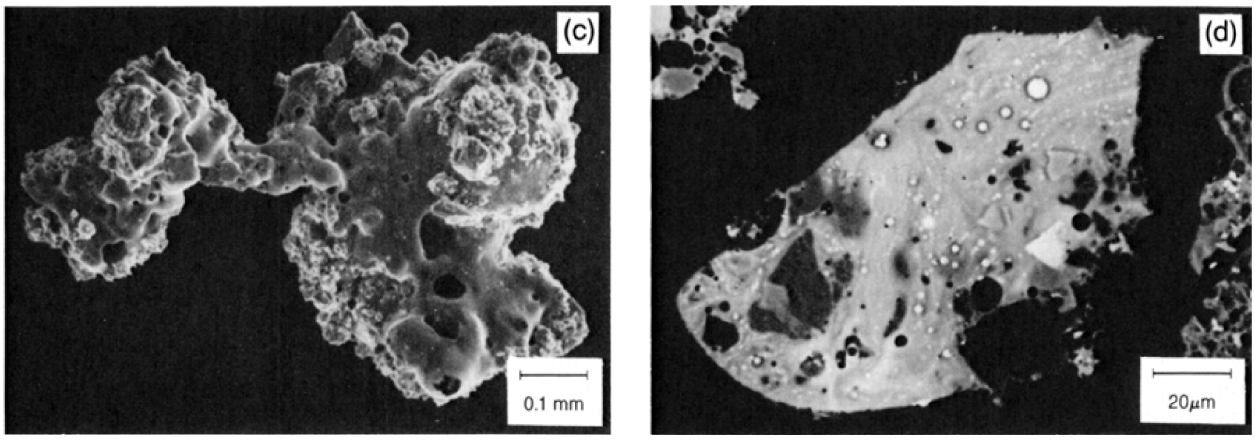

Figure 1.3: Left: A scanning electron microscope image of a lunar agglutinate from Apollo regolith sample 10084 (NASA Photo S87-38811). Right: A scanning electron microscope image of a thin section of a lunar agglutinate. White spots are $smFe^0$ (NASA Photo S87-38816). Detail of Lunar Sourcebook Figure 7.2 McKay et al. (1972).

Regolith optical properties change as a function of surface exposure age from *immature* (younger) to *mature* (older). Mature regolith has been at or near the sufrace the longest and tends to be lower in albedo (reflectivity), causing it to appear darker than immature regolith. Mature regolith also has a "redder" spectral slope (lower reflectance at lower wavelength) than immature regolith in the visible to near-infrared part of the spectrum. These changes in optical properties are attributed to the formation of small particles of pure iron known as submicroscopic iron ($smFe^0$). Ranging in size from nanophase iron (<40 nm) to microphase iron (40 nm–1 μm), these tiny iron particles can be found on the rims of individual regolith

grains or in heavily melted and glassy agglutinates (Figure 1.3). Despite their small size, these particles drastically change the appearance of the lunar surface to the extent that their effects are visible with the naked eye. When looking at the lunar surface, bright rays around lunar craters are due to immature regolith being excavated from the shielded subsurface and spreading over top of the darker, mature regolith which blankets most of the lunar surface (Figure 1.4). Over time, space weathering produces $smFe^0$ in the newly exposed immature regolith, causing the rays to gradually fade into the background mature regolith. The accumulation of $smFe^0$ is observable in optical spacecraft data and the gradual maturation of regolith excavated near young lunar craters is used to track the rate of space weathering in chapter 2.

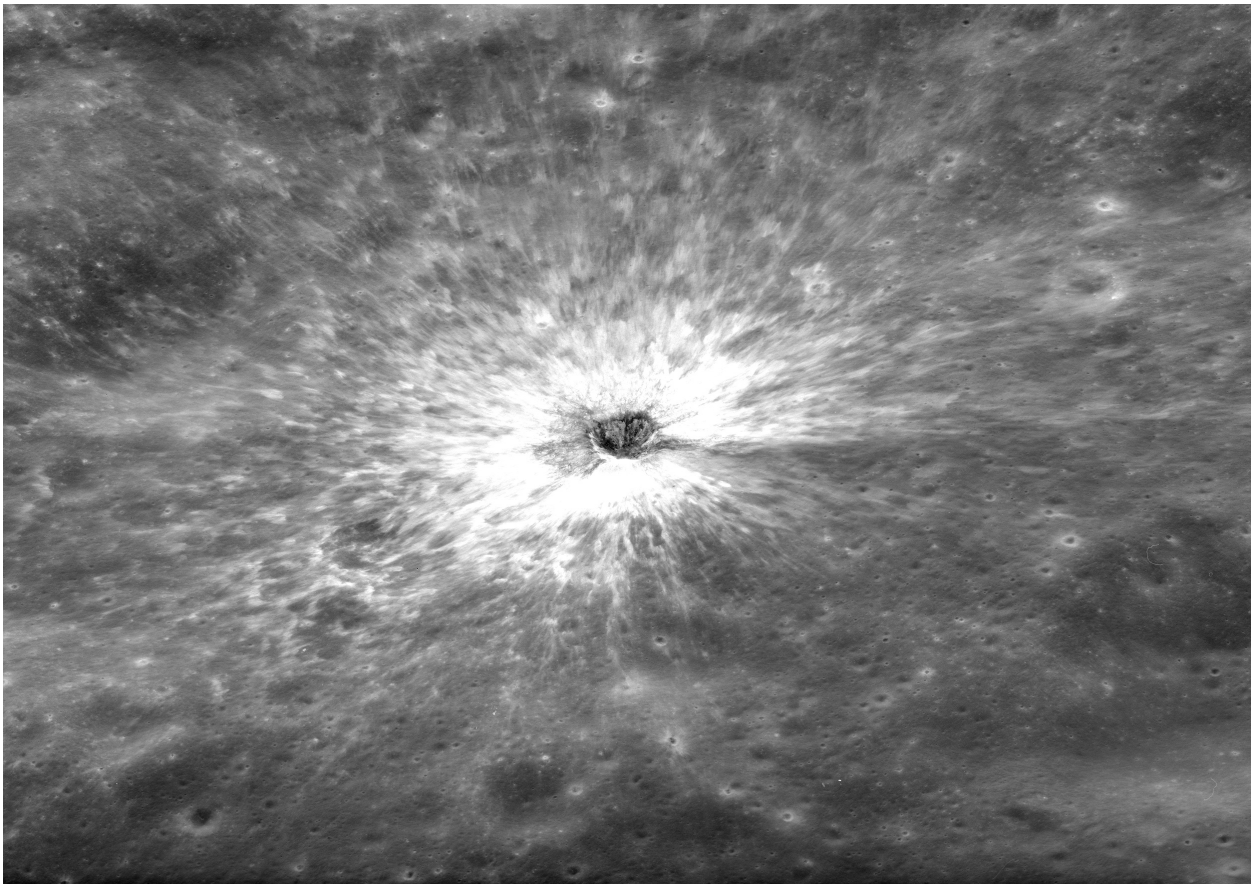

Figure 1.4: Apollo 17 photograph of Bandfield crater, a young 1 km crater on the eastern limb of the Moon. Bright ejecta rays show recently excavated regolith which is still immature, i.e. it has not yet been exposed to space weathering long enough to darken and fade into the background mature regolith (NASA Photo AS17-P-2889).

1.3 Lunar Polar Water

Although the Moon is mostly devoid of water (H_2O), several independent investigations have found direct evidence for H_2O within cold permanently shadowed regions at the lunar poles. Unlike the Earth, the Moon has very little axial tilt (obliquity $\sim$6.7°) and negligible precession, therefore the Sun rises directly above the lunar equator ($\pm$6.7° latitude), regardless of the season. This means that the lunar poles never point directly towards or away from the Sun. From the perspective of the poles, the Sun remains low on the horizon throughout the lunar day. A steep-sided, roughly circular impact crater near the pole will cast a shadow on its own floor regardless of the time of day or season. We call this type of area a permanently shadowed region (PSR) since it never receives direct sunlight.

Surprisingly, shadows on the Moon are much darker and much colder than shadows we typically find on Earth. This is due to the lack of atmosphere which scatters some light and transfers some heat into shadows on Earth. Without atmospheric scattering, there is a complete lack of sunlight s (except perhaps light scattered off nearby lit surfaces), allowing PSRs to remain very cold. The Diviner Lunar Radiometer aboard the Lunar Reconnaissance Orbiter (LRO) has measured PSR temperatures as low as 60 K (-213° C), among the lowest temperatures ever recorded in nature (Paige et al., 2010a). Since PSRs remain very cold for very long periods of time - perhaps millions to billions of years - they have long been hypothesized to host water ice. Any water vapor encountering the extremely cold PSR temperatures would immediately condense into ice and become trapped since the temperatures never rise high enough to re-vaporize the ice. Regions which are permanently too cold to allow water or other volatiles to escape are called cold traps and these lunar cold traps have long been studied as potential hosts of lunar water ice (Watson et al., 1961; Arnold, 1979). It was then surprising when radar observations of the lunar poles failed to find any evidence of ice (Stacy et al., 1997; Campbell et al., 2006), especially given that massive polar ice deposits are found on Mercury (Moses et al., 1999), where the airless surface conditions are similar to those of the Moon.

In the intervening years, new evidence from several direct and indirect methods of detecting water have confirmed that water exists at the surface of polar PSR cold traps, but in much smaller quantities than at the poles of Mercury. Spacecraft observations using visible to near-infrared spectroscopy (Li et al., 2018), ultraviolet spectroscopy (Gladstone et al., 2012; Hayne et al., 2015), albedo (Fisher et al., 2017), and neutron spectroscopy (Miller et al., 2012; Lawrence et al., 2006) showed signatures associated with trace amounts of H_2O or enhanced hydrogen on PSR surfaces. However, the surface ice detected in these studies is patchy and much less extensive than the deposits found at the poles of Mercury. Recent studies have suggested that H_2O is removed from PSRs much more quickly than it is delivered which may explain their patchy appearance. For example, ice can be eroded due to space weathering due to the deflection of the solar wind into PSRs,

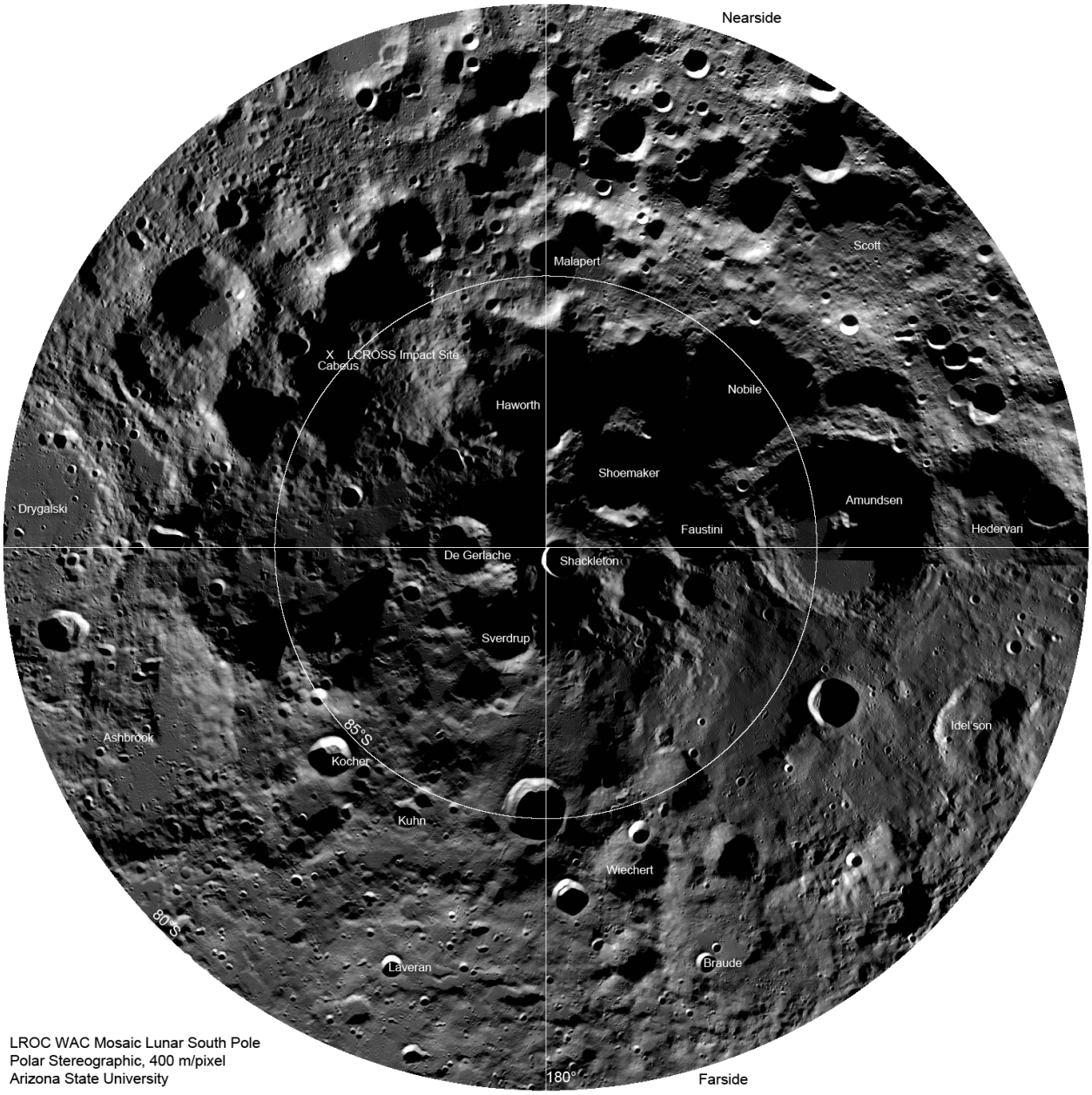

Figure 1.5: The south polar region of the Moon as seen by the Lunar Reconnaissance Orbiter Camera (Robinson et al., 2010). Several of the labelled craters, including Shackleton nearest to the pole, contain permanently shadowed regions (PSRs) which remain dark throughout the lunar day. The Lunar Crater Observation and Sensing Satellite (LCROSS) impact site into the Cabeus PSR is indicated in the upper left quadrant. The NASA Artemis program has targeted 84°–90° S as its target for upcoming human and robotic missions. This mosaic was generated by NASA/GSFC/ASU (`https://www.lroc.asu.edu/posts/237`).

or by micrometeorite bombardment which affects the lunar surface from all directions (Farrell et al., 2019). Additionally, impact gardening, the continual churning of the regolith by impacts of all sizes, is thought to expose buried ice much more quickly than it buries it, exposing it to surface erosion (Costello et al., 2021). While these processes may explain the lack of ice in lunar PSRs, the massive ice deposits at Mercury remain a mystery. Some have suggested that a comet or hydrated asteroid impact at Mercury filled its poles with ice relatively recently and that they will eventually fade to the patchy state that we observe on the Moon (Deutsch et al., 2019). Alternatively, it is possible that the lunar PSRs are younger than previously thought and that the Moon experienced a large swing in its obliquity as it approached its current stable orbit (Siegler et al., 2015; Farhat et al., 2022). If this is the case, ancient water ice delivered early in lunar history would have been quickly lost to space with no permanently shadowed cold traps to store it.

Since there appear to be no massive surface ice deposits at the lunar poles, recent studies have begun the search for ice in the subsurface. Direct evidence for buried water ice came during the Lunar Crater Observation and Sensing Satellite (LCROSS) experiment (Schultz et al., 2010) which impacted a used rocket booster into Cabeus crater, a PSR near the lunar south pole (Figure 1.6). The impact ejecta plume contained a quantity of H_2O consistent with 150 kg water ice buried up to 6–10 m below the PSR (Colaprete et al., 2010; Luchsinger et al., 2021). Other studies have used indirect means to detect buried ice more broadly using surface elevation and roughness data (Deutsch et al., 2020), crater shape (Rubanenko et al., 2019) and updated orbital radar measurements (Spudis et al., 2013; Patterson et al., 2017). While these studies found signs of buried ice, it is still unclear what quantity of ice is buried below the PSRs and at what depths. To attempt to answer this question, Cannon et al. (2020) developed a computational model which tracked the sources of ice throughout lunar history and their delivery to individual cold traps. This model accounted for gradual loss of ice at the surface, but allowed ice to be buried and preserved beneath the ejecta of nearby impact craters. Their results showed potential for very large ice deposits at depth below several PSRs, with size estimates in the gigatons. In chapter 4, I update the Cannon et al. (2020) model with several key processes and more recent estimates of ice delivery and loss rates. With my updated model, I predict the location, depth, and quantity of water ice in PSR cold traps in the lunar south polar region.

1.4 Widespread Lunar Water

Outside the PSRs, the vast majority of the lunar surface experiences large daily temperature swings, with typical daytime temperatures in the range of 300–400 K, much warmer than the sub-110 K temperatures needed to trap water ice at the extremely low surface pressures on the Moon (Schorghofer & Williams, 2020; Landis et al., 2022). It was then surprising when three independent spacecraft discovered evidence of water on

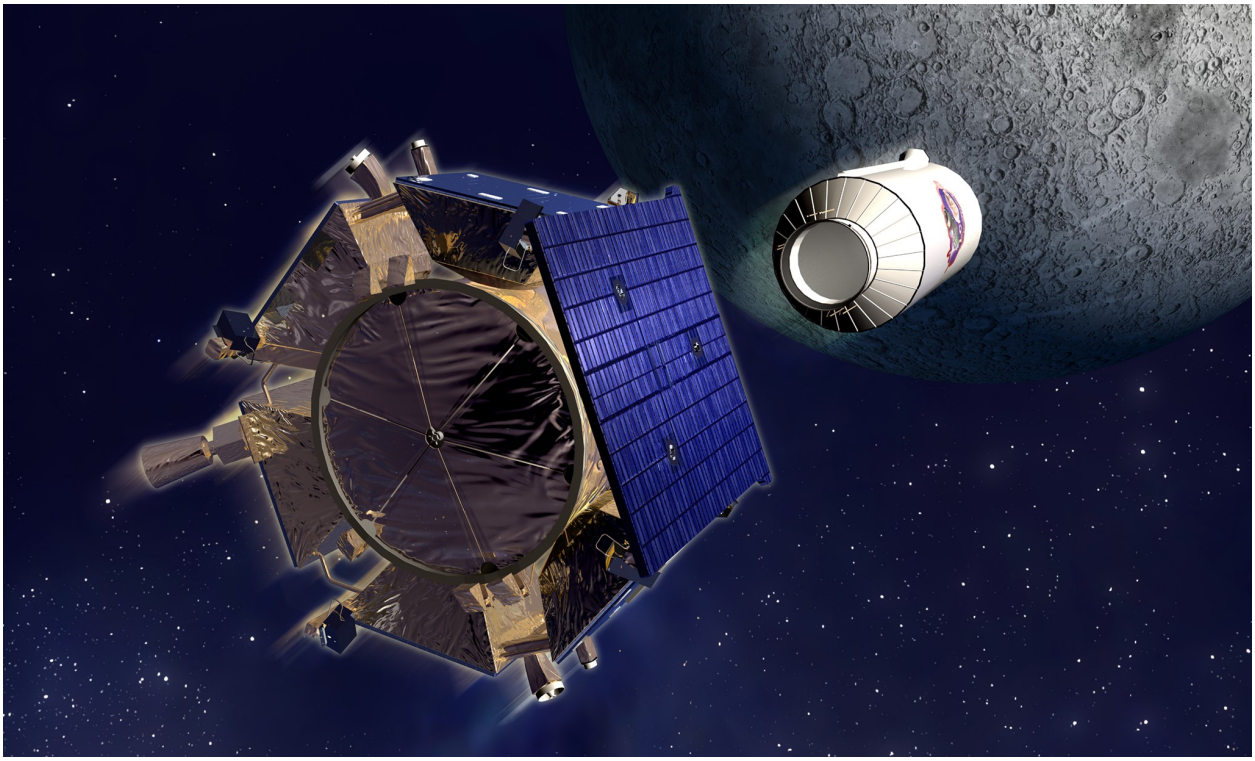

Figure 1.6: Artist rendition of the LCROSS spacecraft and Centaur rocket shortly after separation (NASA; `https://www.nasa.gov/mission_pages/LCROSS/overview`). The Centaur rocket impact into Cabeus crater in October 2009 provided the first direct evidence of buried water ice at the lunar poles (Colaprete et al., 2010).

the daylit side of the Moon. Referred to here as the *widespread* lunar water signature, it was detected by the Deep Impact extended mission (EPOXI), the Moon Mineralogy Mapper (M^3) instrument aboard the Indian Space Research Organisation (ISRO) Chandrayaan-1 spacecraft, and Cassini during a fly-by on its way to Saturn (Sunshine et al., 2009; Pieters et al., 2009; Clark et al., 2011). The three spacecraft observed the Moon with near-infrared spectrometers, specifically at a wavelengths of 2.8 µm and 3 µm, where hydroxyl (OH) and water (H_2O) tend to absorb light, respectively (Farmer, 1974). All three spacecraft observed a dip in near-infrared reflectance in the 2.8–3 µm region, consistent with OH / H_2O on the lunar surface. However, these observations were unable to distinguish OH from H_2O since the 2.8 µm and 3 µm features can overlap when OH / H_2O is attached to various metals in the poorly crystalline lunar surface (Stolper, 1982; Starukhina, 2001; McIntosh et al., 2017; McLain et al., 2021). However, these observations were suggested to be water rather than hydroxyl based on the diurnal variation in the 2.8–3 µm feature; the feature was concentrated in the early morning, late afternoon, and at high latitudes where the surface is cooler. The implication was that water on the lunar surface could be heated off of the surface during the day and then migrate until it reached somewhere cooler to come to rest. These observations were later corroborated by

observations by the Lyman Alpha Mapping Project (LAMP) mission which also showed diurnal variation of far-UV spectra associated with hydration (Hendrix et al., 2019). The prospect of daily migrating water was exciting due to the relative ease with which future missions could extract and possibly use it - simply expose regolith to sunlight in the morning and collect the water that emerges. However, these observations have been debated in the intervening years and the source of the widespread lunar OH / H_2O feature is still an open question.

Interpreting the 2.8–3 µm feature is particularly challenging on the Moon due to the unique lunar thermal environment. The near-infrared part of the spectrum marks a transition from primarily reflected solar light to primarily thermally emitted radiation, which are approximately equal in magnitude at lunar daytime temperatures (see chapter 3, Figure 3.1). To accurately interpret the 2.8–3 µm reflectance feature, the thermal emission (governed by surface temperature) must be removed from the spectrum. If the surface temperature is over-predicted or under-predicted, the apparant shape and size of the 2.8–3 µm OH / H_2O feature can vary drastically. This is why several follow-up investigations of the widespread OH / H_2O feature have conflicted in their interpretation of the 2.8–3 µm signature, with some reporting daily migrating H_2O (Li & Milliken, 2017), completely stationary OH (Bandfield et al., 2018), and some combination of static and migrating OH / H_2O (Wöhler et al., 2017). In chapter 3, I discuss how the roughness of the lunar surface is a further complicating factor influencing the widespread OH / H_2O feature and present a thermal model capable of predicting 2.8–3 µm temperatures while accounting for roughness.

More recently, new observations of the Moon in the infrared have shown diagnostic evidence of H_2O (and not just OH) widespread on the sunlit lunar surface. These observations were collected by the Earth-based Stratospheric Observatory for Infrared Astronomy (SOFIA) mission, a Boeing 747SP airplane with a mounted infrared telescope capable of taking high altitude observations where the atmosphere is thin and water vapor is less likely to bias measurements (Young et al., 2012). Using this telescope to observe the Moon, Honniball et al. (2020) found unambiguous evidence of H_2O on the daylit lunar surface. These observations used the infrared 6 µm emission feature which is only associated with H_2O and not OH. Multiple SOFIA observations at different local times have shown that the H_2O content remains static throughout the lunar day (Honniball et al., 2022). Taken in combination with the previous observations at 2.8–3 µm, it appears that at least some or all of the widespread OH / H_2O feature is due to H_2O. However, the mounting evidence that OH / H_2O can survive the harsh lunar thermal and space weathering environment raises important questions about how these molecules are so strongly attached to the surface or sequestered in individual regolith grains.

1.5 Water and Hydroxyl in the Lunar Regolith

While no samples have yet been collected from the lunar polar regions, the Apollo sample collection and laboratory experiments on regolith analogs yield clues about the source(s) of the widespread OH / H_2O feature. Several sample studies have found OH / H_2O trapped in primary minerals of the lunar crust or in volcanic glasses. These observations suggest an "endogenic" source (i.e., from the lunar interior; McCubbin et al. 2010; Saal et al. 2008; Liu et al. 2022). In particular, the recent surface observations and samples returned by the Chang'E 5 mission show a compelling link between the OH / H_2O feature observed on the surface and hydroxylated apatite grains, suggesting the widespread "water" feature is best explained by hydroxyl (OH) from indigenous sources. However, other sample studies have found OH and H_2O signatures associated with "exogenic" sources like space weathering. An early study by Housley et al. (1973) proposed that micrometeorite bombardment would liberate oxygen from minerals, producing similar amounts of $smFe^0$ and H_2O in the regolith. Recent observations of lunar regolith samples returned by the Apollo missions found that micrometeorite bombardment can trap OH in impact glasses, but the link to $smFe^0$ is unclear (Liu et al., 2012). That study also found evidence that the OH in glassy agglutinates is linked to the solar wind, indicating that both major space weathering processes (micrometeorite bombardment and solar wind irradiation) could play a role in trapping OH on the lunar surface. Several processes have also been shown to produce or liberate H_2O from regolith analogs. For example, dry regolith analogs irradiated with solar wind ions release water when heated by micrometeorite-like laser pulses (Zhu et al., 2019). A related experiment showed that trace amounts of OH and H_2O are trapped within the solar wind irradiated coatings of individual lunar regolith grains, suggesting that the solar wind can sequester OH / H_2O independently of micrometeorite bombardment (Bradley et al., 2014). Other laboratory experiments on regolith analogs have shown that the solar wind can damage the crystal structure of lunar minerals, producing sites where solar wind hydrogen can react and form OH bonds within crystal defect sites (Igami et al., 2021). Each of these formation mechanisms suggest that space weathering could be an important process in the generation of surface OH / H_2O, and could contribute to the widespread 2.8–3 µm feature. At present, it is unclear if endogenic or exogenic sources dominate lunar OH / H_2O or how much H_2O, if any, is liberated from the surface on human timescales. By constraining the rate that space weathering alters the lunar regolith in chapter 2 and the variability of the 2.8–3 µm OH / H_2O in chapter 3, I investigate the source, distribution, and daily behavior of water on the lunar surface.

1.6 Methodological Approach

Note: Each manuscript chapter contains detailed descriptions of methods used for the work therein. Here, I provide a brief summary of the primary data and methods used in this work.

Core questions about lunar water remain unanswered, but an abundance of data from many recent spacecraft missions present an opportunity to glean new insights. In this work, I use spacecraft data from three different instruments on three separate spacecraft which each imaged the Moon in distinct wavelengths of light. In chapter 2, I use global maps of the lunar surface derived from the Japan Aerospace Exploration Agency (JAXA) SELenological and ENgineering Explorer (SELENE) spacecraft, also known as Kaguya, which orbited the Moon in 2009. Among its instruments was the Multiband Imager (MI), a 9-band imaging camera that measured reflected light from the lunar surface in the visible to near-infrared (0.415–1.55 µm; Ohtake et al. 2008). As noted in §1.2, the space weathering product submicroscopic iron ($smFe^0$) darkens and reddens lunar reflectance spectra in the visible to near-infrared and these changes were apparent in Kaguya MI spectra. Using a Hapke radiative transfer model (Hapke, 2001) that tracks the behavior of light reflected from a simulated surface, Trang & Lucey (2019) were able to show that adding $smFe^0$ particles to the model resulted in simulated spectra similar to those observed by the Kaguya MI. Furthermore, they showed that their simulated spectra improved when two different sizes of $smFe^0$, nanophase iron (< 40 nm) and microphase iron (> 40 nm), were incorporated into their Hapke model (Trang & Lucey, 2019). By varying the abundance of nanophase and microphase iron in the model, Trang & Lucey (2019) determined how much $smFe^0$ was needed to reproduce each spectrum observed by the Kaguya MI. They then translated these abundances into global nanophase and microphase iron abundance maps. These maps were the first of their kind to relate the optical effects of space weathering to quantities of physical particles on the surface produced by space weathering. Visually, the Trang & Lucey (2019) $smFe^0$ maps appeared to be well-correlated with surface exposure to space weathering; young crater rays are depleted in $smFe^0$, while ancient terrains were saturated in it. Using these maps, I explored the rate that $smFe^0$ has accumulated in the lunar surface over the past 1 Ga (chapter 2). Although our understanding of the nature and formation of OH / H_2O is still evolving, many studies point to space weathering as a likely source (§1.5). Therefore, even if H_2O is not a byproduct of $smFe^0$ formation as suggested by Housley et al. (1973), determining the rate of space weathering in the lunar surface can place useful constraints on the active formation of lunar OH / H_2O.

To investigate the abundance and behavior of OH / H_2O on the lunar surface directly, I used two other spacecraft data sets. The M^3 instrument was a NASA contributed instrument to the ISRO Chandrayaan-1 spacecraft which orbited the Moon from 2008–2009 (Pieters et al., 2009; Goswami & Annadurai, 2009). M^3

took spectral measurements of the surface from 0.42–3.0 µm in 86 or 256 channels, depending on its operating mode. These high spectral resolution observations were developed to precisely measure slight differences in mineralogy across the lunar surface. However, the detection of a OH / H_2O signature near 2.8–3 µm came as a surprise, but was quickly validated by two other spacecraft around the same time (see §1.4). While it was clear that some amount of OH / H_2O was being detected, it was challenging to characterize its behavior for several reasons. For example, since the spectrometer was not designed with a broad 3 µm feature in mind, M^3 was only able to measure the onset of the dip in reflectance from 2.8–3 µm. However, it was clear from the data and from longer wavelength observations during the Cassini flyby (Clark, 2009) that the feature extends longer than 3 µm, making it impossible to discern the true depth and width of the feature from M^3 data alone. Also, daytime temperatures of the lunar surface cause near-infrared surface emission similar in strength to the reflectance at 3 µm, which could fully mask an absorption feature if not properly compensated (Figure 3.1). The emission of the lunar surface is further confounded by the fact that small surface shadows only centimeters in size have been shown to bias infrared spacecraft measurements of the lunar surface change the apparent temperature at different wavelengths (Bandfield et al., 2015). These challenges have resulted in a range of interpretations of the M^3 OH / H_2O feature primarily due to differences in accounting for thermal emission. Some have concluded that the 3 µm signature varies diurnally and is due to H_2O (Li & Milliken, 2017), others have concluded that the signature is static and caused by OH Bandfield et al. (2018), while yet others advocate for a partially mobile and partially stable combination of OH / H_2O (Wöhler et al., 2017). To study the source and behavior of the M^3 3 µm feature, I developed a thermal model that accounts for the roughness of the lunar surface and independently predicts the emission contributing to each M^3 observation (chapter 3).

To validate the roughness thermal model developed in chapter 3, I used thermal infrared observations from the Diviner Lunar Radiometer Experiment aboard the LRO, which has been in orbit since 2009 (Chin et al., 2007; Paige et al., 2010b). Diviner has been steadily taking measurements of the Moon for over a decade, producing the most robust global thermal data set of the Moon to date. Diviner consists of 9 channels, 7 of which are in the infrared from 7.55–400µm (Paige et al., 2010b). It was recognized early on that daytime Diviner temperatures measured by the 7 well-calibrated channels could differ from each other as a function of the solar incidence angle (governed by the time of day and latitude). Work by Bandfield et al. (2015) showed that the negative trend in apparent brightness temperature with increasing wavelength was predictable when accounting for the roughness of the lunar surface. Their argument rested on two facts of thermal radiation. The first was that the lunar surface is a very good insulator, meaning it does not conduct heat well, and the Moon also lacks an atmosphere to convect heat, causing surfaces only centimeters apart to differ in temperature by up to 100s of degrees. The second is that thermal emission (given by the Planck function) is

strongly temperature dependent and shifts to lower wavelength at higher temperatures. Therefore, imagery that cannot resolve centimeter-sized surfaces (i.e., all spacecraft data) will see a mixture of temperatures on the surface governed by the thermal conditions at each centimeter-sized facet of the surface. At high latitudes or when the sun is low in the sky (high solar incidence angle), centimeter-scale roughness can cast shadows on the surface, causing large temperature differences within a given scene (*anisothermality*). When Diviner records the total emission, it is heavily weighted to hot sunlit facets at short wavelengths and cooler shadowed facets at long wavelengths. By predicting the proportion of the surface that is shadowed under different conditions, Bandfield et al. (2015) developed an anisothermal emission model that was a good fit to Diviner observations. Later, Bandfield et al. (2018) used an updated version of this roughness-based thermal model to predict the emission contribution at 3 µm, presenting a correction of M^3 based on the thermal properties of the surface. That work suggested a strong OH / H_2O signature throughout the lunar day. In chapter 3, I update and extend the roughness thermal model developed in Bandfield et al. (2015, 2018), which was limited to lower incidence angle conditions. Using Diviner thermal observations, I validate the new model to show that it accurately captures the anisothermality introduced by roughness. I then apply the new emission predictions to M^3 observations to investigate the variability of the 3 µm OH / H_2O signature at mid to high latitudes.

The third investigation I present in chapter 4 differs from the others in that it is not based directly on spacecraft observations. In this chapter, I investigate the abundance and depth of water ice below permanently shadowed region (PSR) cold traps near the lunar south pole. Since the majority of spacecraft data are only sensitive to surface - and best efforts to seek ice in the subsurface with radar and other techniques have been inconclusive (§1.3), this chapter required a different approach. Building on a recently published model of polar ice and ejecta stratigraphy (Cannon et al., 2020), I use a computational model to simulate the delivery of ice and ejecta to polar cold traps. I also developed a thermal model to determine the loss of ice as warm ejecta is vigorously mixed into a given PSR through a process called ballistic sedimentation. At present, little is known about ice buried below the PSRs other than what we can infer from the single LCROSS impact experiment at Cabeus crater (Colaprete et al., 2010). However, as the National Aeronautics and Space Administration (NASA) Artemis program prepares to resume uncrewed and then crewed missions to the south polar region, in addition to many next-generation spacecraft missions planned to do polar reconnaissance, we may be able to test the predictions made in chapter 4 in the near future (§5.1).

1.7 Manuscript Summaries

The three manuscript chapters that follow each describe a self-contained investigation submitted or in preparation to be submitted to a peer-reviewed journal. Each manuscript contributes to my central goal of understanding the origin and distribution of water on the Moon, which I summarize here.

In chapter 2, *Manuscript I: New Constraints on the Lunar Optical Space Weathering Rate*, I investigate the rate that space weathering effects accumulate on the lunar surface. Lunar space weathering primarily consists of solar wind irradiation and micrometeorite bombardment, each of which have implications for the generation and storage of OH / H_2O on the Moon (§1.5). In this manuscript, I quantify the rate of space weathering in the lunar highlands over time through the correlation between submicroscopic iron ($smFe^0$) and ages of young lunar craters. I conclude that space weathering effects influence the lunar surface at a predictable rate for the first 1 Ga of surface exposure. Investigating the size-dependent accumulation rates of $smFe^0$, I inferred that solar wind likely influences nanophase iron accumulation, but micrometeorite bombardment could drive microphase iron accumulation. Constraining the rate at which that the solar wind and micrometeorite bombardment alter the lunar regolith has implications for solar wind implantation of hydrogen and production of OH / H_2O by space weathering.

In chapter 3, *Manuscript II: Roughness reveals persistent daytime OH/H_2O on the Moon from Equatorial to High Latitudes*, I investigate the widespread lunar 3 µm spectral feature measured by M^3 (§1.4). Associated with hydroxyl (OH) and/or water (H_2O), the 3 µm absorption feature has been thought to indicate daily migrating water, hydroxyl or water tightly locked in the surface, or some combination of migrating and static OH / H_2O. These conflicting interpretations have stemmed from challenges in compensating for thermal emission and roughness of the lunar surface. I developed an improved roughness thermal model to predict emission at 3 µm, validated it using spacecraft thermal observations, and applied it to remove emission from M^3 spectra. I investigated the variability of the 3 µm feature throughout the lunar day and with changing latitude and found no evidence that the widespread lunar OH / H_2O migrates around the surface. This indicates that although OH / H_2O is widespread across the lunar surface, it is trapped within regolith grains and unlikely to be as easily extracted as previously thought.

In chapter 4, *Manuscript III: Buried Ice Deposits in Lunar Polar Cold Traps were Disrupted by Ballistic Sedimentation*, I investigated buried ice deposits beneath lunar polar cold traps (§1.3). Permanently shadowed regions (PSRs) near the lunar poles are potentially long-lived sites where lunar water from a variety of sources may be stored. Over geologic time, nearby impact events would have delivered ejecta (regolith and boulders) to the PSRs, potentially heating, mixing and/or burying water ice that was present on the surface. A previous model estimated the quantity of ice that could be buried in the polar regions by crater ejecta,

but did not consider the heating and mixing effects of the ejecta entering each PSR. I modeled this process, known as ballistic sedimentation, and incorporated it into an improved polar ice and ejecta stratigraphy model. Using the improved model, I predicted which south polar PSRs were most likely to retain thick ice deposits at depth. This work directly supports NASA Artemis program which aims to land humans in the lunar south polar region this decade, in part to study the availability of water and other volatiles on the Moon. This work makes testable predictions about the size and distribution of buried lunar ice deposits, furthering our understanding of water abundance and storage on the Moon.

Together, these three investigations advance our understanding of lunar surface processes like space weathering, ballistic sedimentation, and water migration. These studies have implications for the production, mobility, and usability of lunar OH / H_2O both widespread across the lunar surface and buried at the lunar poles.

1.8 Open Science Philosophy

The recently established NASA Transform to Open Science (TOPS) program[1] recognizes that the lack of transparency in research practices hinders scientific progress and leads to barriers for historically excluded communities. Developed with recommendations from NASA's Strategy for Data Management and Computing for Groundbreaking Science 2019–2024, the National Academies reports on open science, reproducibility, and scientific software, and the 2021 UNESCO draft Recommendation on Open Science synthesis report, the TOPS program aims to promote scientific collaboration, accessibility, and reproducibility (SDMWG, 2018; NAS et al., 2018; CBPFOCPNSS et al., 2018; UNESCO, 2021). These initiatives are timely as concerns mount about the reproducibility of science (the so-called "reproducibility crisis"), which is driven in part by lack of access to research data and analysis code (Baker, 2016; Miyakawa, 2020). Since each manuscript in this dissertation required code for data generation, filtering, processing, and analysis, I saw an opportunity to implement open science values in my work.

A core value of the open science movement is accessibility which can be achieved in part by using existing free and open source tools to conduct research. Most code generated for this dissertation was authored in the free and open source Python programming language which has become a central tool in planetary data science and research (Laura et al., 2013; Hess et al., 2016). I also released source code developed for each manuscript chapter of this dissertation as open source, citable repositories. Care was taken to include code, documentation, usage examples, and instructions for installation to facilitate access and usability of each code base. All three repositories are publicly available on GitHub[2], an open source software hosting and

[1] `https://science.nasa.gov/open-science/transform-to-open-science`
[2] `https://github.com/`

collaboration platform (Perkel, 2016). For robustness and ease of citation, each repository was assigned a Digital Object Identifier (DOI) with Zenodo[3], and a DOI resolving to a snapshot of the specific software version used to prepare each manuscript. Each Zenodo webpage also contains a link to the full GitHub source code with latest software updates and documentation for ease of access and discoverability. Finally, all repositories are licensed with the MIT open license which allows free and unlimited use, editing, and redistribution of each package, with proper citation of the source repository. Below, I summarize the three open source repositories generated in this work.

For Manuscript I (chapter 2), I contributed to the `craterpy` Python package. Originally developed in 2017 to support my previous investigations into lunar crater maturity (Tai Udovicic et al., 2016), `craterpy` is an open source collection of tools used to extract and analyze image data associated with impact craters (Tai Udovicic, 2017). It was used to collect the smFe^0 data central to chapter 2. Through this work, `craterpy` was updated to version 0.5.1[4] to improve its recognition of geographical information embedded in image files.

In Manuscript II (chapter 3), I describe the `roughness` Python package that predicts the shadowing conditions on rough planetary surfaces (Tai Udovicic et al., 2021b). Also available as an open source Python package, the model was translated from the shadowing model described in Bandfield et al. (2018), originally written in the Davinci programming language. The model was then generalized to allow customization of the reference surface used in the statistical shadowing computation and to allow a range of thermal models to be used to predict surface emission while accounting for roughness (the model is described in detail in §3.3). Version 0.10.1[5] was released in preparation for Manuscript II to be submitted for peer review.

The Moon Polar Ice and Ejecta Stratigraphy model is the basis of Manuscript III (chapter 4) and is available as an open source Python package called `moonpies` (Tai Udovicic et al., 2022a). The model framework was translated from a MATLAB script published by Cannon et al. (2020) and then significantly updated to add several methods of ice and ejecta delivery and to improve computational efficiency and reproducibility. Version 1.0.0[6] allows users to tweak nearly every model parameter with a simple configuration file and allows deterministic, reproducible Monte Carlo model runs by supplying a random seed. A detailed description of the MoonPIES model and its parameters is given in §4.3.

The three open source repositories developed here contribute to the wider body of planetary research software and embrace the core goals of the NASA TOPS movement. These transparent research code bases are now available for use and open to feedback, improvements, and contributions from the wider community.

[3] `https://zenodo.org/`
[4] https://doi.org/10.5281/zenodo.4780769
[5] https://doi.org/10.5281/zenodo.7440068
[6] https://doi.org/10.5281/zenodo.7055800

Chapter 2

Manuscript I: New Constraints on the Lunar Optical Space Weathering Rate

Christian J. Tai Udovicic[1], Emily S. Costello[2], Rebecca R. Ghent[3], Christopher S. Edwards[1]

This is the Accepted Manuscript version of an article accepted for publication in Geophysical Research Letters (GRL). Wiley Inc is not responsible for any errors or omissions in this version of the manuscript or any version derived from it. The Version of Record is available online at `https://doi.org/10.1029/2020GL092198`.

2.1 Abstract

Space weathering processes form submicroscopic metallic iron particles that are optically active, darkening and reddening the lunar surface over time. The optical effects of these particles depend on their size; nanophase iron darkens and reddens, while microphase iron darkens without reddening. Using available Kaguya Multiband Imager parameter maps believed to estimate submicroscopic iron abundance, we investigate trends that may be associated with abundance of nanophase and microphase iron near dated lunar craters. We observe that nanophase iron is strongly correlated with crater age, while microphase iron exhibits a weaker correlation. We present models for the highlands nanophase and microphase iron accumulation rates from 100 ka – 1 Ga. Our observations suggest that highlands nanophase iron abundance is a direct result of space weathering exposure, while highlands microphase iron abundance is likely influenced by lunar source materials or stochastic impact-delivery mechanisms.

Plain Language Summary

The Moon, Mercury, and asteroids lack protective atmospheres and slowly darken over time due to their exposure to space. We call this darkening process space weathering. Apollo samples returned from the Moon show that space weathering produces tiny iron particles that range in size from nanometers to micrometers. We use orbital lunar maps of nanophase and microphase iron content to better understand how quickly space weathering occurs on the Moon. We first find the iron content of young lunar soils deposited by

[1]Northern Arizona University (NAU), Department of Astronomy and Planetary Science (DAPS), PO Box 6010, Flagstaff, AZ 86011, USA
[2]University of Hawai'i at Manoa, Honolulu, HI, USA
[3]Planetary Science Institute, Tucson, AZ, USA

large impact events, then use the age of each impact crater to see how much iron accumulates in different lengths of time. We find that nanophase iron accumulates predictably over time due to space weathering. In contrast, microphase iron accumulates less predictably, possibly because it exists in the lunar soil initially, or is delivered to the Moon by crater-forming impacts. Our work helps us understand how the surface of the Moon weathers over time and how space weathering might work elsewhere in the Solar System.

2.2 Introduction

Space weathering is the combination of processes that physically and chemically alter the surfaces of airless bodies over time. On the Moon, space weathering darkens and reddens the optical spectrum through formation of fine metallic iron particles, termed submicroscopic iron ($smFe^0$) (Cassidy & Hapke, 1975; Pieters et al., 2000; Hapke, 2001). The optical effects of $smFe^0$ are highly dependent on its size: smaller *nanophase iron* particles (1–40 nm) cause optical darkening and reddening, and larger *microphase iron* particles (40 nm – 2 μm, sometimes called Britt-Pieters particles) darken without reddening (Keller & Clemett, 2001; Britt & Pieters, 1994; Noble et al., 2007; Lucey & Noble, 2008; Lucey & Riner, 2011). In this work, we use published parameter maps thought to represent different forms of $smFe^0$ along with craters of known age to estimate the rate of accumulation of nanophase and microphase iron on the lunar surface.

Several mechanisms of $smFe^0$ formation are actively debated in the literature. An early hypothesis suggested that solar wind sputtering and/or H^+ implantation could reduce mineral iron in oxides (FeO) to form metallic Fe^0 (Wehner, 1961; Cassidy & Hapke, 1975). While ion irradiation experiments are capable of producing $smFe^0$, it appears that H^+ implantation is not a necessary precursor as seen in He ion irradiation and pulse laser experiments which simulate micrometeorite bombardment (Sasaki et al., 2001; Loeffler et al., 2009). The discovery of thin $smFe^0$-bearing rims on individual regolith grains appeared to solve the conundrum (Keller & McKay, 1993, 1997). Hapke (2001) described a model by which solar wind sputtered and micrometeorite vaporized material would naturally deposit nanophase iron on adjacent grains (Hapke, 1973). The $smFe^0$-bearing grain rims could then combine and form the full distribution of nanophase and microphase iron particles found in agglutinates by successive melt/vaporization events (Noble et al., 2007; Pieters & Noble, 2016). The sputter deposit aspect of this model is backed by several remote observations that report reduced optical space weathering in zones of reduced solar wind flux (e.g. at higher latitude or on magnetically shielded lunar swirls) (Hemingway et al., 2015; Glotch et al., 2015; Sim et al., 2017). Thus far, laboratory simulations of solar wind irradiation have failed to confirm the solar wind sputter-deposits (Christoffersen et al., 2015). In addition, solar wind contribution is called into question by immature Apollo soils which appear to contain an abundance of nanophase iron in micrometeorite-associated vapor deposits,

relative to solar-wind damaged grain rims (Keller & Zhang, 2015). Here, we provide new constraints on the possible $smFe^0$ formation mechanisms by leveraging modeled nanophase and microphase iron particle abundances predicted from radiative-transfer modeling (Trang & Lucey, 2019).

While most of the lunar surface is heavily space weathered and locally homogenized by regolith gardening, notable exceptions are the bright rays and youthful ejecta of recently formed craters. Impact craters provide natural time stamps on the lunar surface and their ejecta have informed our understanding of lunar space weathering for decades (e.g., Shoemaker & Hackman 1962; Grier et al. 2001). Notably, the Diviner rock abundance proximal to dated craters exhibits a tight correlation with crater age, constraining the mechanical weathering of surface rocks and providing a new chronometer used to date similarly rocky craters (Ghent et al., 2014; Mazrouei et al., 2019). Constraining the optical weathering rate of the regolith has proven more challenging, partially due to target composition biasing maturity parameters, inhibiting global comparisons (Grier et al., 2001; Braden & Robinson, 2013; Nettles et al., 2011).

Our work updates our understanding of the optical weathering rate in two important ways. First, we use modern parameter maps of nanophase and microphase iron which are empirically validated by Apollo soil spectra and backed by a physical radiative-transfer model (Trang & Lucey, 2019). Second, we use a larger sample of dated lunar craters <1 Ga, enabled by recent developments in remote detection and chronology of young lunar craters (Ghent et al., 2014; Williams et al., 2018). For comparison with previous work, we apply our methodology to a database of large rayed craters previously investigated in the Clementine optical maturity parameter (Grier et al., 2001). We present new surface accumulation rates of nanophase and microphase iron and discuss key constraints that they place on the lunar optical space weathering rate.

2.3 Methods

We split our analysis into 2 parts: Global and Highlands. First, we investigate global (within $\pm 60^0$ latitude) $smFe^0$ trends, incorporating both the highlands and mare regions. Using crater populations dated relative to one another, we present overall trends in the nanophase and microphase iron with age and show heritage from the Grier et al. (2001) global study of lunar optical maturity (Figure 2.2). Second, we restrict our study to the lunar highlands and craters with absolute model ages. We derive surface accumulation rates from time-resolved fits to the highlands nanophase and microphase iron abundance (Figure 2.3). This portion of the analysis is limited to the iron-poor lunar highlands which are more consistent in FeO content and optical space weathering trends (Lucey et al., 1998; McFadden et al., 2019; Trang & Lucey, 2019).

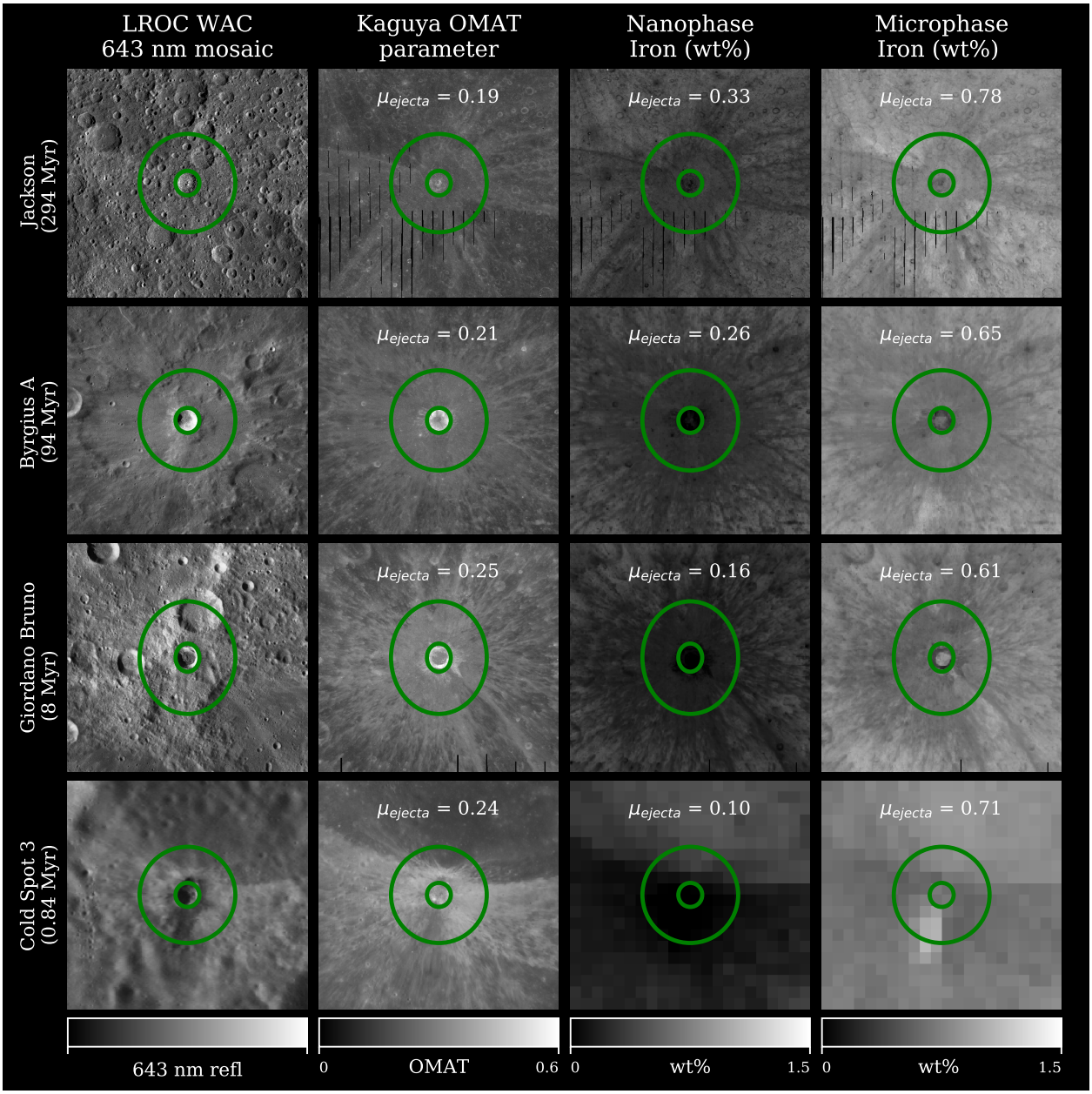

Figure 2.1: Four craters of decreasing model age (descending order) shown in the Lunar Reconnaissance Orbiter Wide Angled Camera 643 nm mosaic, Kaguya Optical Maturity (OMAT) parameter, nanophase iron abundance and microphase iron abundance (left to right; Speyerer et al. 2011; Lemelin et al. 2016; Trang & Lucey 2019). Ejecta annuli extending from each crater rim to 4 crater radii are denoted in green. Mean OMAT, nanophase iron abundance, and microphase iron abundance computed within the annulus are shown in each respective inset as μ_{ejecta}.

2.3.1 Nanophase and Microphase Iron abundance

We define an annular region of interest around each crater in the global 60°N – 60°S, 1 km/pixel nanophase and microphase iron maps of Trang & Lucey (2019) using the craterpy Python package (Tai Udovicic, 2017). We scale each annulus with crater radius; the inner edge of the annulus is set at the crater rim (1 crater radius from the center), while the outer edge of the annulus extends to 4 crater radii (Figure 2.1). We parameterize each crater by the mean nanophase and mean microphase iron abundance within the annulus, excluding terrain within the crater rim which may be refreshed by mass wasting on steep slopes. In the global analysis, the mean iron abundances are grouped by relative age (Figure 2.2). In the highlands analysis, the mean iron abundances of each crater are plotted with age (Figure 2.3).

Four crater radii is chosen as the maximum annular extent because the youngest craters in our sample typically feature a continuous nanophase iron depletion zone of this size. We note that a small fraction (∼9%) of our highlands crater population exhibit asymmetric ejecta, causing some background contamination in select craters (e.g., Cold Spot 3, Figure 2.1). In addition, small fresh impacts may act to refresh the material within our chosen annulus. We limit our sample to craters of sufficient size (annulus $\geq$ 12 pixels) such that these effects are minor for any given crater (Fig. S3). Additionally, we fit a sufficient sample (n=77 craters in the highlands) such that these effects are negligible on our overall trends (Fig. S4). We do not undertake a detailed mapping of crater ejecta because anomaly identification is likely to be biased for craters near the resolution limit of the Trang & Lucey (2019) maps.

2.3.2 Crater Populations

The global analysis uses two published crater databases providing relative crater ages. The Lunar and Planetary Institute (LPI) crater database consists of the 421 craters dated as Copernican, Eratosthenian, and Imbrian in the Lunar and Planetary Institute Lunar Impact Crater Database (Losiak et al., 2015). The OMAT crater database contains large rayed craters relatively dated by Grier et al. (2001) as Young (appear younger than Tycho), Intermediate (appear younger than Copernicus) and Old (appear older than Copernicus) using the Clementine OMAT parameter (Table 2.1).

The highlands analysis uses three published crater databases providing absolute model ages of craters. The *Chronology* crater database consists of 8 craters dated using crater counting techniques, assuming the standard lunar chronology function (e.g., Neukum et al. 2001). These craters are Byrgius A, Giordano Bruno, Hell Q, Jackson, King, Moore F, Necho, and Tycho (Morota et al., 2009; Hiesinger et al., 2012; van der Bogert et al., 2010; Eugster, 1999; Ashley et al., 2012; Salih et al., 2016). For craters with multiple published ages, we selected model ages derived from crater counts on the ejecta.

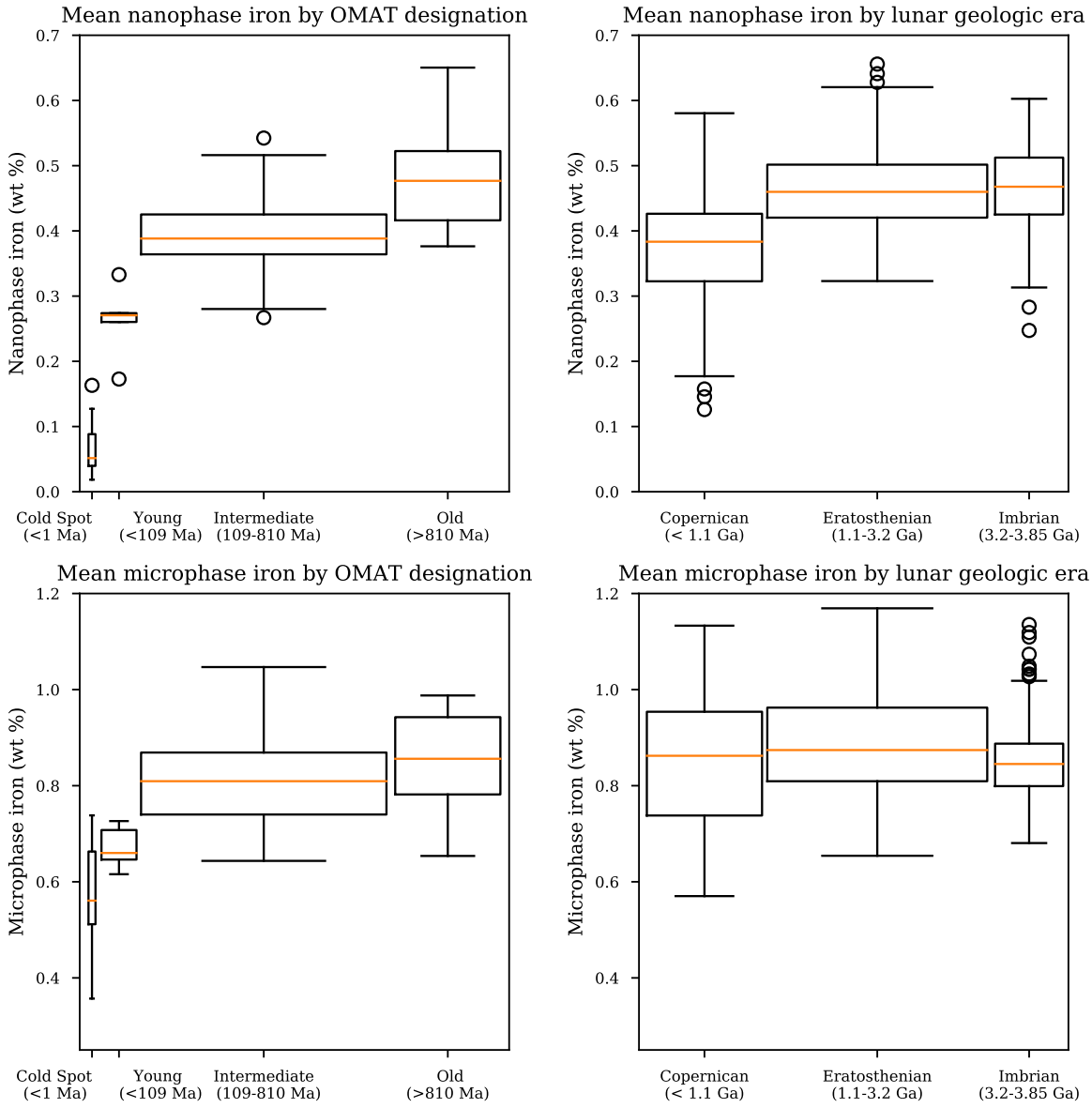

Figure 2.2: Box plots of mean nanophase iron (top) and microphase iron (bottom) in the crater annuli of the OMAT (left) and LPI databases (right), grouped by relative age. Cold spot craters are included as a young endmember population. The central orange bar of each population denotes the median and the whiskers denote 1.5*IQR (interquartile range). Circles denote outliers outside 1.5*IQR). Nanophase and microphase iron abundances increase with relative ages of OMAT craters. Copernican craters exhibit a paucity of nanophase iron relative to Eraotsthenian and Imbrian craters, but this contrast is less apparent for microphase iron.

The *Rock Abundance* crater database consists of 57 craters ≥10 km in diameter which have published absolute model ages based on the Diviner Rock Abundance of their ejecta (Ghent et al., 2014; Mazrouei et al., 2019). Several Chronology craters are duplicated in the Rock Abundance database. Where this is the case, we choose the model age predicted by the standard lunar chronology function. The *Cold Spot* crater database consists of 12 Diviner cold spot craters dated by crater counting techniques and the standard lunar chronology function (Williams et al., 2018). We group this database separately from the *Chronology* craters because they form a population of the youngest craters in our sample and are thermophysically distinct (Williams et al., 2018).

Table 2.1: The five impact crater databases, the ages they provide, and the final counts used in this study (see Data Sets S1 & S2 for full tables).

Crater Database	**Age Classification**	**Population Age**	**Count**
Cold Spot†	Absolute	220 ka – 1.3 Ma	12
Chronology†	Absolute	1.5 Ma – 990 Ma	8
Rock Abundance†	Absolute	22 Ma – 990 Ma	57
OMAT	Young	≤ Tycho (∼100 Ma)	5
	Intermediate	Tycho – Copernicus	38
	Old	> Copernicus (∼800 Ma)	18
LPI	Copernican	< 1.1 Ga	70
	Eratosthenian	1.1 Ga — 3.2 Ga	118
	Imbrian	3.2 Ga — 3.85 Ga	233
Saturation range†	≥ Eratosthenian	≥ 1.1 Ga	52

†Highlands subset only.

The *Highlands Saturation Range* population consists of 52 craters used to infer the levels of saturation for the nanophase and microphase iron in the lunar highlands. This population is a subset of the LPI crater database containing only highlands craters Eratosthenian or older and ≤200 km in diameter.

We filter all craters by the following criteria: The entire ejecta annulus falls in bounds of, and represents at least 12 pixels in, the 1 km/pixel, 60°N, 60°S global $smFe^0$ maps (Trang & Lucey, 2019). Highlands crater annuli must additionally not cross the mare bounds defined by Nelson et al. (2014), who used Lunar Reconnaissance Orbiter Camera (LROC) images to precisely demarcate lunar mare boundaries. Although the $smFe^0$ maps decrease in mean abundance at latitudes pole-wards of ±50° (Trang & Lucey, 2019), all dated highlands craters that meet the above criteria are within 50°N and 50°S so we do not apply a latitude correction in this work (Fig. S1).

Final counts and age summaries for each database are given in Table 1. See Data Sets S1 & S2 for full crater lists and derived $smFe^0$ abundances.

2.4 Results

2.4.1 Global Analysis

We plot our derived distribution of mean nanophase and microphase iron for craters from the LPI and OMAT databases, grouped by relative age (Figure 2.2). The Cold Spot database is included as the young endmember population for comparison. We observe consistently lower modeled nanophase iron abundance relative to microphase iron. Unexpectedly, microphase iron is enhanced (median > 0.5 wt %) initially for cold spot craters (≤ 1 Ma), while nanophase iron is negligible for the same craters (median < 0.05 wt %). In the LPI populations, only the Copernican range is exhibits reduced nanophase and microphase iron, consistent with having observable unsaturated rays (Shoemaker & Hackman, 1962; Losiak et al., 2015). No significant smFe^0 variation is observed in non-Copernican populations (i.e., OMAT Old, Eratosthenian, and Imbrian craters), implying saturation. Relatively wide saturation ranges are expected due to variable FeO content in the mare and highlands, as discussed in Trang & Lucey (2019). In addition, we observe that nanophase iron abundance is consistently lower than microphase iron abundance across all populations, while the former appears to increase rapidly on very young surfaces.

2.4.2 Highlands Analysis

We plot the mean nanophase and microphase iron of each highlands crater versus crater age (Figure 2.3). Age uncertainties indicated are the crater chronology model age uncertainties for Cold Spot and Chronology craters, and the 95% credible intervals for Rock Abundance craters (see references in Table 2.1). Uncertainties in smFe^0 are the standard error of the mean within each crater annulus. To investigate the evolution of smFe^0 over time, we plot these data both on log-log and linear-log axes (Figure 2.3a and Figure 2.3b, respectively).

Linear fits on log-log axes are consistent with power law growth in time (Figure 2.3a). Microphase iron appears weakly power-law correlated ($R^2 = 0.37$, Equation 2.1). By contrast, nanophase iron is non-linear on log-log axes, indicating non-power law growth (more apparent on linear axes (Fig. S2).

Linear fits on linear-log axes are consistent with logarithmic functions of time (Figure 2.3b). The logarithmic fit to microphase iron is again weakly correlated ($R^2 = 0.36$), while nanophase iron is strongly correlated in log-time ($R^2 = 0.88$). Logarithmic fits predict a greater y-intercept (initial abundance) for microphase iron (a=0.57 wt%, b: 0.024), relative to (a=0.081 wt%, b: 0.049) for nanophase iron, where fits are given by $y = a + blog(x)$ (Equations 2.2–2.3). We discuss the significance of the differing intercepts in Section 2.5.2.

We also compute saturation ranges of nanophase iron (0.40 – 0.51 wt%) and microphase iron (0.75 –

0.86 wt%) representing the mean $\pm 1\sigma$ range of smFe^0 in LPI Highlands Saturation annuli (shaded regions, Figure 2.3). The fits described above and in Equations 2.1–2.3 each reach saturation in 1 Ga within error, as expected.

We note that the power law and logarithmic fits for microphase iron are equivalent within error, but we present both fits for ease of comparison with previous power law models of space weathering and impact flux (e.g., Ghent et al. 2014; Mazrouei et al. 2019). The power law curve of best fit (Figure 2.3a) is given below, where y is microphase iron abundance (wt%) and x is age (Ma).

$$y_{\text{microphase}} = (0.56 \pm 1)x^{0.040 \pm 0.0059}, R^2 = 0.37 \tag{2.1}$$

The logarithmic curves of best fit of microphase and nanophase iron (Figure 2.3b) are given below, where y is metallic iron abundance (wt%) and x is age (Ma).

$$y_{\text{microphase}} = (0.57 \pm 0.018) + (0.024 \pm 0.0037)\text{log(x)}, \text{R}^2 = 0.36 \tag{2.2}$$

$$y_{\text{nanophase}} = (0.081 \pm 0.010) + (0.049 \pm 0.0021)\text{log(x)}, \text{R}^2 = 0.88 \tag{2.3}$$

In summary, our results place the following empirical constraints on the growth of highlands nanophase and microphase iron over time.

1. Both nanophase and microphase iron are correlated in logarithmic time.
2. Microphase iron is less correlated than nanophase iron in log time (R^2=0.36 and R^2=0.88, respectively).
3. Nanophase iron is negligible initially (0 wt% within error for craters 100 ka or younger)
4. Microphase iron appears to be elevated initially or very soon after crater formation ($\sim$0.5 wt% for 100 ka craters)

2.5 Discussion

2.5.1 Global Constraints

We observe clear increasing trends in absolute nanophase and microphase iron abundance over Copernican timescales (Figure 2.2). Both sizes of smFe^0 appear saturated for non-Copernican populations (i.e., OMAT old, Eratosthenian, and Imbrian), as expected. The greater abundance of microphase iron relative to nanophase iron, particularly in the youngest craters, is notable and will be discussed further below. Our analysis shows that previous crater maturity studies with OMAT are broadly consistent with the modeled

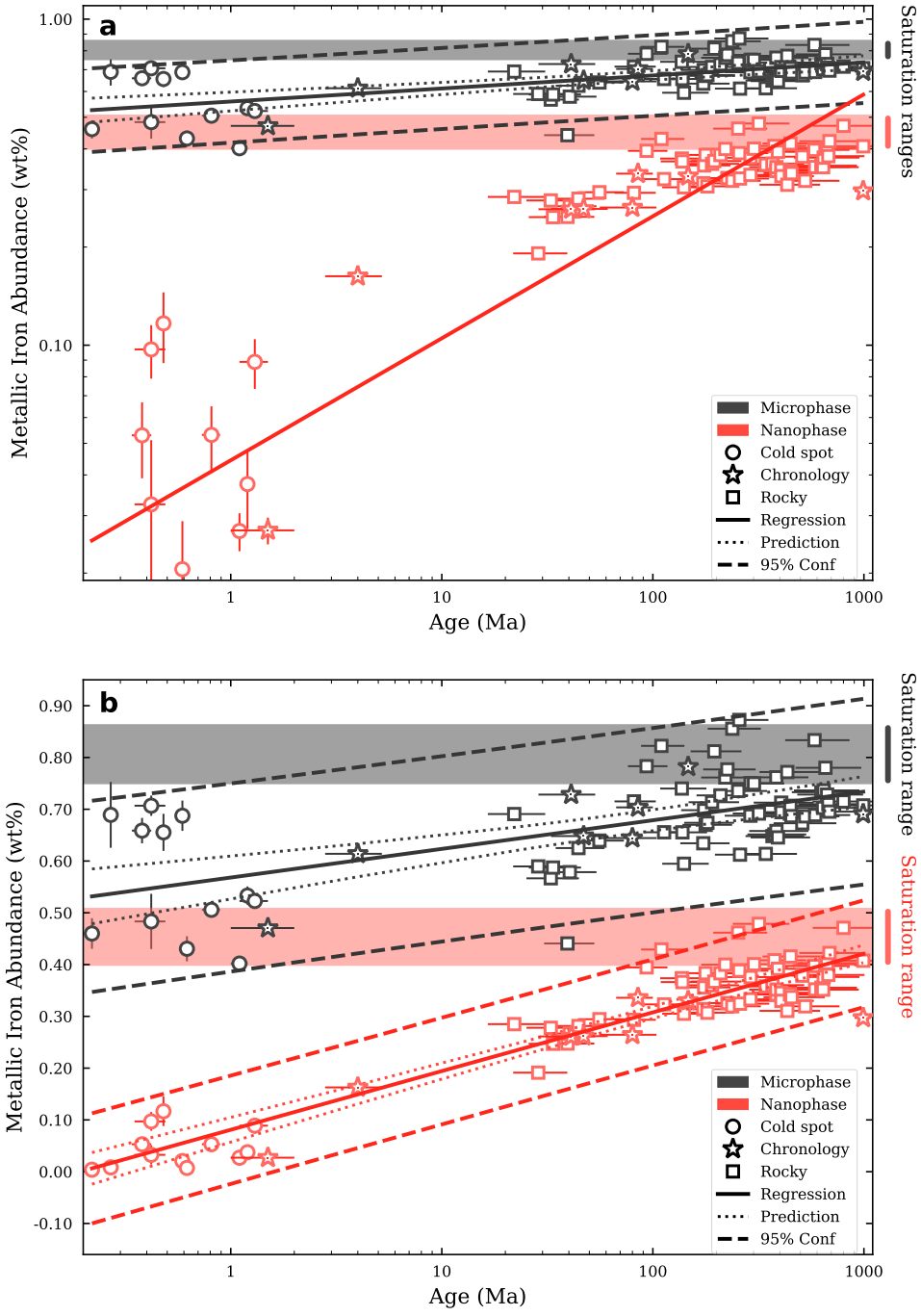

Figure 2.3: Mean abundances of microphase iron (black) and nanophase iron (red) in highlands crater annuli plotted over crater age. **a** Log-log axes and straight-line power law fits. **b** Linear-log axes and straight-line linear-logarithmic fits. Saturation ranges (shaded regions) denote the mean $\pm 1\sigma$ of non-Copernican highlands LPI craters. Ordinary least squares regression fits (Equations 2.1–2.3), prediction intervals and 95% confidence intervals are shown.

nanophase and microphase iron abundances of Trang & Lucey (2019). Further global interpretations would require a more detailed understanding of how local iron composition influences the rate of production and saturation limits of $smFe^0$ (McFadden et al., 2019; Trang & Lucey, 2019).

2.5.2 Highlands Constraints

Our modeled linear-logarithmic fit to highlands nanophase iron abundance exhibits a strong correlation with age ($R^2 = 0.88$) and an approach to saturation in $\tilde{1}$ Ga, i.e. on a Copernican timescale, as expected (Equation 2.2; Figure 2.3b). Our model residuals are consistent with respect to latitude, longitude, crater radius and crater age, suggesting the trend we observe is robust (Fig. S5). Our model also predicts negligible nanophase iron in the initial primary ejecta of craters in our sample (> 0.5 km diameter). Our results are consistent with ferromagnetic resonance (FMR) measurements of $smFe^0$ in Apollo soils which found that nanophase iron is strongly correlated with maturity and negligible in pristine regolith (Morris, 1980). Our model is broadly consistent with our understanding of lunar space weathering and relates modeled nanophase iron abundance to surface exposure age for the first time.

In contrast, highlands microphase iron exhibits weakly correlated linear-logarithmic or power law growth over time ($R^2 = 0.36$ and 0.37, respectively). Since these fits are indistinguishable within errors, we discuss the linear-logarithmic model which is both simpler and consistent with the nanophase iron model. The non-zero early abundance and weak correlation of microphase iron with crater age are qualitatively similar to the trends Morris (1980) identified in Apollo samples. That study found that the microphase fraction of $smFe^0$ is present in pristine Apollo soils and is weakly correlated with maturity, likely due to the variable quantities present in lunar source materials. We note that our modeled microphase iron abundance saturation range (0.75 – 0.86 wt%) exceeds the maximum corresponding Fe^0_C–Fe^0_A content (0.56 wt %) measured by Morris (1980). This discrepancy could be due to the Trang & Lucey (2019) radiative-transfer model assuming microphase iron particles are ≥ 33 nm, smaller than other derivations of the microphase iron particle size in the literature (Noble et al., 2007; Lucey & Riner, 2011). If the microphase iron particle size is increased in the Trang & Lucey (2019) model, we would expect an overall downward shift in microphase iron abundances that would preserve the trends we observe over time. Therefore, the microphase iron models we present in Equations 2.1–2.2 capture trends in the relative abundance of microphase iron over time, though they may not be reliable as absolute wt % abundance predictors.

2.5.3 A Broken Link Between Nanophase and Microphase Iron Accumulation

Our analysis of highlands $smFe^0$ reveals three primary differences in the accumulation of nanophase and microphase iron over 100 ka – 1 Ga:

1. Crater ejecta ∼100 ka contain negligible nanophase iron, but detectable microphase iron.
2. Microphase iron is less correlated with crater age than nanophase iron.
3. Nanophase iron accumulates at a greater rate (steeper log slope) than microphase iron through time.

We discuss the implications of these constraints on the following models of optical space weathering:

Nanophase aggregation: A common hypothesis is that nanophase iron is primarily formed in vapor deposits by micrometeorite impacts and is later aggregated to form microphase iron in agglutinates (Pieters & Noble, 2016). This hypothesis is corroborated by the observation that nanophase iron is found primarily in the rims of individual soil particles, while microphase iron is found in heavily reworked agglutinates (Keller & McKay, 1993, 1997; Keller & Clemett, 2001).

Our observations indicate that if nanophase aggregation is the primary space weathering mechanism, then either the Trang & Lucey (2019) maps preferentially overestimate the abundance of microphase iron near young craters or the provenance of microphase iron abundance is more linked to source materials than space weathering products. From 100 ka until saturation, microphase iron is much more weakly correlated with crater age ($R^2 = 0.36$) than nanophase iron ($R^2 = 0.88$), indicating that microphase iron abundance is only a minor function of exposure to space weathering. This observation could be explained if highlands source materials (e.g., bedrock and breccia) contain highly variable quantities of microphase iron, thus seeding each crater in our sample with an independent initial abundance. Additionally, Morris (1980) also proposed that impactors larger than micrometeorites may be a source of microphase iron. If this is the case, the initial quantity of microphase iron could also depend on the composition of the primary impactor, while delivery of microphase iron by later non-micrometeorite impacts may explain the variance in our observations. Therefore, while micrometeorite bombardment may aggregate nanophase iron into microphase iron, our observations suggest this is not the primary source of microphase iron in the highlands regolith.

Nanophase and microphase independent growth: An alternative hypothesis is that nanophase and microphase iron accumulation are governed by independent processes. For example, solar wind and micrometeorites could both play significant but distinct roles in lunar space weathering. This hypothesis is most commonly supported by observations of inconsistent weathering trends correlated with the solar wind flux, e.g. with latitude, across magnetic anomalies, and on equator-ward and pole-ward facing slopes (Hemingway et al., 2015; Glotch et al., 2015; Sim et al., 2017).

Our observations are consistent with a mechanism by which nanophase iron accumulation is controlled by the solar wind while microphase iron accumulation is controlled by micrometeorites (Hemingway et al., 2015). Observations of Apollo soils have revealed that solar wind amporphized rims in the finest fraction of lunar soil grow in thickness over logarithmic time, while vapor deposited rim thicknesses show no correlation in time (Keller & Zhang, 2015). The logarithmic growth of solar wind amorphized rims of the finest fraction of lunar soil may suggest that the well-correlated logarithmic growth of nanophase iron we observe here is controlled by solar wind amorphization of the finest fraction. Micrometeorites may then be responsible for redistributing solar wind-produced nanophase iron in depositional rims and/or aggregating it into microphase iron in agglutinates, as described above. Alternatively, microphase iron growth may be controlled entirely by micrometeorite or larger impactors with negligible input from the solar wind, as the saturation of lunar swirls in microphase – but not nanophase – iron appears to suggest (Trang & Lucey, 2019). The potential bombardment source of microphase iron in Apollo soils was noted to be indistinguishable from lunar source materials by Morris (1980). Similarly, our analysis cannot distinguish between microphase iron present initially in lunar highlands materials or delivered stochastically by later bombardment.

The nanophase and microphase iron accumulation rates we present are broadly consistent with our understanding lunar space weathering. Our results also suggest that parameterizing crater ejecta by the mean within 4 crater radii is a simple yet effective tool for comparing crater ejecta across orders of magnitude in size and age. Extending these analyses to the lunar maria could further constrain the role of source materials in the accumulation of nanophase and microphase iron on the lunar surface, in turn yielding additional insights for the role of solar wind and micrometeorites in lunar space weathering. We also note that while the final saturation of nanophase and microphase iron is likely governed by gradual homogenization by impact gardening (Gault et al., 1974; Costello et al., 2018), we find no significant change in linear-log accumulation rate of $smFe^0$ over the crater ages and sizes observed here.

2.6 Conclusions

Our analysis reveals distinctions between the surface accumulation of nanophase iron and microphase iron over time on the lunar surface. Globally, the nanophase and microphase iron parameters accumulate over time and show good agreement with prior investigations of optical space weathering. In the lunar highlands, we observe negligible nanophase iron $<$ 100 ka and a tightly correlated accumulation from 100 ka – 1 Ga. By contrast, we observe an initial enhancement in microphase iron associated with very young craters $<$ 100 ka, followed by a gradual approach to saturation from 100 ka – 1 Ga. For the first time, we present quantitative accumulation rates of lunar nanophase and microphase iron in the highlands. Furthermore, our analyses

suggest that space weathering exposure is the primary predictor of highlands nanophase iron abundance, while highlands microphase iron abundance may be influenced by lunar source materials or delivery by micrometeorite or larger impacts. The insights into lunar $smFe^0$ presented here will help disentangle the myriad processes that weather the surfaces of airless bodies over time.

2.7 Acknowledgments

The space weathering data used in this study are publicly available via the Geosciences Node of the Planetary Data System: `https://pds-geosciences.wustl.edu/missions/kaguya/trang_moon.htm`. Python code used to extract regions of interest from these data is available via the open source Craterpy (Version 0.5.1) Python package which is available for use with proper citation under the Massachusetts Institute of Technology (MIT) license (DOI: 10.5281/zenodo.830057). Current versions are also available from the GitHub repository: `https://github.com/cjtu/craterpy`. Crater data tables produced in this work are described in the supplementary information and are available for use with proper citation under the Creative Commons Attribution 4.0 (CC BY 4.0) license (DOI: 10.5281/zenodo.4345058). We would like to thank C. M. Pieters and an anonymous reviewer for their helpful comments which greatly improved this work.

Chapter 3

Manuscript II: Roughness Reveals Persistent OH/H_2O on the Moon from Equatorial to High Latitudes

Christian J. Tai Udovicic[1], C. W. Haberle [1], C. S. Edwards [1], J. L. Bandfield[2], J. K. Gonzales[1], J. A. Ruiz[1], W. H. Farrand[2]

This a preliminary version of an article in preparation for submission to a peer reviewed journal.

3.1 Abstract

Spectral signatures associated with OH/H_2O have been recently detected globally on the Moon by several independent instruments. Of these, the Moon Mineralogy Mapper (M^3) hyperspectral imager has the greatest spatial coverage and resolution in the 2.7–3 µm spectral region. However, different approaches to thermal emission correction have resulted in conflicting interpretations of the M^3 3 µm absorption feature. Determination of lunar thermal emission is complicated by the rough lunar surface. Observed brightness temperatures can vary as a function of wavelength due to anisothermality within a scene. Here, we present an updated physics-based thermal model, with a probabilistic treatment of surface roughness, that we use to correct M^3 spectra at a range of latitudes and local times. A generalized raytracing model predicts shadowing of self-affine rough surfaces over a range of illumination conditions. These shadowing statistics are coupled with a 1D heat diffusion model to predict the aggregated anisothermal emission for a given viewing geometry and roughness. We show that this model accurately predicts the daytime anisothermal emission observed by Diviner from 15° to 70° of solar incidence. Employing our model to account for thermal emission present in M^3 data, we find a deep and persistent 3 µm feature at all latitudes and local times. Our observations support a strongly bound source of the widespread lunar OH/H_2O feature which does not migrate on diurnal timescales.

[1]Northern Arizona University, Department of Astronomy and Planetary Science, PO Box 6010, Flagstaff, AZ 86011, USA
[2]Space Science Institute, Boulder, CO

Plain Language Summary

The Moon has long been thought to be dry because it lacks the atmosphere needed to lock in water at its extreme daytime temperatures. Surprising data returned from multiple sources over the last 15 years found that trace amounts of water do exist and may migrate around the surface daily in a lunar water cycle. However, water migration was mainly observed using Moon Mineralogy Mapper data which can be biased by the temperature of the lunar surface. Precisely measuring the temperature of the Moon is challenging because surfaces only centimeters apart can differ in temperature by hundreds of degrees Celsius, particularly when the sun is low in the sky and casts long shadows on the rough lunar surface. Here, we present a method that accurately predicts lunar temperatures while accounting for shadows due to roughness. When we revisit the data with our updated temperature correction, we find a strong water feature that does not vary throughout the day. This could indicate that water is stuck to the surface or that we are not detecting water (H_2O), but the similar hydroxyl (OH) molecule instead. In either case, the global H_2O or OH stored in the surface may be more difficult to extract than previously thought.

3.2 Introduction

Recent remote detections of hydroxyl (OH) or water (H_2O) on the lunar surface have reignited interest in the Moon as a potential reservoir of *in-situ* resources. Although the lack of volatiles in lunar samples (e.g., Wolf & Anders 1980) appeared to confirm the long-held belief that the daylit lunar surface is dry (Kuiper, 1952), surprising observations from 3 independent spacecraft reported a widespread 3 µm spectral feature associated with OH or H_2O on the daylit lunar surface (Pieters et al., 2009; Clark et al., 2011; Sunshine et al., 2009). More recently, improved spacecraft observations have reaffirmed the daytime OH/H_2O signature (Chauhan et al., 2021), while Earth-based observations detecting a diagnostic H_2O signature are the first to distinguish water from hydroxyl in specific target regions (Honniball et al., 2020).

Presently, most remote investigations of lunar OH/H_2O have relied on spectra from the Moon Mineralogy Mapper (M^3) which flew on Chandrayaan-1, due to its high spatial resolution and near-global coverage of the 2.72 µm (OH) and 3 µm (H_2O) absorption features (Pieters et al., 2009; Green et al., 2011). However, lunar surface emission sharply increases across the ∼2–3 µm spectral region at typical daytime temperatures, masking these absorptions beneath a "thermal tail" (Figure 3.1). This rising thermal emission is typically compensated by a simple temperature fit (e.g., Rivkin et al. 2003), however, the shape of the thermal tail is poorly constrained over the narrow ∼2–3 µm emission range resolved by M^3. Radiance in this range is further confounded by the potentially variable depth and shape of the OH/H_2O absorption feature(s) in the lunar soil which may cover a broad range from 2.67 µm to at least 3.4 µm, according to laboratory irradiation

experiments (McLain et al., 2021). As a result, interpretations of the strength and behavior of the M^3 3 µm band have varied widely depending on the approach to thermal correction (see Lucey et al. 2021 for a review). Here, we present a physics-based M^3 emission correction which independently predicts ~2–3 µm emission without assumptions of the underlying spectral shape.

Previous M^3 thermal emission corrections may have varied in their interpretations due to their approach to accounting for surface roughness. Roughness affects the apparent temperature of the lunar surface as a function of solar incidence angle, wavelength, surface physical properties, and viewing geometry (Bandfield et al., 2015). Thermal emission corrections that did not account for roughness showed variation in the 3 µm feature with solar incidence angle (e.g., with latitude and local time; Clark et al. 2011; Li & Milliken 2017), while roughness-based thermal corrections observed a more prominent 3 µm feature that survives the full lunar day (Wöhler et al., 2017; Bandfield et al., 2018) . Here, we update the roughness-based thermal emission correction of Bandfield et al. (2018) and validate it using daytime emission observations from the Diviner lunar radiometer on board the Lunar Reconnaissance Orbiter (Paige et al., 2010b). The goal of this study is to examine the diurnal and latitudinal behavior of the widespread M^3 3 µm feature when thermal emission is corrected by a robust surface roughness thermal model.

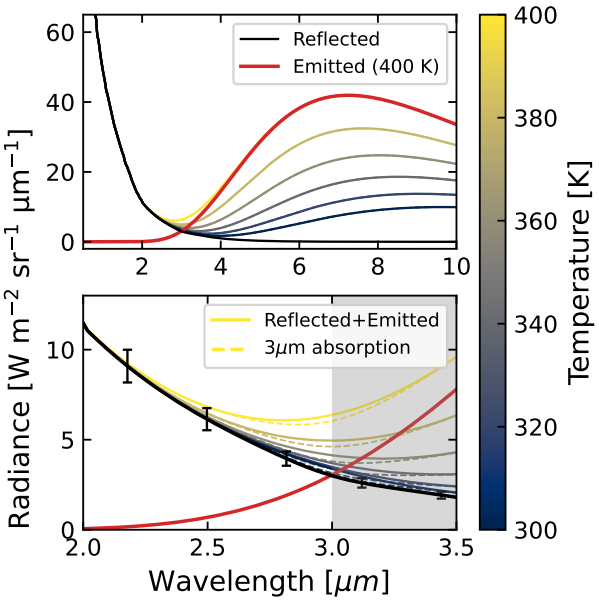

Figure 3.1: Top: Reflected M^3 L1 radiance (black; extrapolated via exponential decay >2.5 µm) and sum of reflected and blackbody emission curves 300–400 K (the 400 K blackbody curve shown in red for reference). Bottom: the same synthetic spectra (solid lines) with a broad 5% absorption feature centered at 3 µm). Errorbars estimated at 10% of radiance (maximum M^3 radiometric uncertainty Green et al. 2011).

3.3 Methods

To accurately interpret the 3 µm feature in M^3 spectra of the lunar surface, we must account for the thermal emission contribution which begins to become a significant fraction of surface radiance longward of 2–2.5 µm at typical lunar daytime temperatures (Green et al., 2011). Diviner emission observations have revealed an apparent wavelength dependence of surface brightness temperatures which has been attributed to sub-pixel anisothermality due to surface roughness (Bandfield et al., 2015). Surface slopes smaller than the instrument

spatial resolution can have large temperature differences between sun and anti-sun facing slopes, causing the observed emission to deviate from that of an ideal blackbody emitter (Bandfield & Edwards, 2008; Bandfield et al., 2015). These sub-pixel anisothermalities are insidious on the Moon due to the lack of an atmosphere and low regolith thermal inertia, allowing centimeter-scale slopes to remain thermally isolated with ∼100s of K temperature difference (Bandfield et al., 2015). Therefore, accurately predicting radiated emission from a rough surface at a particular wavelength (e.g., 3 µm in M^3 observations) necessitates the use of a roughness-based thermal model (Bandfield & Edwards, 2008; Bandfield et al., 2018).

Here, we present a model with key updates to the Bandfield et al. (2018) roughness thermal model which combines a new rough surface raytracing shadowing model than can be coupled with an arbitrary thermal model to predict emission at a range of viewing geometries and wavelengths. Previous iterations of the model assumed surface radiative equilibrium and were therefore limited to regions of airless bodies with near-equilibrium conditions (e.g., the lunar equator near midday;Bandfield et al. 2015, 2018). Here, we couple our generalized raytracing shadow model with the open source KRC 1D heat diffusion thermal model (Kieffer, 2013) to predict emission across a wider range of illumination conditions than previously possible. We describe both halves of the combined model below.

3.3.1 Roughness Shadowing Model

We generalize the raytracing roughness shadowing model of Bandfield et al. (2018) which assumes the Moon is a Gaussian rough surface (e.g., Shepard et al. 1995; Helfenstein & Shepard 1999; Bandfield et al. 2015; Wöhler et al. 2017). We generate synthetic self-affine (fractal) rough surfaces using the power spectral density formulation of roughness (Jacobs et al., 2017). Importantly, this generalized technique produces smooth random topography and is scale-invariant, eliminating artifacts due to an imposed length scale or pixel resolution. Adjusting the scale height of the surface alters the degree of roughness and we parameterize surface roughness as the commonly used root-mean-square (RMS) slope of the surface (Shepard et al., 1995; Bandfield et al., 2015; Wöhler et al., 2017). Scaling the rough surface to different RMS values, we then employ a vectorial ray tracing routine to determine the shadowing conditions over a range of solar geometries (Corripio, 2003).

Ray tracing routines are critical to determining the shadowing conditions at high latitudes/incidence angles due to the propensity of cast shadowing (shadows cast by other surface slopes), as opposed to geometric shadowing (the sun dipping below a facet's local horizon, i.e., solar incidence angles $> 90°$). We follow the method of Bandfield et al. (2018) and use our ray tracing routine to produce a statistical shadowing lookup table relating surface roughness (RMS) and solar incidence to the probability of a surface facet with a given

orientation being in shadow. Shadow predictions are binned by facet slope (0°–90°) and azimuth (0°–360°) in 2 and 10-degree increments, respectively. The routine was repeated to produce a regularly-gridded lookup table for synthetic rough surfaces ranging in RMS from 0° (flat) to 50° (very rough) and spanning solar incidence angles from 0°–90° in 5-degree increments. Due to symmetry of the random rough surface, solar azimuth is degenerate and can be predicted in 360° as a simple azimuthal rotation of the lookup table at a given solar incidence. The step sizes of the table were chosen such that it is smooth and shadowing conditions at a precise solar geometry and RMS roughness can be linearly interpolated from the lookup table. With this lookup table, the rough surface is parameterized by 450 facet slope and azimuth bins, each with a probability of being shadowed from a particular solar geometry. To produce the total surface emission, we retrieve the probability of each facet being shadowed and then must predict a temperature for each, given the local solar geometry and surface roughness.

3.3.2 Thermal Model

Here, our generalized raytracing shadow model is coupled with the open source KRC 1D heat diffusion thermal model (Kieffer, 2013) to predict emission across a wider range of illumination conditions than previously possible. KRC (`https://krc.mars.asu.edu/`) is an efficient and widely used long-heritage thermal model that allows us to model key lunar thermophysical properties like temperature-dependent conductivity and specific heat capacity, subsurface layering, density gradients (h-parameter), etc. KRC may also be tuned to various solar system bodies including Mars, small bodies and icy satellites and therefore the methodology presented here can be readily extended to roughness investigations of other bodies. We assess the effectiveness of the KRC thermal model for lunar temperature predictions through comparisons to Diviner observations.

To predict the total thermal emission of a rough surface given a particular geometry, we must predict the temperatures of all surface facets under a range of illumination conditions. Our model assumes that each facet is thermally isolated and therefore conduction between facets is negligible (on the Moon, this occurs at the cm-scale;Bandfield et al. 2015). We may then use an arbitrary thermal model to predict the temperature of each facet (binned by slope and azimuth as above) and sum the emission contribution of all facets under a given set of surface and illumination conditions. Here, we use the open source KRC 1D heat diffusion thermal model (`https://krc.mars.asu.edu/`Kieffer 2013). KRC is an efficient and widely used long-heritage thermal model that allows us to model key lunar thermophysical properties like temperature-dependent conductivity and specific heat capacity, subsurface layering, density gradients (h-parameter), etc. KRC may also be tuned to various solar system bodies including Mars, small bodies and icy satellites and

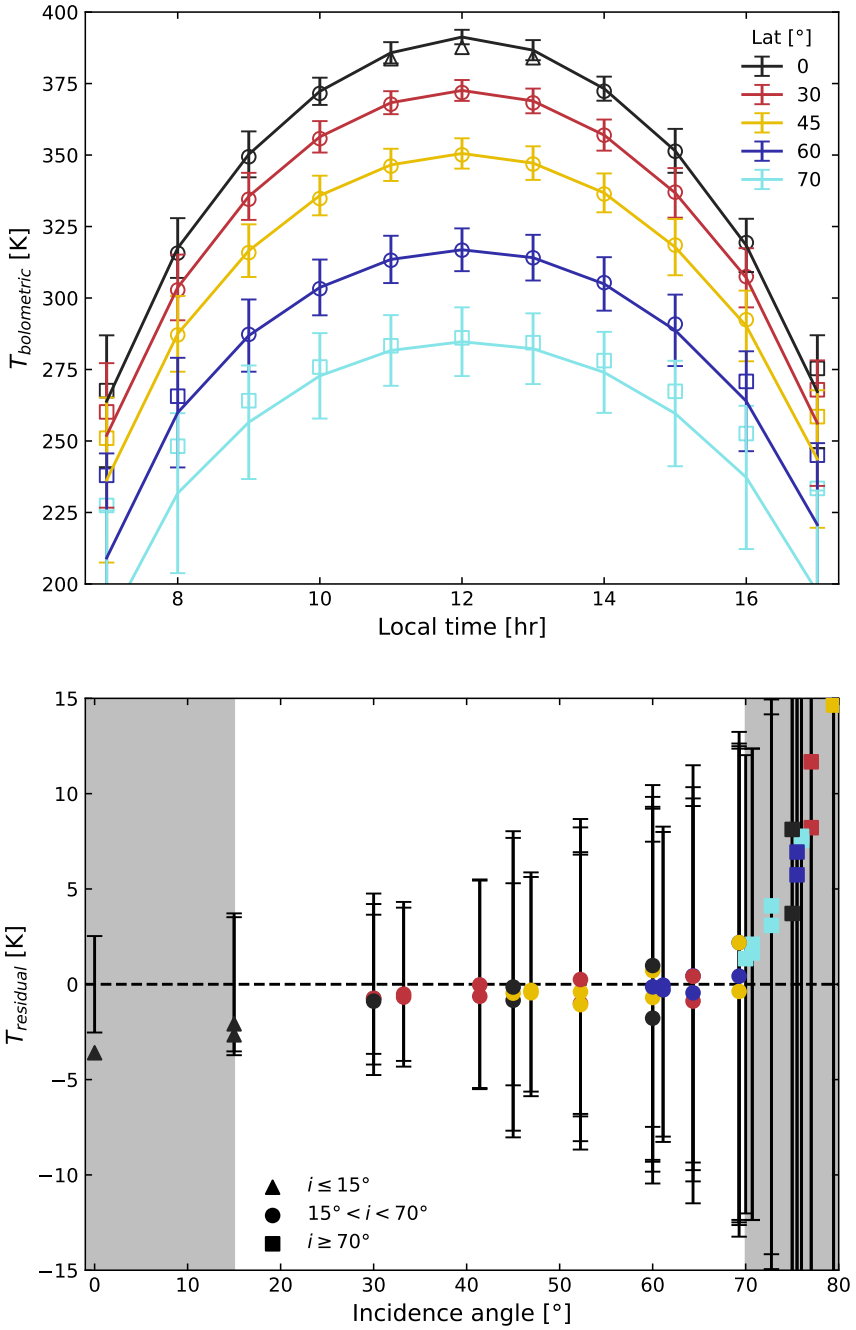

Figure 3.2: Bolometric temperatures (top) and residuals from Diviner (bottom) predicted by the roughness thermal model. Points indicate model predictions while lines and errors indicate global mean and standard deviation Diviner bolometric temperature (Williams et al., 2017). The model may underpredict temperature at low incidence angles ($i \leq 15°ee$; triangles), where Diviner temperatures have been noted to be higher than anticipated (Vasavada et al., 2012), and the model overpredicts at high incidence ($i \geq 70°ee$; squares), where cast shadows are more influential.

therefore the methodology presented here can be readily extended to thermal roughness investigations of other bodies. We construct a 2-layer model in KRC with model parameters drawn from recent observations of lunar surface properties (Hayne et al. 2017; Feng et al. 2020). See Table B.1 in Appendix B for full list of KRC model parameters.

For computational efficiency, we use KRC to produce a lookup table of facet temperatures across a range of illumination conditions and surface properties. The lookup table consists of diurnal surface temperature predictions (0–24 hours local time, 60 steps per hour) across a range of albedos (0.04–0.24 in steps of 0.02), latitudes (-85°–85° in 5° increments), solar longitudes (L_s; 0°–360° in 4° increments), surface slope (0°–90° by 5° increments) and surface azimuth (0°–360° by 20° increments). At runtime, we linearly interpolate between these these nearly 2 billion pre-computed surface temperatures to predict the precise facet temperature of each slope/azimuth combination given local time, latitude and L_s, and albedo.

To predict the temperatures of shaded surface facets, we must distinguish between geometric and cast shadows. Facets oriented >90° from from the sun are in geometric shadow (pre-sunrise or post-sunset) and are simply assigned the KRC-predicted nighttime temperature at the facet local time. However, our temperature lookup table cannot predict the temperature of facets in cast shadow (facets which would otherwise be illuminated but lie in the shadow of a taller facet). For facets in cast shadow, we apply a simple cooling approximation based on the average fraction of the day, f, that a facet remains in shadow. We may then compute the time spent in shadow, t_{illum} as:

$$t_{illum} = f \cdot (t_{loc} - t_{dawn}) \tag{3.1}$$

where t_{loc} is the facet local time and t_{dawn} is facet sunrise time. The cast shadow temperature at t_{loc} is then assumed to be cooled linearly from its last illuminated temperature to its minimum daytime temperature:

$$T_{cs} = f \cdot T(t_{illum}) + (1 + f) \cdot T(6) \tag{3.2}$$

This is a simple first order approximation for the aggregate cooling behavior of facets in cast shadow. However, facets may move into and out of shadow several times throughout a lunar day or cool below the minimum facet temperature if remaining in cast shadow for most of the lunar day (particularly true of permanently shaded regions near the lunar poles which are in perpetual cast shadow and would be much colder than T_{cs}). We find that f=1% results is appropriate temperature predictions across much of the lunar surface (Figure 3.2). Long cast shadows in the polar regions are primarily due to macroscopic topography rather than cm-scale roughness and are therefore outside the scope of this work.

Finally, total radiated emission is computed as the weighted sum of emission from each illuminated and shadowed facet bin. We compute the Planck emission as a function of wavelength of each facet assuming each is a Lambertian surface with an emissivity of 0.96 (Hayne et al., 2017). We then weight each facet bin by its shadow probability and probability of occurring at the chosen RMS roughness level. We also apply a correction for the areal fraction of each facet visible from the spacecraft as the cosine of the angle between each facet and the spacecraft emission vector, such that facets oriented away from the spacecraft do not contribute and those oriented directly towards the detector contribute the most. Finally, we maintain the re-radiation approximation developed in Bandfield et al. (2018) to account for emission between facets. The result is an emitted radiance spectrum which accounts for lunar surface roughness.

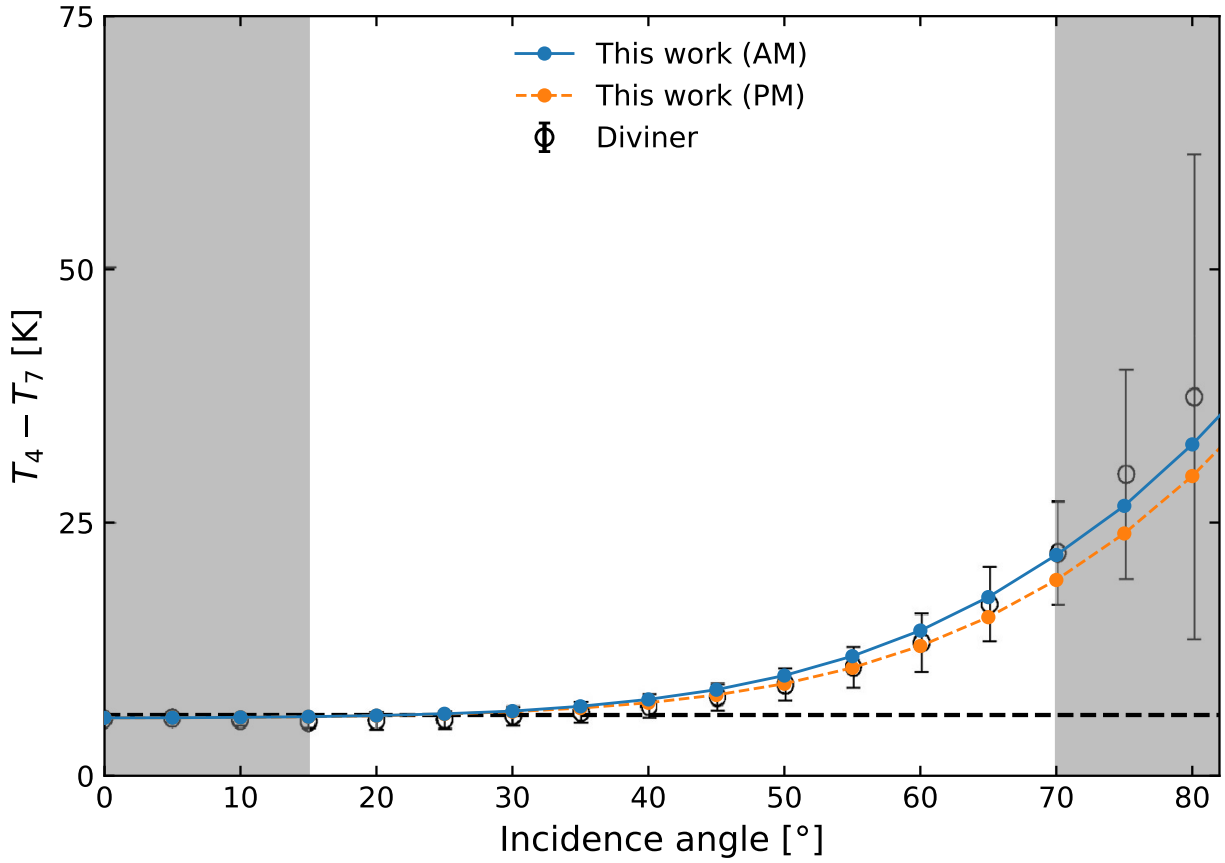

Figure 3.3: Equatorial model predicted (morning, blue; afternoon, orange) over Diviner observed (black) anisothermality (channel 4 – channel 7 brightness temperature;Williams et al. 2017). The roughness thermal model accurately predicts the onset of anisothermal effects with increasing incidence well within Diviner standard deviations.

3.3.3 Model Validation Approach

We validate the updated roughness thermal model through comparisons to thermal observations from the Diviner lunar radiometer (Paige et al., 2010b). To test model performance at a range of latitudes and incidence angles, we compare model temperatures to the Williams et al. (2017) Diviner global average bolometric temperatures (Figure 3.2). We simulate global average temperatures by predicting rough emitted radiances for 7–17h local time in 1-degree latitude / longitude bins with albedos drawn from a published global thermal albedo map (Feng et al., 2020). RMS roughness and emissivity were held constant at 19° and 0.96, respectively (Bandfield et al., 2015, 2018). For comparison, we convolved our predicted emitted radiance spectra with the Diviner filter functions to predict individual channel 3 through 9 (spanning 7.8–400 µm) brightness temperatures (Paige et al., 2010b). From the brightness temperatures, we also computed Diviner-like broadband bolometric temperature with the standard formula described in Paige et al. (2010a). We also compute anisothermality as the difference between predicted channel 4 and channel 7 brightness temperatures. Diviner channel 4 (8 µm, near the peak of lunar daytime emission) and Diviner channel 7 (25–41 µm, thermal IR) are well suited for measuring anisothermality (Bandfield et al., 2015) and we compare our model predictions to the Williams et al. (2017) channel 4 minus channel 7 globally averaged measurements (Figure 3.3).

3.3.4 Application to M^3 data

To process M^3 spectra, we use the updated USGS and Boardman 2017 ("Step-2") geometry (Gaddis et al., 2016; Malaret et al., 2019) to determine the local solar incidence, azimuth and spacecraft emission and azimuth angles. We adopt a constant RMS roughness value of 19° and emissivity of 0.96 which accurately predict Diviner anisothermality across a range of latitudes and incidence angles (Figures 2–3). We draw hemispherical thermal albedo linearly interpolated from the microwave albedo maps produced by (Feng et al., 2020). We then run our roughness thermal model to predict radiated emission given the albedo and bidirectional geometry of each pixel of M^3 data. To produce an unbiased independent estimate of emission, we assume a constant emissivity of 0.96 which best matched Diviner observations (Figures 1-2) rather than deriving emissivity from the spectrum by assuming Kirchoff's Law (Bandfield et al., 2018; Wöhler et al., 2017). We then subtract the model-predicted radiated emission at each wavelength from the total M^3 level 1 radiance and apply the standard M^3 photometry and statistical polishing steps to derive reflectance values directly comparable to PDS level 2 reflectance (as generated by the Clark et al. 2011 method). These thermally corrected spectra are then used to investigate the variability of the 3 µm feature across latitude and local time.

3.4 Results

3.4.1 Model Validation

Our roughness thermal model accurately predicts Diviner bolometric temperatures (Williams et al., 2017) across a range of roughness conditions (Figure 3.2). Our predictions are consistent to 2 K spanning negligible roughness (∼15° incidence) to high roughness conditions (∼70° incidence). Our model may under-predict Diviner bolometric temperatures at low solar incidence (<15°), where Diviner observations exceed expected tempertures at radiative equilibrium, perhaps due to directional emissivity effects (Vasavada et al., 2012). Our model prediction exceed Diviner bolometric temperatures at solar incidence angles larger than 75°, where large-scale topographic effects (larger than the cm-scale roughness modeled here) begin to dominate the shadowing conditions of the surface. A key assumption of this work is that macro-scale topography is not the dominant cause of the anisothermality since this would necessitate localized raytracing, which is outside the scope of this work. We indicate plot regions outside the primary model domain ($15° < inc < 70°$) with shading for the remainder of this work (e.g. Figure 3.3).

Although Diviner bolometric temperatures approximate the kinetic temperature of the surface under nighttime or low roughness conditions, they mask the wavelength-dependent emission introduced by subpixel anisothermality in daytime observations. Assuming an emissivity of 0.96 and an RMS roughness value of 19°, our roughness thermal model predicts the onset and magnitude of Diviner channel 4 and channel 7 brightness temperature differences reported by Williams et al. (2017), well within standard deviations (Figure 3.3). We note that the anisothermality is asymmetric around noon, yielding greater residuals in the morning relative to the afternoon. The global averages of Williams et al. (2017) also exhibit much more scatter at incidences larger than 75°, indicating macro-scale shadowing effects are more significant than global roughness effects at very high incidence. Therefore, we find good agreement in predicted bolometric temperature and anisothermality up to ∼75° solar incidence.

We compare our model-predicted 3 µm brightness temperatures to those predicted by previous M^3 thermal corrections (Figure 3.4). We removed topography >15° and chose a mare region that had repeat coverage by M^3 at multiple local times. We show each correction as a residual from Diviner channel 4 brightness temperature queried within 0.5 h of local time. We find that the M^3 level 2 temperatures (Clark et al., 2011) significantly under-predict surface temperature, while Li & Milliken (2017) and (Wöhler et al., 2017) are comparable to Diviner observations. The roughness thermal model presented here predicts higher brightness temperatures than observed by Diviner channel 4 (8.25 µm) in each case. This is expected from the inverse correlation between brightness temperature and wavelength due to anisothermal effects introduced by roughness (Bandfield et al., 2015).

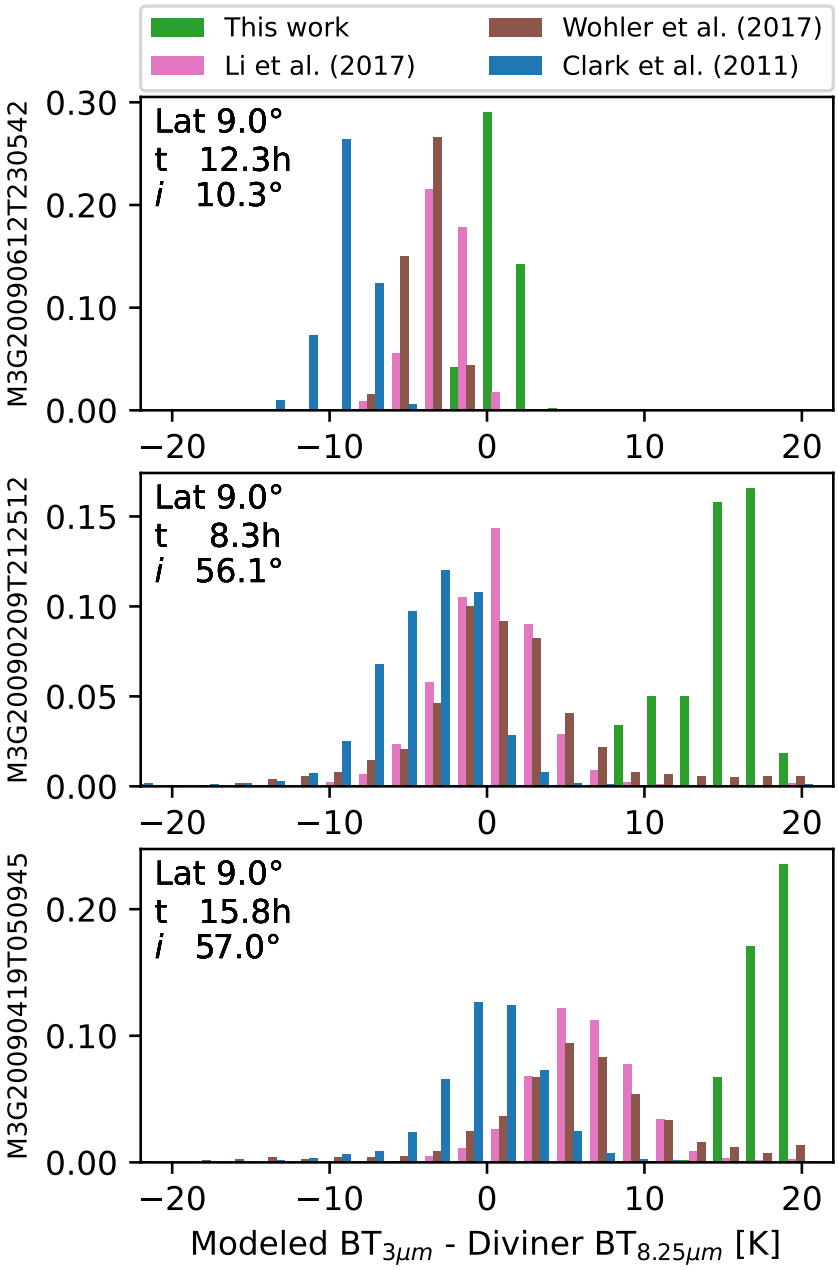

Figure 3.4: Residuals of modeled 3 µm brightness temperature from this work and 3 previous studies relative to Diviner 8.25 µm (channel 4) brightness temperature. The roughness thermal model predicts higher brightness temperatures at 3 µm relative to 8.25 µm, consistent with a negative trend in brightness temperature with increasing wavelength (Bandfield et al., 2015). Brightness temperatures computed by three previous M^3 thermal corrections are consistently lower than those predicted here (Clark et al., 2011; Li & Milliken, 2017; Wöhler et al., 2017).

3.4.2 Corrected M^3 Data

We apply our validated roughness thermal model to correct M^3 observations at a variety of solar incidence angles and latitudes to evaluate variability in the 3 µm feature. We compute the 3 µm integrated band depth ($IBD_{3\mu m}$) used previously to look for variation in the M^3 3 µm feature (Wöhler et al., 2017; Grumpe et al., 2019). We compute $IBD_{3\mu m}$ consistently with Grumpe et al. (2019) as the integrated area below channels 78–84 (2.697–2.936 µm) after removal of a linear continuum fit to channels 74–77 (2.537–2.657 µm), expressed as a percentage. While useful for comparing relative strength, we note that this band depth should not be interpreted as the maximum depth of the feature since M^3 did not have the spectral range to sample the entire 3 µm feature. spectral range. A direct comparison of $IBD_{3\mu m}$ reveals a much stronger absorption than that derived by Li & Milliken (2017), both in the morning and at midday (Figure 3.5). We compute the average $IBD_{3\mu m}$ across latitude and local time and observe a strong feature which appears invariant with latitude and solar incidence angle within standard deviations (Figure 3.6).

3.5 Discussion

3.5.1 Lunar Surface Roughness and Directional Emissivity

The updated roughness thermophysical model presented here accurately predicts Diviner bolometric temperatures and anisothermality as viewed at nadir with solar incidence angles from 15° to ∼70°. A uniform RMS roughness of 19° and emissivity of 0.96 appears to best fit Diviner bolometric temperatures as well as channel 4 minus channel 7 anisothermality (Williams et al., 2017). These parameters are nearly identical to the 0.95 emissivity and 18° RMS used in the earlier iteration of this model (Bandfield et al., 2018). However, our updated shadowing and 1D thermal model extend the model domain to higher latitudes and local times (up to ∼70° between local times 7-17h). Notably, the roughness derivation in our model is smaller than values derived by Rubanenko et al. (2020) who used analytical expressions of directional emissivity on gaussian rough surfaces at radiative equilibrium to derive averages of 30° and 37° roughness values for the maria and highlands, respectively. The lower roughness predicted by our model may be due to the difference in emissivity between the two models; while Rubanenko et al. (2020) took a directional emissivity approach, our model aimed to model nadir-observed anisothermality as purely a function of roughness at constant emissivity. It has also been suggested that the thermal excess observed in low incidence nadir Diviner observations is due to directional emissivity (Vasavada et al., 2012), which may explain the our model underpredicting bolometric temperature at low incidence (Figure 2). The ongoing Diviner Emission Phase Function off-nadir observation campaign (Warren et al., 2021) aims to better quantify the directional emissivity of the lunar

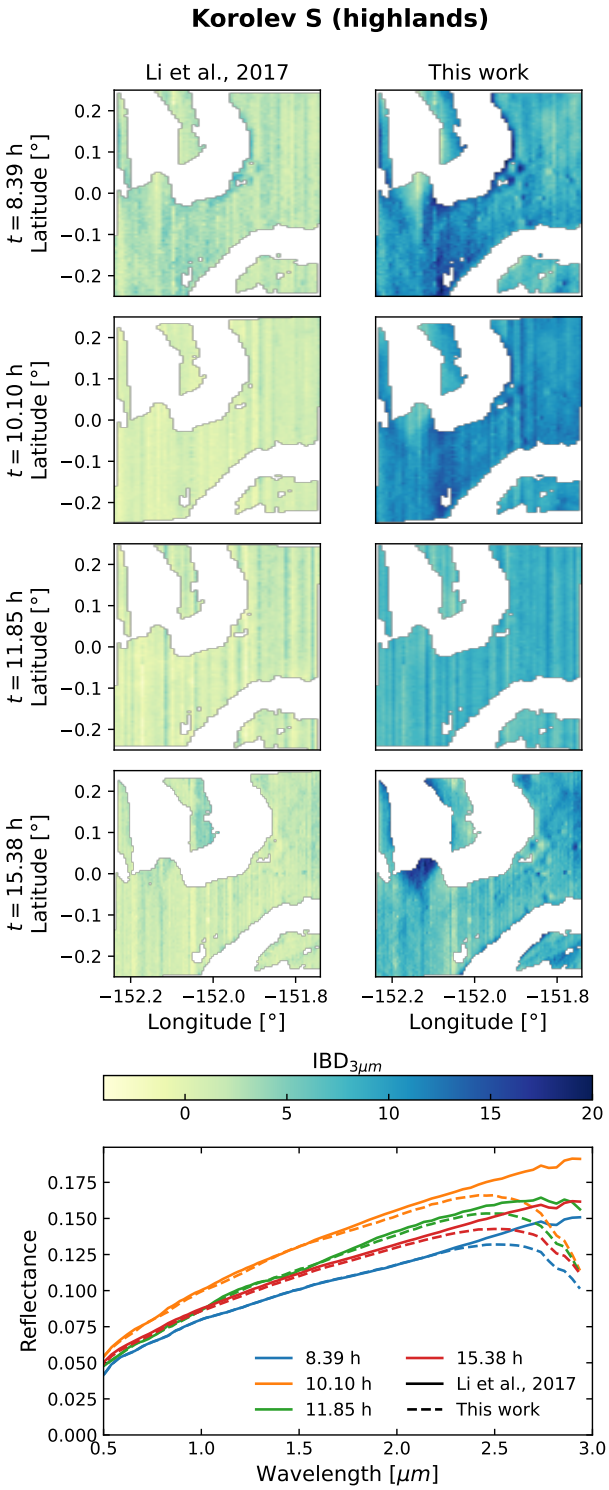

Figure 3.5: $IBD_{3\mu m}$ at multiple local times in M^3 data thermally corrected by Li & Milliken 2017 (left) and this work (right). Regions with large topographic slopes (>15°) are excluded. Mean spectra across the scene show deeper 3 µm absorptions in roughness-corrected spectra at all local times.

surface which will be a boon to this and similar bidirectional thermal models in the future.

3.5.2 Limitations of predicting temperature at 3 µm

We apply our roughness thermal model to predict the brightness temperature at 3 µm to independently constrain the thermal emission relevant to M^3 spectra. At present, the emission characteristics of the lunar surface at 3 µm are poorly understood, due in part to 3 µm being a critical region where lunar surface radiance transitions from reflectance-dominated to emission-dominated at typical daytime temperatures (Figure 3.1). We also lack spacecraft observations with the range of incidence and phase angles needed to constrain directional emission effects at 3 µm. Furthermore, although M^3 has the greatest spatial coverage to date, it lacks the spectral range to isolate the 3 µm feature and predict temperature from the onset of the emission tail longwards of 3 µm.

Unlike previous corrections, our approach to predicting 3 µm emission is an independent physics-based emission model. The emission at a particular wavelength is the weighted sum of emission from sub-pixel facets at a given orientation to the sun and the detector and a probability of being shaded. Assuming that these cm-scale rough surface facets are Planck-like emitters with constant emissivity, the model reproduces the bolometric and anisothermal temperature differences observed by Diviner and is therefore well validated from orbit at thermal infrared wavelengths. Our model-predicted brightness temperatures at 3 µm rely on the simple assumption that roughness behaves similarly in the near-infrared as it does in the thermal infrared. Since the thermal skin depth is shallower at 3 µm than at 8^+ µm, our Diviner-derived RMS roughness may differ from the roughness influencing emission at 3 µm. However, Guo et al. (2021) found that roughness appears to increase at sub-centimeter length scales. Therefore, our

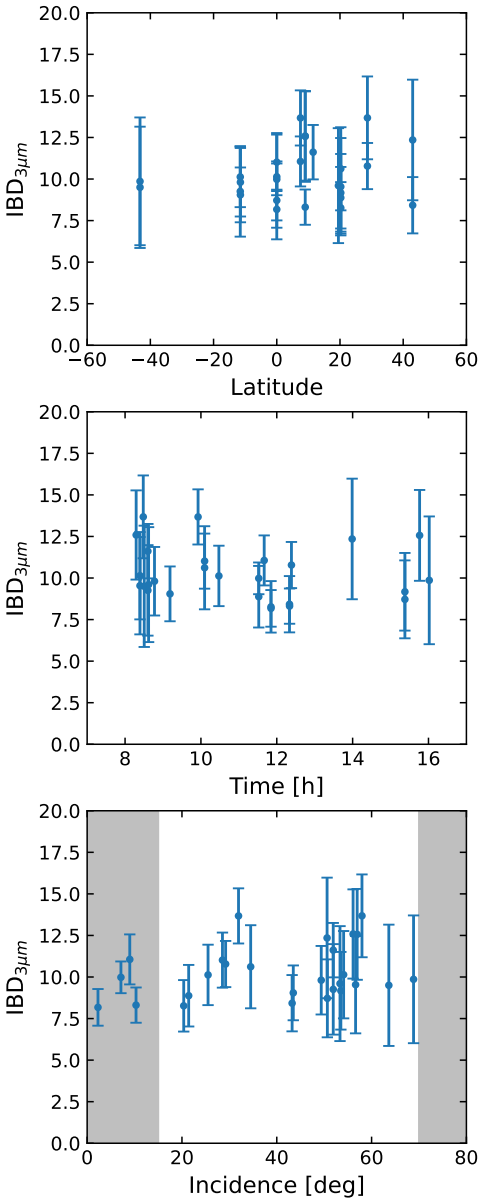

Figure 3.6: IBD$_{3\mu m}$ from roughness-corrected M^3 spectra averaged across latitude and local time. We find no significant increase in IBD$_{3\mu m}$ with latitude, local time, or solar incidence angle.

derivation of the 19° RMS slope roughness derived from Diviner wavelengths is a conservative estimate of roughness at 3 µm and greater roughness values would produce larger anisothermal effects than those reported here. If future near-infrared observations reveal negligible anisothermal effects in the 3–5 µm region, an updated physical mechanism would be required to explain the surprising homogeneity in the near-infrared despite the well-established anisothermal effects observed at longer wavelengths.

Ongoing and planned missions may offer insights into surface emission characteristics at 3 µm. Initial results from the Chandrayaan-2 IIRS spectrometer appear to show a lack of anisothermality in the 4.5–4.85 µm region (Chauhan et al., 2021; Verma et al., 2022). When an isothermal temperature derived at these wavelengths is applied to remove emission at 3 µm, IIRS data appear to show a more prominent 3 µm feature with increasing latitude, similar to observations of Li & Milliken (2017) and contrary to the observations reported here. Notably, our roughness thermal model is in agreement, predicting negligible anisothermality between 4.5 and 4.85 µm (black line; Figure 3.7). However, when predicting anisothermality between 3 and 4.5 µm, our roughness thermal model predicts 1–10 K of anisothermality, increasing with incidence angle (dashed line; Figure 3.7). Therefore, the isothermal correction described in Verma et al. (2022) may not capture roughness effects at high solar incidence angles, resulting in a variable 3 µm feature with latitude. Upcoming missions like Lunar Trailblazer (Ehlmann et al., 2022) will collect co-boresighted observations in the near- and thermal-infrared under a variety of bidirectional geometries. Such missions will be critical for characterizing roughness effects at 3 µm and unambiguously investigating the behavior of widespread OH/H_2O on the lunar surface.

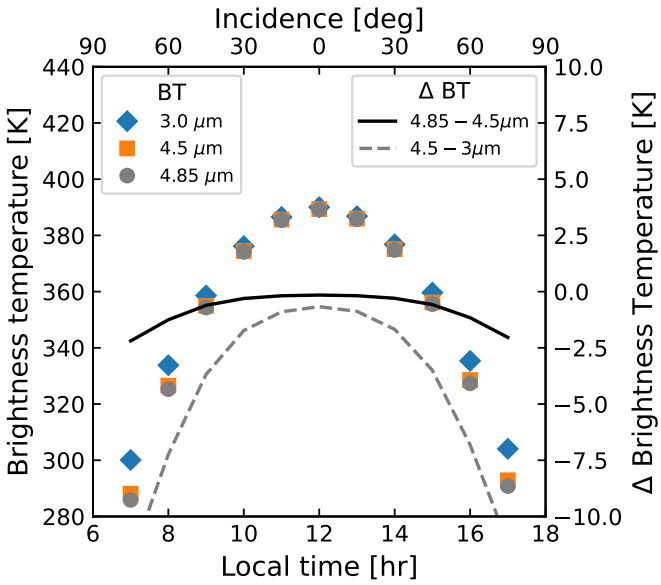

Figure 3.7: Equatorial model-predicted brightness temperatures at 3, 4.5, and 4.85 µm over local time. The surface is nearly isothermal (< 1 K) for incidence angles < 45° in the 4.5–4.85 µm range (black line). However, larger anisothermality is predicted between 4.5 and 3 µm, increasing with incidence (dashed line).

3.5.3 Comparison with previous 3 µm predictions

Independent thermal corrections of M^3 data have resulted in a range of interpretations of the diurnal nature of the 3 µm feature, spanning fully mobile to fully static. The aim of each thermal correction is to remove emission at 3 µm, therefore we compare the 3 µm brightness temperatures (or the derived 3 µm brightness temperature inferred from the total removed emission). Relative to the original PDS Level 2 thermal correction (Clark et al., 2011), we found a greater 3 µm brightness temperature across all conditions, similarly to previous updated M^3 thermal corrections (Figure 3.4). We find that our radiance predictions result in apparent 3 µm brightness temperatures that are consistently higher than previous corrections and Diviner 8.25 µm brightness temperatures. In Figure 3.5, we compared $IBD_{3\mu m}$ predicted by our roughness thermal model and the thermal correction of Li & Milliken (2017). Since our model predicts greater radiance in general, we observe a stronger 3 µm absorption both spatially and temporally than Li & Milliken (2017). In general, $IBD_{3\mu m}$ predicted by our model (5–15%) is in agreement with the range reported by Wöhler et al. (2017); Grumpe et al. (2019), indicating consistency between our approaches to correcting for roughness. However, Grumpe et al. (2019) reported a partially mobile 3 µm feature and lower $IBD_{3\mu m}$ in the maria. In contrast, our model predicts no significant variation in $IBD_{3\mu m}$ across all local times, latitudes and in both the mare and highlands regions modeled here (Figure 3.6).

3.5.4 The nature of widespread lunar OH / H_2O

Our model predicts a deep, prominent 3 µm absorption feature throughout the lunar day that has previous been attributed to OH at crystal defect sites (Bandfield et al., 2018). In contrast, Li & Milliken (2017) found that the 3 µm absorption feature is absent during the day and attributed this to surface H_2O fully mobilizing on diurnal timescales, while Wöhler et al. (2017) reported a partially mobile 3 µm feature and inferred that a combination of a tightly locked source and diurnally varying H_2O are responsible. Recently, solar wind irradiation of lunar soils has been shown to produce a deep and broad OH absorption which engulfs the 3 µm region and is stable at high temperature, precluding the need of H_2O to explain the remote observations (McLain et al., 2021). However, independent confirmation that some part of the 3 µm feature is likely due to H_2O recently came in form of SOFIA observations which observed the diagnostic 6 µm emission feature attributed to H_2O rather than OH (Honniball et al., 2020). As such, the relative contributions of OH and H_2O to the 3 µm feature remain unclear. Our observations support a strong 3 µm feature which does not vary on diurnal timescales. This could indicate solar-wind-induced OH dominates any observable H_2O signature in the 3 µm spectral region, or that a combination of strongly bound OH and H_2O both contribute. Our observations are ambiguous with respect to the source of the 3 µm feature, but future work

correlating the remote 3 and 6 µm features or in-situ measurements of OH and H_2O content of the regolith would help resolve this outstanding question.

3.6 Conclusions

Interpretations of the lunar 3 µm OH / H_2O feature have varied depending on the approach used to remove thermal emission from Moon Mineralogy Mapper (M^3) observations. Surface emission is complicated by anisothermality below the M^3 spatial resolution due to surface roughness. At moderate solar incidence angles and latitudes, roughness causes observed surface emission to vary as a function of wavelength and incidence angle, due primarily to local shadowing conditions below the detector resolution. We update and generalize the roughness thermal model developed by (Bandfield et al., 2015, 2018) to accurately predict and remove emission from M^3 spectra.

The roughness thermal model described here accurately reproduces Diviner temperature observations across a range of latitudes and local times in 15°–70° of solar incidence. The model combines a raytracing shadowing model with a 1D thermal model to predict the illumination conditions and temperatures of sub-pixel surface elements. The roughness open-source Python model (Tai Udovicic et al., 2021b) has been generalized to be applicable to any rough planetary surface with Gaussian roughness. At extreme incidence angles $> 70°$ (e.g., at dawn/dusk or near the poles), large-scale topography begins to dominate local shadowing conditions, which would necessitate a targeted rather than the statistical approach to roughness modeling presented here.

M^3 spectra corrected with our roughness thermal model contain a deep and broad 3 µm absorption feature which persists across all observed local times and latitudes. With no observed diurnal variability, our results favor a strongly bound source of the OH / H_2O feature. While this model was validated with and applied to nadir observations, new observations are needed to constrain the directional characteristics rough airless surfaces, particularly in the near-infrared. Our results indicate that surface roughness is an important consideration when interpreting infrared observations of planetary surfaces and bi-directional effects of roughness should be incorporated into future thermal emission models.

3.7 Open Research

The `roughness` Python package is open source and publicly available on GitHub (`https://github.com/NAU-PIXEL/roughness`) for use under the MIT license (`https://doi.org/10.5281/zenodo.5498089`; Tai Udovicic et al. 2021b). Data and code required to reproduce each figure is available from TBD. Moon Mineralogy Mapper (M^3) and Diviner Lunar Radiometer data are available from the Planetary Data System

(https://pds.nasa.gov/).

3.8 Acknowledgements

This work was supported by the NASA Lunar Data Analysis Program (15-LDAP15_2-0023, PI: Bandfield, Subsequent PI: Farrand). The authors would like to thank L. Gaddis, S. Li, C. Wohler, K Wohlfarth and the Diviner Team for assistance accessing and processing the data used in this work.

Chapter 4

Manuscript III: Buried Ice Deposits in Lunar Polar Cold Traps were Disrupted by Ballistic Sedimentation

Christian J. Tai Udovicic[1], K. R. Frizzell[2], G. R. L. Kodikara[3], M. Kopp[4], K. M. Luchsinger[5], A. Madera[2], M. L. Meier[6], T. G. Paladino[7], R. V. Patterson[8], F. B. Wroblewski[6], D. A. Kring[9,10]

This a preliminary version of an article submitted for publication in Journal of Geophysical Research: Planets. Wiley Inc is not responsible for any errors or omissions in this version of the manuscript or any version derived from it.

4.1 Abstract

The NASA Artemis program will send humans to the lunar south polar region, in part to investigate the availability of water ice and other *in-situ* resources. While trace amounts of ice have been detected at the surface of polar permanently shadowed regions (PSRs), recent studies suggest that large ice deposits could be stable below cold traps in the PSRs over geologic time. A recent study modeling the rate of ice delivery, ejecta deposition and ice loss from cold traps predicted that gigatons of ice could be buried below 100s of meters of crater ejecta and regolith. However, crater ejecta vigorously mix the target on impact through ballistic sedimentation, which may disrupt buried ice deposits. Here, we developed a thermal model to predict ice stability during ballistic sedimentation events. We then modeled cold trap ice and ejecta stratigraphy over geologic time using Monte Carlo methods. We found that ballistic sedimentation disrupted large ice deposits in most cases, dispersing them into smaller layers. Ice retention decreased in most cases, but varied significantly with the sequence of ejecta delivery, particularly from basin-forming events. Over many model runs, we found that south polar craters Amundsen, Cabeus, Cabeus B, and Idel'son L were most likely to retain large deposits of ice shallow enough to be detectable with ground-penetrating radar. We discuss these

[1]Northern Arizona University, Department of Astronomy and Planetary Science, PO Box 6010, Flagstaff, AZ 86011, USA
[2]Rutgers University, New Brunswick-Piscataway, NJ
[3]University of Wisconsin-Milwaukee, Milwaukee, WI
[4]Boston College, Newton, MA
[5]New Mexico State University, Las Cruces, NM
[6]University of Idaho, Moscow, ID
[7]Idaho State University, Pocatello, ID
[8]University of Houston, Houston, TX
[9]Lunar and Planetary Institute, Universities Space Research Association, Houston, TX
[10]NASA SSERVI Center for Lunar Science and Exploration (CLSE)

findings in the context of the imminent human exploration activities at the lunar south pole.

Plain Language Summary

Some craters near the South Pole of the Moon contain permanently shadowed regions (PSRs) which stay cold enough to trap water vapor as ice. Recent studies have predicted that large amounts of ice could be buried under thick protective layers of lunar soil in the PSRs. Lunar soil is mainly transported by large impacts which launch soil and boulders up to hundreds of kilometers. However, when these projectiles land they have destructive effects and may melt or redistribute buried ice. We simulated this process, called ballistic sedimentation, and predicted the amount of ice it removes. We also simulated ice and soil deposits over billions of years to test how much ice is lost to ballistic sedimentation over time. We predicted which PSRs are most likely to have ice near enough to the surface to detect in future missions. The upcoming Artemis program will send crewed and robotic missions to the lunar south pole region, and our work will help with planning where to land, what instruments to bring, and how much ice we might find.

4.2 Introduction

The NASA Artemis program will include crewed and uncrewed missions to the lunar south polar region where water and other volatiles are trapped (NRC et al., 2007). Permanently shadowed regions (PSRs) remain very cold (in some cases, down to 38 K, Paige et al. 2010a) and therefore have the potential to trap volatiles such as H_2O, CO, and S in their solid state. Polar water ice has been detected by a variety of independent spectroscopic techniques in addition to the Lunar Crater Observation and Sensing Satellite (LCROSS) impact experiment at Cabeus crater (Colaprete et al., 2010; Li et al., 2018; Hayne et al., 2015). Lunar water ice is a valuable science target for its potential to constrain early sources of water to the Earth-Moon system and to investigate the evolution of those reservoirs throughout Solar System history (NRC et al., 2007). It may also play a critical role as an *in-situ* resource utilization (ISRU) target for supporting a sustained human presence on the Moon (i.e., to support human life or as a source of hydrogen and oxygen to produce other compounds, e.g., rocket propellant; Kornuta et al. 2019).

Lunar polar water ice has been theorized for decades (Watson et al., 1961; Arnold, 1979), but has only recently begun to be characterized, primarily by remote sensing observations (see Lucey et al. 2021 for a review). Remote spectroscopic studies have suggested trace amounts of polar water (e.g., Hayne et al. 2015; Li et al. 2018), but not in massive surface ice deposits like those found at the poles of Mercury (Moses et al., 1999). Neutron spectroscopy uncovered a polar hydrogen enhancement in the upper meter of regolith, suggesting up to 1% ice content if water is solely responsible (Feldman et al., 2001; Miller et al., 2014).

Radar initially failed to find evidence of subsurface ice deposits (Campbell et al., 2006; Neish et al., 2011), but later found backscatter consistent with increased roughness or ice in the upper meters of PSR regolith (Spudis et al., 2013). The only diagnostic detection of subsurface polar water ice was recorded during the LCROSS experiment in which an expended Centaur rocket impacted and ejected material from depths of 6 to 10 meters below the Cabeus PSR (Korycansky et al., 2009; Colaprete et al., 2010; Schultz et al., 2010; Hermalyn, 2012; Luchsinger et al., 2021). Other studies have also inferred the presence of subsurface ice based on geomorphology and roughness of PSR surfaces (Deutsch et al., 2020; Moon et al., 2021). Despite clear evidence that water ice exists at the lunar poles, key questions remain as to the source, distribution, and abundance of ice, both at the surface and potentially buried in the subsurface.

Several recent studies estimated the total abundance of potentially stable water in the lunar south polar region, primarily in PSRs (Hayne et al., 2015; Paige et al., 2010a), seasonal cold traps (Williams et al., 2019), and micro cold traps (Hayne et al., 2021). However, no massive ice deposits have been detected at the surface (Li et al., 2018; Haruyama et al., 2008; Bickel et al., 2022), perhaps due to the short stability timescales of surface water ice (Farrell et al., 2019). Water ice in the upper meters is also susceptible to loss via impact gardening, the net disruptive effect of small impacts into the lunar surface, over geologic timescales (Costello et al., 2021). A mechanism for preserving ice at greater depths was proposed by Kring (2020) who recognized that surface ice deposits would be blanketed by ejecta from neighboring craters and thus remain protected from surface loss. Several punctuated episodes of ice and ejecta deposition could then lead to a stratigraphic sequence that would remain relatively pristine in the absence of resurfacing processes other than impact cratering.

The first model investigating ice and ejecta stratigraphy at the lunar poles was developed by Cannon et al. (2020). Through a Monte Carlo approach, they showed that ejecta blanketing of cold traps could preserve mining-scale ice deposits over geologic time. However, that work neglected the effects of ballistic sedimentation, the vigorous mixing of ejecta with local materials, which may rework and volatilize ice rather than strictly preserving it (Kring, 2020). In this work, we seek to understand the effects of ballistic sedimentation on lunar polar ice and ejecta stratigraphy. In order to address this question, we developed a simple thermal model to account for volatilization in a particular ballistic sedimentation event. We then developed a Monte Carlo polar ice and ejecta stratigraphy model using the same framework of Cannon et al. (2020). In addition to ballistic sedimentation, we use the model to explore the effects of basin impacts, cometary impactors, and solar wind ice deposition. We predict ice retention at key cold trap locations in the Artemis exploration zone and discuss the potential for subsurface ice exploration near the lunar south pole.

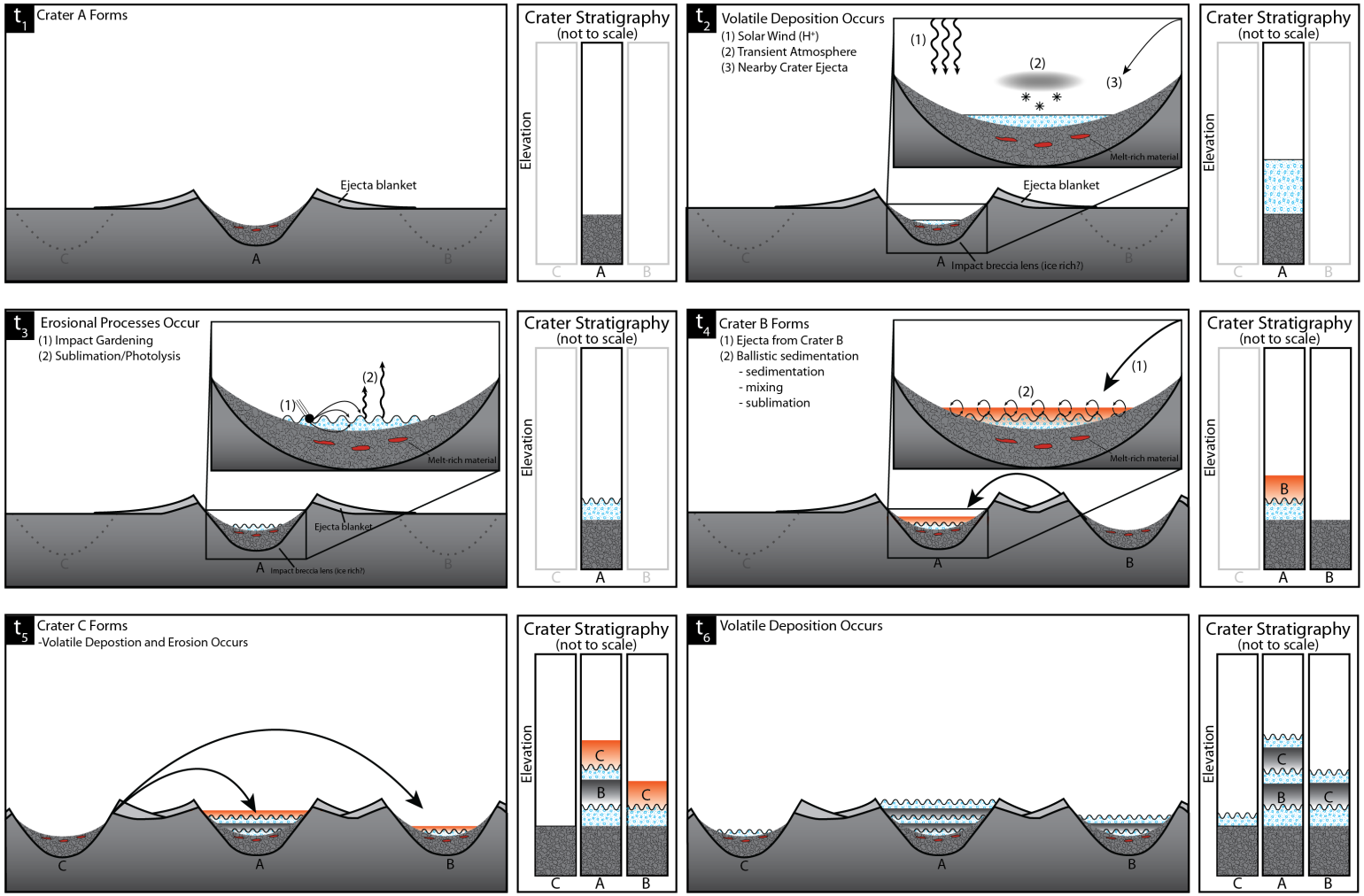

Figure 4.1: Sequence of events resulting in layered stratigraphy in lunar south pole craters. Greyed out stratigraphy columns indicate that the column/crater does not yet exist. Notice how the presence and thickness of layers change with time as craters are formed and geologic events occur. We do not include ice modification processes in this figure or in the MoonPIES model.

4.3 Methods & Modules

Moon Polar Ice and Ejecta Stratigraphy (MoonPIES) is a Monte Carlo model designed to simulate lunar polar cold trap stratigraphy resulting from ice delivery, ejecta deposition, and ice removal at the lunar poles. Our model extends a previous model by Cannon et al. (2020) by introducing basin-scale impacts, ballistic sedimentation effects, latitude dependent ballistic hop efficiency, and cometary impactors.

4.3.1 Main model

We developed the MoonPIES model to track ice and ejecta layering within permanent cold traps over lunar geologic time, recording ice delivered, ice lost, and ejecta deposited to target cold traps in 10 Myr intervals. We limited our study to south polar cold traps found within large permanently shaded craters (Cannon et al., 2020). Each cold trap was modeled as a 1D column of unit area at the centroid of its permanently shadowed area (Data Set S1, Appendix C).

At each timestep following its formation age, a given cold trap stratigraphy column was updated in the following order:

1. Ejecta deposited from basins and craters (possible ballistic sedimentation)
2. Ice deposited (see processes, Figure 4.1)
3. Ice removed due to impact gardening (§4.3.7)

We ran the full MoonPIES Monte Carlo model from 4.25 Ga to the present 10,000 times to generate a statistical distribution of possible cold trap stratigraphies. Parameters which were varied on each run included the ages of basins and polar craters (Figure 4.2) as well as the amount of impactor ice deposited in each timestep (see §4.3.4).

4.3.2 Ejecta deposition

We modeled ejecta emplacement similarly to Cannon et al. (2020) with the addition of basin events (Figure 4.2). We included 24 south polar complex craters (D >20 km) and 27 basins (D >300 km), each dated previously by crater counting methods (Data Sets S1-S2, Appendix C; Deutsch et al. 2020; Tye et al. 2015; Orgel et al. 2018). We calculated ejecta thickness (t) as a function of distance (r) and crater radius (R) using the scaling relationship from McGetchin et al. (1973); Kring (1995):

$$t = \begin{cases} 0.04 & \text{for simple craters,} \\ 0.14 & \text{for complex craters} \end{cases} \times R^{0.74} \left(\frac{r}{R}\right)^{-3.0 \pm 0.5} \tag{4.1}$$

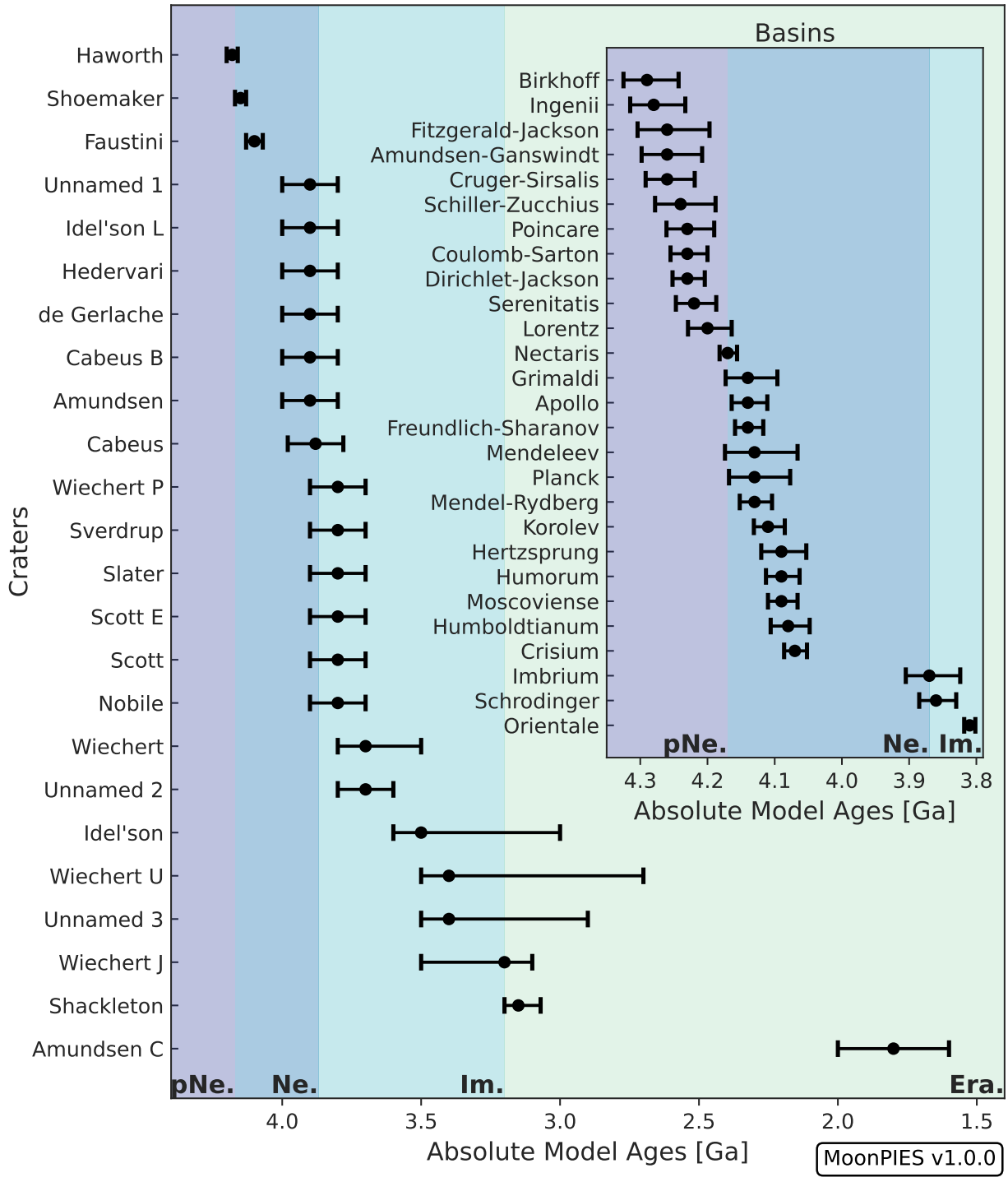

Figure 4.2: Absolute model ages of craters and basins (inset) incorporated within the MoonPIES model. The ages of polar craters were drawn from Deutsch et al. (2020) and Cannon et al. (2020). Lunar epochs were defined by the ages of the basins, drawn from (Orgel et al., 2018).

An exponent of -2.8 +/- 0.5 was proposed by Fassett et al. (2011) for basin-size events, but that is within the uncertainty of Equation 4.1. Two caveats of using Equation 4.1 to estimate ejecta thickness are: 1) proximal ejecta may be overestimated due to the raised crater rim (Kring, 2007; Sharpton, 2014), and 2) distal ejecta is heterogeneously distributed (e.g., as discontinuous rays; Gault et al. 1974) due to instabilities in the ejecta curtain (Melosh, 1989). Because none of the craters or basins in our study overlap each another, no cold traps lie on or within 1 crater radius of another crater. Furthermore, we restricted ejecta deposition to threshold distances at which most impacts produce continuous ejecta (Melosh, 1989), setting the threshold distances to be 4 crater radii for simple and complex craters, for consistency with Cannon et al. (2020), and 5 crater radii for basins (Liu et al., 2020; Xie et al., 2020).

4.3.3 Ballistic sedimentation

Ballistic sedimentation was first formally discussed by Oberbeck (1975) and describes the process by which ejecta from a primary crater follows a ballistic trajectory and impacts the surface at high velocity, mixing with local material to form breccias. A side effect of ballistic sedimentation is heating of the mixed ejecta unit. Because we have not drilled into ballistic sedimentation breccias on the Moon, we use Earth analogues to constrain the effects of ballistic sedimentation, specifically, the Bunte Breccia Unit within Ries crater in Germany (Oberbeck, 1975; Hörz et al., 1977, 1983).

Ballistic sedimentation only occurs when ejecta reach the surface with sufficient velocity to brecciate the target. In the case of Meteor Crater (D=1.25 km; see Kring 2007 for a review), a simple crater on Earth, continuous ejecta is distributed to distances of about two crater radii beyond the crater rim. Material deposited at the outer edge of that ejecta blanket hit the surface with a velocity of about 11 m/s, which caused some radially outward skating across the landscape, but no significant erosion and mixing with substrate materials or heating. Conversely, the larger Ries crater (D=24 km) has two distinct ejecta units. It contains a polymict breccia with fragments of solidified impact melt (known as suevite) that has components shocked to >50 GPa and depositional temperatures between 500 and 900°C (Kring 2005 and references therein). The underlying Bunte breccia unit represents the bulk of the ejecta and has components shocked to <10 GPa and was deposited with no significant increase in temperature. The Bunte Breccia is the ballistically emplaced unit at the Ries Crater (Hörz et al., 1977, 1983). The Bunte Breccia extended from near the crater rim to at least 36 km from the crater center, about 3 times the basin radius (see Kring 2005 for a review). We therefore expect the onset of ballistic sedimentation to occur at an ejecta kinetic energy intermediate to those at Meteor and Ries craters.

Since ballistic sedimentation is capable of introducing significant heating and mixing to target materials,

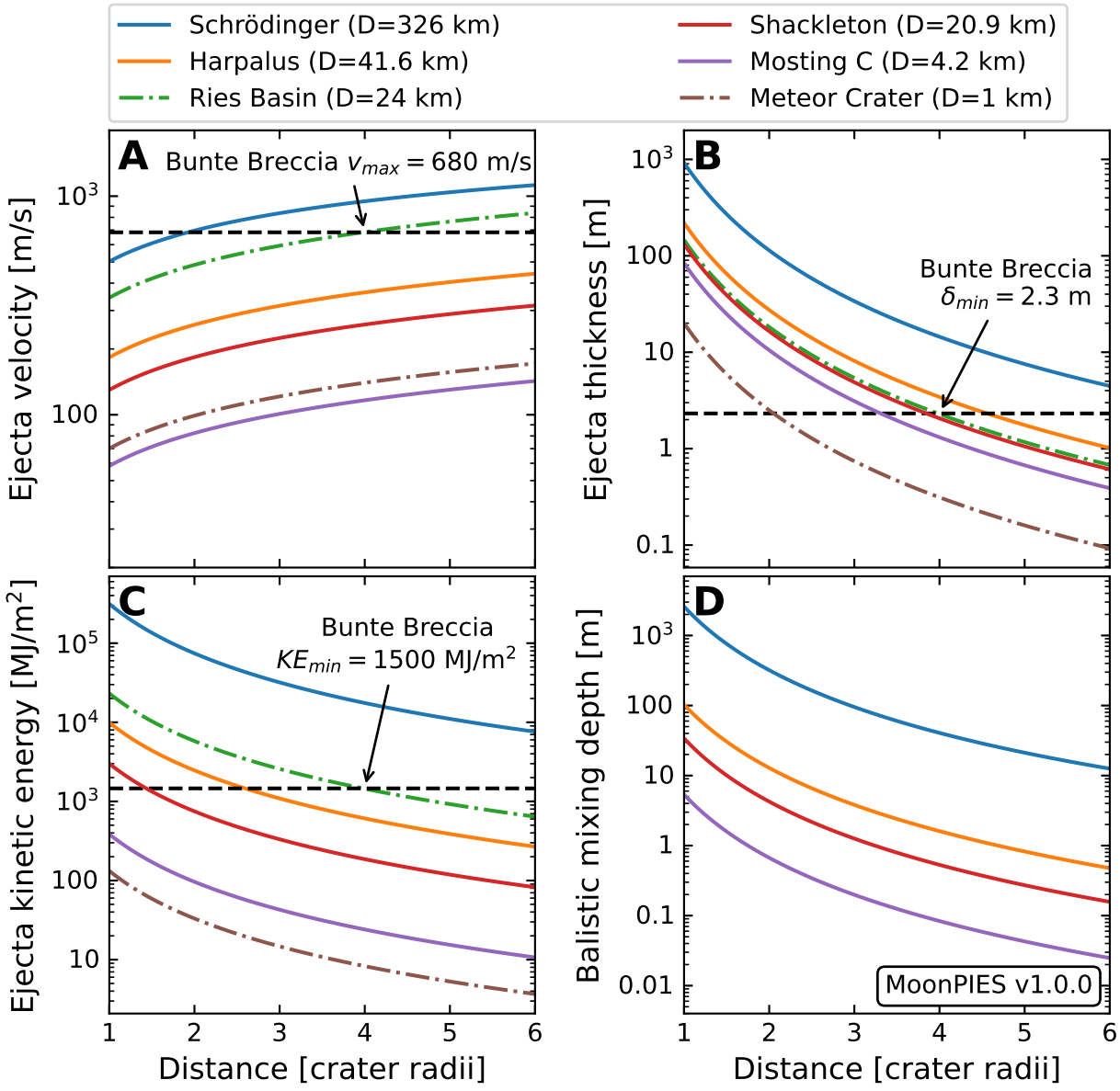

Figure 4.3: Modeled ejecta speed (A), thickness (B), kinetic energy (C), and ballistic mixing depth (D) with distance from primary crater for multiple craters ranging in size from simple to basin-sized impacts. Horizontal dashed lines are present on panels A through C, indicating relevant calculated values for the Bunte Breccia unit of the Ries basin impact structure.

we modeled it as an ice loss process as a function of ejecta kinetic energy, temperature, and depth of mixing.

Onset of ballistic sedimentation

To estimate a threshold kinetic energy for the onset of ballistic sedimentation, we computed the relevant ejecta energy of the Bunte Breccia deposits at the Ries impact structure (Kring, 2005). We computed ejecta mass per unit area as the product of ejecta density and thickness, assuming an ejecta density of $\rho = 2700$ kg/m^3 for Malmian limestone (Bohnsack et al., 2020) and calculating thickness using Equation 4.1 (R_{Ries}=12 km). Ejecta velocity at impact was computed using the ballistic formula for a spherical body (Vickery, 1986), derived from the half-angular distance of travel, $\phi = r/2R_p$, which is related to velocity (v) and the ejection angle (θ) by:

$$tan\phi = \frac{v^2 sin\theta cos\theta}{gR_p - v^2 cos^2\theta} \tag{4.2}$$

where g is gravitational acceleration and R_p is planet radius. Solving for velocity gives:

$$v = \sqrt{\frac{gR_p tan\phi}{sin\theta cos\theta + cos^2\theta tan\phi}} \tag{4.3}$$

Ballistic kinetic energy is then given by KE=mv^2 and is a function of r, R_p, and θ. Using the 4 crater radii extent of our ejecta deposits and Equation 4.3 for the Earth ($g = 9.81$ m/s^2; $R_p = 6371$ km) and assuming the most likely ejecta angle of $\theta = 45^o$, we find that the minimum kinetic energy that produced ballistic sedimentation at the Ries impact structure was ∼1500 MJ/m^2 (Figure 4.3).

For comparison, we repeated the above calculation for the 1 km Meteor Crater where ballistic sedimentation has not been observed (see Kring 2007 for a review). The maximum ejecta kinetic energy was ∼10 MJ/m^2 at Meteor crater, indicating the onset of ballistic sedimentation is between 10–1500 MJ/m^2.

The lunar case for ballistic sedimentation as a function of crater size is made by Oberbeck (1975) who observed the onset of hummocky textures in the continuous ejecta of craters larger than 4 km in diameter. Repeating the kinetic energy calculation for the Moon assuming an anorthositic target ($\rho = 2700$ kg/m^3; $g = 1.624$ m/s^2; $R_p = 1737$ km), we found the kinetic energy for Meteor Crater was smaller than the 4 km lunar crater (Figure 4.3). If the hummocky textures observed by Oberbeck (1975) are indicative of ballistic sedimentation, we would expect the Meteor Crater impact to be energetic enough to produce these deposits. However, since the smallest known crater to produce ballistic sedimentation deposits is the Ries impact, we use it as our model threshold. The derived ∼1500 MJ/m^2 at 4 crater radii corresponds to lunar craters $D \geq$ 20 km, and therefore we model ballistic sedimentation for impacts larger than 20 km which encountered a cold trap within 4 crater radii.

Ballistic sedimentation depth

We modeled the depth of influence of ballistic sedimentation events using the local mixing model introduced by Oberbeck (1975) and updated by Petro & Pieters (2004). The local mixing ratio, μ, of local material to ejected material was modeled as a function of distance traveled, r in km (Oberbeck, 1975), with an adjustment for $\mu > 5$ (Petro & Pieters, 2006):

$$\mu = \begin{cases} 0.0183 r^{0.87} & \mu \leq 5 \\ \frac{0.0183}{2} r^{0.87} + 2.5 & \mu > 5 \end{cases} \tag{4.4}$$

We then defined the ballistic sedimentation depth (δ) as the product of ejecta thickness (Equation 4.1) and mixing ratio (Petro & Pieters, 2004):

$$\delta = t \times \mu \tag{4.5}$$

The mixing ratio can also be expressed as the fraction of ejecta relative to total (ejecta and local) material as:

$$f_{ejecta} = \frac{1}{1+\mu} \tag{4.6}$$

We parameterize ice loss to ballistic sedimentation as a function of f_{ejecta} and the temperature of the incoming ejecta.

Fraction of ice volatilized

We used a 1D heat flow model to derive the fraction of local material volatilized (heated beyond a constant ice stability temperature), given the amount of ejecta delivered (f_{ejecta}) and the initial ejecta and target temperatures.

The 1D heat flow model assumes vigorous mixing and rapid equilibration, such that the ejecta and local material primarily exchange heat through conduction rather than radiation (Carslaw & Jaeger, 1959; Onorato et al., 1978). We then solve the 1D heat flow equation (Carslaw & Jaeger, 1959) and track the maximum temperatures encountered during equilibration. We summarize the model in Equations 4.7 – 4.8:

$$K = \frac{\kappa(T)}{\rho C_p(T)} \tag{4.7}$$

$$T_{i,n+1} = \frac{K\Delta t}{(\Delta\chi)^2} T_{i-1,n} + \frac{K\Delta t}{(\Delta\chi)^2} T_{i+1,n} - (2 \times \frac{K\Delta t}{(\Delta\chi)^2} T_{i,n}), \tag{4.8}$$

where K is the thermal diffusivity, $\kappa(T)$ is thermal conductivity, $\rho = 1800$ kg m^{-3} is regolith density, $C_p(T)$ is the heat capacity, $\Delta t = 1$ ms is the time step, $\Delta\chi = 10$ μm is the spatial scale, and i, n are the spatial and time steps, respectively, with regolith properties drawn from (Hayne et al., 2017).

To compute the fraction of water ice volatilized ("melt fraction" hereafter), we chose an ice stability temperature of 110 K (Hayne et al., 2015; Fisher et al., 2017). We initialized the 100 pixel 1D model to a PSR temperature of 45 K (typical surface temperatures of lunar polar cold traps; Paige et al. 2010a), and varied the f_{ejecta} and temperature of ejecta pixels from 0–100% and 110–500 K, respectively. We ran the thermal model until equilibration (i.e., all elements within 1 K of each other), or until all elements exceeded 110 K (melt fraction = 1). We defined the melt fraction as the fraction of local elements that exceeded 110 K in any time step. We randomized the initial ejecta positions and ran the model 50 times for each f_{ejecta} and ejecta temperature combination, reporting the mean and standard deviation melt fractions of all runs (Figure 4.4; Data Sets S3-S4, Appendix C).

Ice lost due to ballistic sedimentation

To predict ice loss in a particular ballistic sedimentation event, we estimated the ejecta and PSR temperatures at the time of deposition. Hydrocode simulations by Fernandes & Artemieva (2012) indicated that ejecta temperatures increase with distance from a basin impact due to shock heating, but primarily beyond the 4–5 radius distances modeled here. Proximal ejecta temperatures were much more sensitive to the choice of subsurface thermal profile from about 260 K in the "present-cold-Moon" scenario to 420 K for the "ancient-hot-Moon" (Artemieva & Shuvalov, 2008). For a conservative treatment, we chose 260 K as the ejecta temperature basin impacts, but note that there is little change in our predicted melt fraction from 260–420 K (Figure 4.8). For smaller cratering events (non-basin impacts from polar crater), we chose an ejecta temperature of 140 K, a typical sub-surface polar regolith temperature (Vasavada et al., 1999; Feng & Siegler, 2021). For each ballistic sedimentation event, we then retrieved f_{ejecta} (Equation 4.6) and ejecta temperature (Figure 4.4) and computed the depth of influence, δ (Equation 4.5). We assumed that the derived melt fraction of ice was volatilized in each layer within δ of the surface. All volatilized ice is assumed to be lost from the stratigraphy column in the ballistic sedimentation event since redistribution and upwards migration of ice is outside the scope of this work. We discuss the implications of this simple treatment of ballistic sedimentation ice removal in §4.5.2. If multiple ballistic sedimentation events occurred in a single timestep, they were applied in δ order from smallest to largest. The ballistic sedimentation events in our model produced δ values ranging from meters to multiple kilometers depending on the size of primary impact and distance to a particular cold trap (Figure 4.3). Our first order approximation of ballistic sedimentation effects allows us to assess incoming ejecta as a removal process, however a method which more precisely

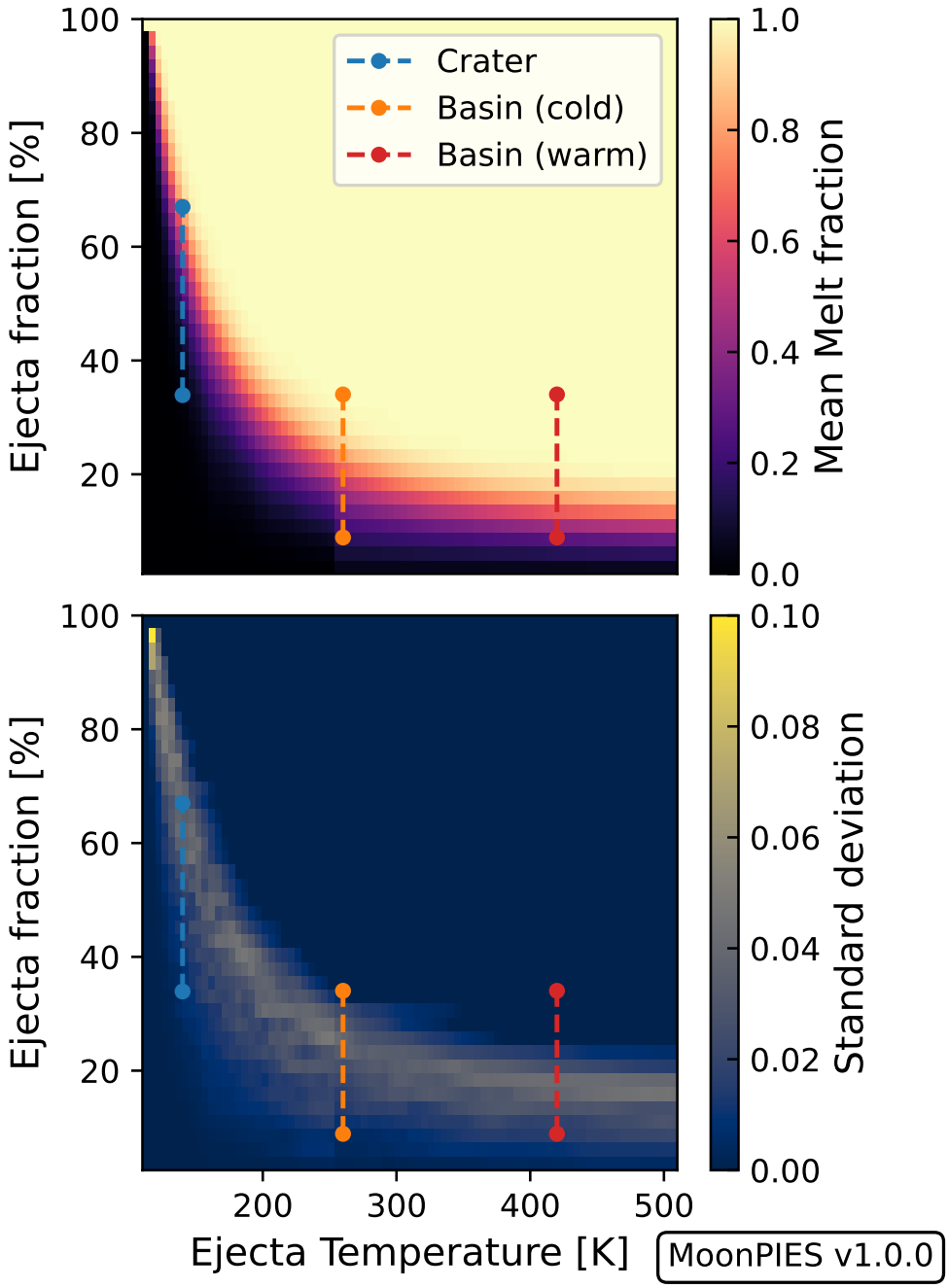

Figure 4.4: Ballistic sedimentation melt fraction as a function of initial ejecta fraction (f_{ejecta}) and ejecta temperature. Melt fraction is expressed as the mean (upper left) and standard deviation (upper right) cold trap material exceeding 110 K in model simulations, computed over 50 runs with random initial ejecta positions. High temperatures and ejecta fractions result in high melt fractions, as expected. Ranges of melt fractions are indicated for ballistic sedimentation events resulting from craters (blue) and basins (orange, present-cold-moon; red, warm-ancient-moon) modeled in this work.

mixes and redistributes ice may be warranted in future work.

4.3.4 Impact ice delivery

To model ice delivery to the the lunar poles by impacts, we first divide all possible impactors into 6 size regimes and two classes: hydrated asteroid and comet. Hydrated asteroids in Regimes B–E were modeled consistently with Cannon et al. (2020) as 24% hydrated C-types with 10% water content by mass, and adopting consistent fluxes, size-frequency distributions, and crater scaling laws, as summarized in Table 4.1 (Brown et al., 2002; Grün et al., 2011; Mazrouei et al., 2019; Neukum et al., 2001; Ong et al., 2010). Additionally, we introduce basin impactor (the new Regime F) and cometary impactor (across all regimes) contributions to polar ice for the first time.

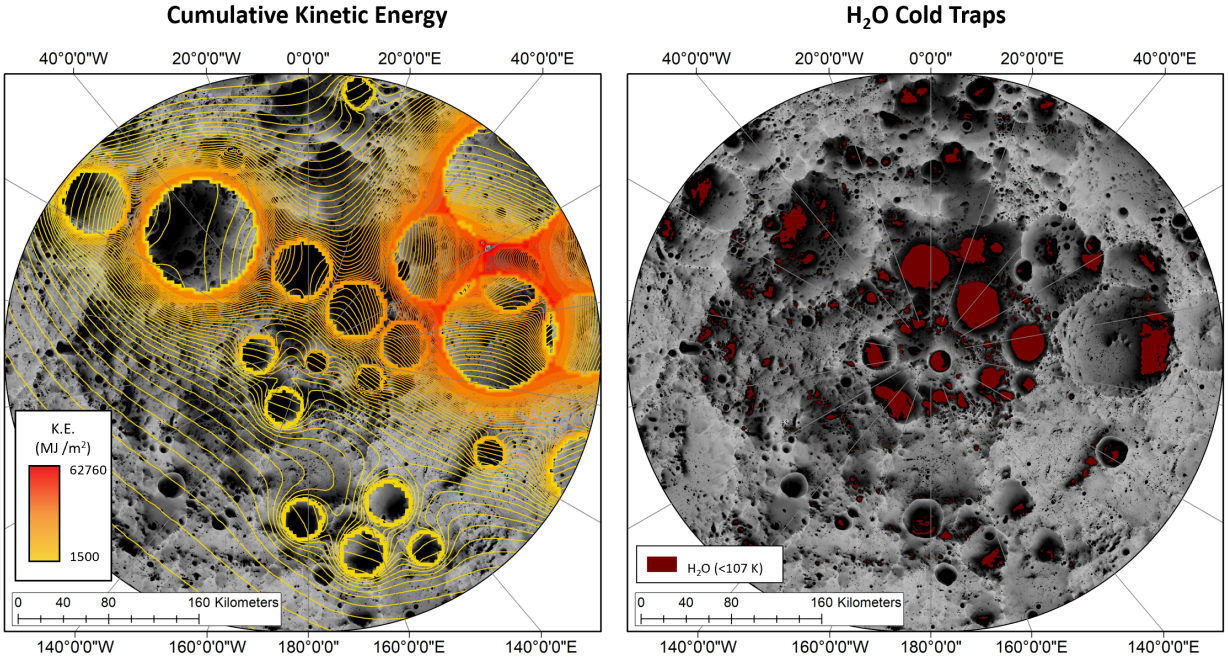

Figure 4.5: Cumulative Kinetic Energy (left) from each of the large age-dated craters, excluding basins. The kinetic energy contours are plotted over an average solar illumination map of the south pole (AVGVISIB_75S_120M_201608.LBL; Mazarico et al. 2011). Water ice cold trap extents (right; Landis et al. 2022).

Micrometeorites and comets

We modeled all micrometeorites (Regime A) as cometary based on dynamical models that suggest comets dominate the smallest impactors at 1 AU (Oberst et al., 2012; Suggs et al., 2014; Pokorný et al., 2019). For larger impacts, we assumed 5% are cometary, which is a conservative estimate within a typical range

of 5-17% (Joy et al., 2012; Liu et al., 2015). To predict the total cometary mass delivered, we used the same scaling laws of Regimes B–F (Table 4.1). We assigned each comet a random velocity from a bi-modal velocity distribution (Figure C.2) and assumed each comet is 50 wt% water (Whipple, 1950) with a density of 600 $kg\ m^{-3}$ (the density of Comet Shoemaker-Levy 9; Asphaug & Benz 1994).

Regime	Population	Impact Freq. Ref.	CSFD slope	Crater Diam (km)	Impactor Diam (km)	Crater Scaling Ref.	Model Treatment
A	Micro-meteorites	Grün et al. (2011)	N/A	N/A	10 nm – 1 mm	N/A	Averaged
B	Small Impactors	Brown et al. (2002)	-3.82	N/A	10 mm – 3 m	N/A	Averaged
C	Small simple craters	Neukum et al. (2001)	-3.82	0.1 km – 1.5 km	N/A	Prieur et al. (2017)	Averaged
D	Large simple craters	Neukum et al. (2001)	-1.8	1.5 km – 15 km	N/A	Collins et al. (2005)	Stochastic
E	Complex craters	Neukum et al. (2001)	-1.8	15 km – 300 km	N/A	Johnson et al. (2016)	Stochastic
F	Basins†	Orgel et al. (2018)	N/A	$\geq$ 300 km	N/A	Johnson et al. (2016)	Individual

†MoonPIES only

Table 4.1: Cratering Regimes. Regimes A-E are defined following (Cannon et al., 2020). Regime F, representing basin impactors, was added for this work.

Basins

Basins included in our model (Figure 4.2; Data Set S2, Appendix C) were designated as hydrated C-type, cometary, or neither at the same probability as other impactors. If a modeled basin impactor was icy, it delivered ice in the timestep nearest to its age, randomized within model age uncertainties for each run. Although absolute ages and age uncertainties are debated for several basins, we drew all basin ages from the same source, Orgel et al. (2018), noting that the sequence of basin ages is more important for generating an accurate stratigraphy than precise absolute ages. We scaled each basin main ring diameter to transient diameter using the scaling laws from Croft (1985) and then to impactor diameter following Johnson et al. (2016). Volatile content and retention rates were predicted consistently with other hydrated asteroids and comets in the model.

Volatile retention

The fraction of ice retained by the Moon in a hypervelocity impact is primarily a function of the impact velocity (Ong et al., 2010). We derived a simple power law fit to retention rates computed in impact simulations by Ong et al. (2010) ($1.66 \times 10^4 v^{-4.16}$, where v is velocity in m/s; Figure C.3). For consistency with Cannon et al. (2020), we retained the assumption that $<$ 10 km/s impacts result in 50% volatile

retention for asteroid impactors due to incomplete clay mineral heating (Svetsov & Shuvalov, 2015).

Ballistic hopping

At each timestep, global ice delivery was converted to a local cold trap ice mass by employing a ballistic hop efficiency. The ballistic hop efficiency is defined as the fraction of global ice that comes to rest in a particular cold trap via ballistic hop random walks. We took the fraction of total water in the ballistic hop simulations by Moores (2016) and normalized by cold trap area. For cold traps not modeled in Moores (2016), we made a conservative estimate recognizing that ballistic hop efficiency is related to latitude. For Slater, we took the average of the nearest latitude craters, Shoemaker, de Gerlache, and Sverdrup. For craters north of Faustini (87.2° S), we set the ballistic hop efficiency to that of Faustini, recognizing that if the latitude trend holds then this would underestimate the amount of ice transported to and therefore retained within these cold traps in the model (Figure C.1; Data Set S5, Appendix C).

4.3.5 Volcanic ice delivery

We modeled volcanic ice delivery via a transient atmosphere that deposits ice in polar cold traps (Aleinov et al., 2019). Volatiles are deposited at a rate predicted by transient atmosphere simulations by Wilcoski et al. (2021), who found 26% of erupted H_2O is able to be deposited in south polar cold traps when accounting for atmospheric escape and sublimation. This treatment of deposition ignores any effect of ballistic hopping as the deposited H_2O from a transient atmosphere can only persist on the poles and is very quickly sublimated away elsewhere on the surface (Wilcoski et al., 2021). We used model estimates of Needham & Kring (2017) for total H_2O outgassed from mare volcanic provinces over time. We converted volatile H_2O to ice deposited in the style of Cannon et al. (2020). Although Head et al. (2020) presented smaller estimates of outgassed volatile mass, our model is insensitive to this choice as neither deposits more ice than is removed by impact gardening in a given timestep, as seen in Figure 4.6.

4.3.6 Solar wind H^+ deposition

We included a treatment of solar wind H^+ as a possible source of water in polar cold traps (Arnold, 1979). We used solar wind-derived H_2O mass flux of 2 g/s H_2O (Housley et al., 1973; Benna et al., 2019). We note this may be an overestimate since Lucey et al. (2020) predicted about 1/1000 of the 30 g/s H^+ suggested by Hurley et al. (2017) would be converted to H_2O. Additionally, historical solar wind H^+ flux may have been lower when the sun was fainter (Bahcall et al., 2001). However, less than 1 cm of ice is expected per model timestep given the 2 g/s H_2O rate, which is less than is removed by impact gardening each timestep, making

our model insensitive to a more precise treatment of solar wind ice delivery, illustrated in Figure 4.6.

4.3.7 Ice loss by impact gardening

We model the loss of ice from polar cold traps as a function of the lunar impact gardening rate, similarly to Cannon et al. (2020). Recent work by Costello et al. (2021) scaled the impact gardening depth by the historical impact gardening flux, predicting that polar cold traps may be heavily disturbed to 10s of meters depth, deeper than previously proposed (Costello et al., 2018, 2020). In timesteps where we expect the lunar impact flux to be approximately constant (3 Ga to present; Neukum et al. 2001), we adopted a present-day reworking rate of 10 cm per 10 Myr (Costello et al., 2020), consistent with Cannon et al. (2020). At earlier timesteps, we scale this value by the historical lunar impact flux (Neukum et al., 2001). Figure 6 of Costello et al. (2021) shows an excess reworking depth prior to 3 Ga of approximately 1% of the relative early impact flux (Neukum et al., 2001). Therefore we scale the present-day 10 cm depth accordingly, resulting in a gardening rate of approximately 3 m per 10 Myr in the first model timestep (4.25 Ga). This deeper early gardening quickly decays with the impact flux to a steady value of 10 cm in each timestep from 3 Ga to present.

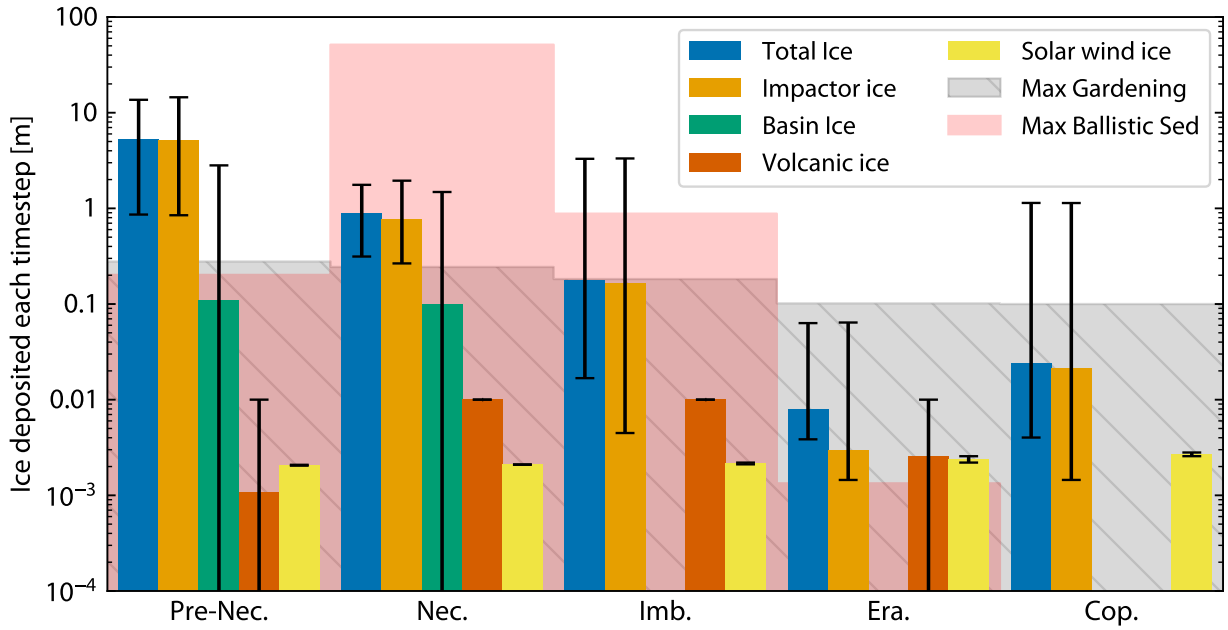

Figure 4.6: Average ice deposited in each timestep across lunar geologic eras spanned by a MoonPIES model run (log scale). The bars represent the total ice thickness (blue) as well as ice originating from non-basin impactors (orange), basin impactors (green), volcanic (red), and solar wind (yellow). Whiskers denote the maximum and minimum ice delivered in a particular timestep. Shaded regions represent the maximum ballistic sedimentation depth and impact gardening possible in each era, though on average less than this is removed because ballistic sedimentation is sporadic and ejecta layers will preserve ice underlying ice.

At each timestep, we removed all ice present in the predicted gardening depth. Although some ice may not be completely lost from the Moon following a particular gardening event, the gardening depths we chose predict total homogenization of the regolith (see Costello et al. 2021 for a detailed discussion). Therefore, most material to these depths have been disrupted (excavated and re-buried) numerous times. Because our 10 Myr model timesteps are much longer than the expected ∼1000 yr residency time of ice in polar cold traps (Farrell et al., 2019), homogenization of the gardened layer would allow ample opportunity for all ice in this layer to be lost. While not all ice escaping a cold trap is lost from the Moon entirely, there is a much greater chance of it coming to rest in cold traps not large enough to retain a stratigraphic sequence (e.g., micro cold traps; Hayne et al. 2021) and therefore are outside the scope of this work.

4.3.8 Randomness and reproducibility

To simulate the delivery of ice and ejecta to target cold traps, MoonPIES uses Monte Carlo methods to vary the timing and abundance of impacts through lunar geologic history. Consistent with the previous model by Cannon et al. (2020), ice delivery was driven by impactor size and impactors forming craters smaller than 1.5 km diameter were treated as bulk populations, with fluxes drawn from the literature (see Table 4.1). However, larger impactors were modeled individually with compositions (hydrated asteroid, unhydrated asteroid, or comet) and speeds each randomly drawn, affecting the ice delivered and retained in a given timestep (see §4.3.4). Asteroid speeds were drawn from a Gaussian distribution (μ=20km/s, σ=6km/s). Comet speeds were drawn from a bimodal distribution of two Gaussians to simulate the Jupiter family and long period comet populations (μ_{JFC}=20km/s, σ_{JFC}=5km/s; μ_{LPC}=54km/s, σ_{LPC}=5km/s) (Chyba, 1991; Jeffers et al., 2001; Ong et al., 2010). We assume that Jupiter family comets are 7 times as likely as long period comets, though the precise ratio and its evolution over lunar geologic time are not well constrained (Carrillo-Sánchez et al., 2016; Pokorný et al., 2019).

To model individual crater and basin events that deliver ejecta to cold traps, we randomly drew ages from the published crater count model ages (Figure 4.2). Ages were drawn from a truncated Gaussian centered on the absolute model age with standard deviation being half of the model age uncertainty (or the average of the upper and lower bounds, if asymmetric). The minimum and maximum ages are fixed at the upper and lower age uncertainty. Ice delivery was not modeled for individual south polar craters since their contributions are already included in the complex crater population. However, basins are assigned a probability of being asteroidal or cometary and a random impact speed to determine ice delivery in a consistent manner with other impactors. Ejecta deposition and basin ice delivery then occurs during the nearest timestep in the model to the assigned ages for these individual events.

For reproducibility, MoonPIES generates a configuration file specifying all parameters used to run the model as well as the random seed, allowing a given model run to be reproducible. Monte Carlo results presented here were run on MoonPIES v1.0.0 with random seeds 1-10000 (see Tai Udovicic et al. 2022a for full documentation).

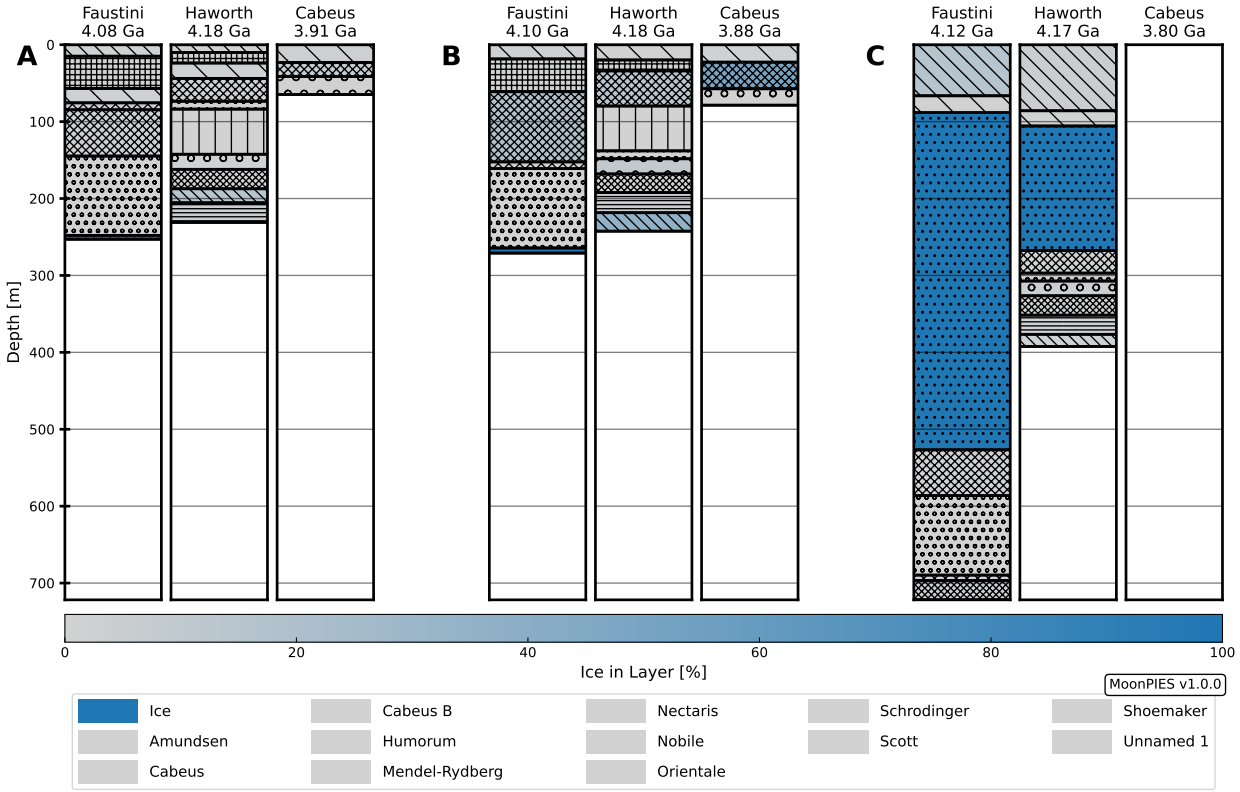

Figure 4.7: A comparison of Fautini, Haworth and Cabeus over 3 different Monte Carlo model runs (all including ballistic sedimentation effects). We note that the cold trap ages and stratigraphic sequence of a particular run differs due to random variation in ejecta ages and ice delivery. Runs A and B show typical columns for all three cold traps. In run C, the large ice layer in Faustini and Haworth is the result of a basin-scale cometary impact, while the absence of layering in Cabeus indicates that it formed later than all possible ejecta sources.

4.4 Results

The ice layering trends predicted by the MoonPIES model were broadly consistent with Cannon et al. (2020) when ballistic sedimentation was excluded from the model (e.g., the oldest cold traps often retained "gigaton" ice deposits). However, when accounting for ballistic sedimentation, such gigaton ice deposits were disrupted and the quantity of ice retained was reduced. We also found a location dependence of ice retention, with cold traps nearest to the poles retaining less ice in general when compared to cold traps at lower latitudes.

We ran the model 10,000 times to generate a distribution of ice retention in each cold trap, with the results of the Monte Carlo approach shown in Figures 4.7 and 4.9. Figure 4.7 compares the stratigraphic columns generated for Faustini, Haworth, and Cabeus craters over three different Monte Carlo model runs, while Figure 4.9 shows the range of possible total ice thicknesses across all 10,000 model runs for the 10 cold traps in our sample (Data Set S6, Appendix C).

4.4.1 Effects of ballistic sedimentation

Ballistic sedimentation reduced the amount of ice retained within most cold traps modeled in this study. Figure 4.8 depicts a single run with and without the effects of ballistic sedimentation, while Figure 4.9 depicts total ice thickness retained for 10 cold traps across 10,000 model runs with and without the effects of ballistic sedimentation. Cold traps were grouped by similar age and sorted by latitude within each group.

When ballistic sedimentation is considered, ejecta from nearby craters and impact basins effectively removed pre-existing ice within cold traps, resulting in less preserved average ice thickness across all cold traps. Ballistic sedimentation did not remove ice entirely, but rather reduced the thickness of ice deposits at and near the surface at the time of ejecta implantation. Although impacts that form basins and complex craters both have the potential to remove ice due to ballistic sedimentation, basin-sized impacts tended to be more effective at melting ice through ballistic sedimentation than complex polar craters. Complex polar craters tended to produce ejecta lacking sufficient kinetic energies at the distances required to reach nearby polar cold traps, effectively caused a net preservation effect rather than a net ice removal effect. The influence of ballistic sedimentation was most notable for the oldest cold traps in our sample, Haworth, Shoemaker, and Faustini. The oldest cold traps retained large ice deposits in nearly all runs without ballistic sedimentation. After ballistic sedimentation effects were included, ice retention was reduced and more variable, with cold traps retaining about a tenth of former median total ice thicknesses.

Similarly, Nectarian and Imbrian cold traps saw overall declines in ice retention when including the effects of ballistic sedimentation, though not as dramatically as observed in the Pre-Nectarian cold traps. Eratosthenian cold traps formed after the majority of ice was delivered and most large ballistic sedimentation events occurred and therefore retain little ice regardless of ballistic sedimentation.

4.4.2 Gigaton ice deposits

The term "gigaton deposit" has previously been used to refer to single layer ice deposits that would exceed 10^9 metric tons of ice if they filled a cold trap with a surface area of at least 100 km^2 (Cannon et al., 2020). Assuming a density of ice of $\sim$1000 kg/m^3, such deposits must be larger than 10 m thick. Pristine

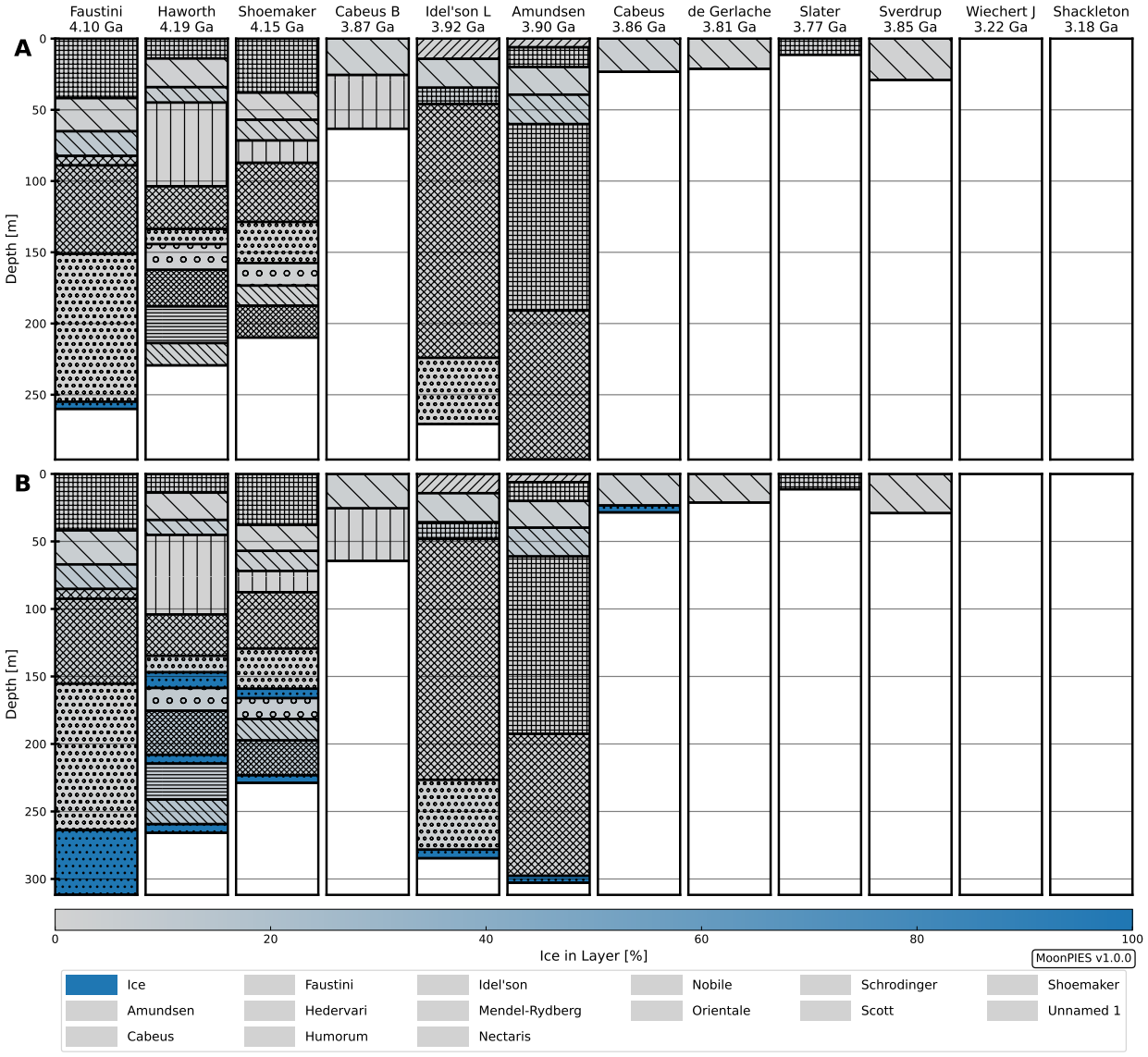

Figure 4.8: Model stratigraphy columns for the same model run with A) ballistic sedimentation and B) no ballistic sedimentation. When ballistic sedimentation was accounted for, large pure ice layers were lost from the base of the oldest cold traps (Faustini, Haworth and Shoemaker). Shallower layers retain a similar ice % in both cases. Although this is a representative outcome, it should be noted that the absolute quantity of ice and stratigraphic sequence changes from run to run (Figures 4.7-4.9).

single-layer deposits exceeding 10 m were rare in most cold traps and absent from others except when early large ice delivery events occurred in a particular run (Figure 4.8 - 4.7). We investigated the likelihood of retaining layers of a given thickness at depth over the 10,000 model runs (Figure 4.10). When excluding effects of ballistic sedimentation, gigaton layers (>10 m) emerged at depths of about 100 m, consistent with the previous model by Cannon et al. (2020). By contrast, when ballistic sedimentation was implemented, layers rarely exceeded 10 m and were most commonly < 1 m thick (Figure 4.10).

We also assessed the total ice retention by each cold trap at all depths (Figure 4.9). Without ballistic sedimentation, we found that the median total ice exceeded 10 m "gigaton" thickness for all Nectarian and older craters. However, when we accounted for ballistic sedimentation, all craters declined in total ice retention, with medians near or below 10 m. For Shoemaker, Idel'son L and Amundsen, this decline marked a shift from >75% of runs producing gigaton levels of ice to <25% exceeding the 10 m threshold. However, other Nectarian and older cold traps retained 10 m of ice in about 50% of runs. The youngest cold traps retained the least ice: Imbrian cold traps Slater and Sverdrup rarely exceeded 5 m, while Eratosthenian cold traps Wiechert J and Shackleton exceeded 1 m in only a handful of runs. In summary, while single layer gigaton deposits were rare, volumetric gigaton deposits occurred for most older cold traps in about 50% of runs.

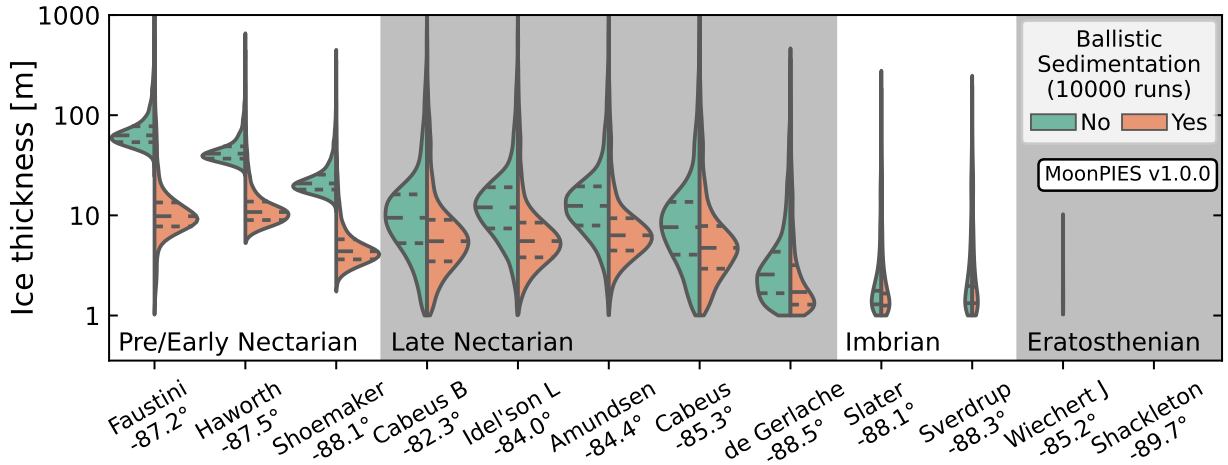

Figure 4.9: Total ice thickness retained across 10,000 runs for each cold trap grouped by geologic era and sorted by latitude. The width of each violin is scaled by the total number of runs retaining at least 1 m of ice. Median and quartiles are indicated as dashed lines. Without ballistic sedimentation, total ice thickness is greater, particularly for Pre-Nectarian and Nectarian cold traps. The difference in ice retention is smaller for Imbrian cold traps where few basins and local impacts disturb ice. About 1000 runs retained > 1 m for Wiechert J and only 3 runs retained > 1 m of ice in Shackleton.

4.4.3 Gardened layer

The gardened layer (referred to as gardened mantle deposits in Cannon et al. (2020)) we observed near the surface of most stratigraphy columns ranged in size depending on cold trap location and age. We defined the gardened layer as any portion of the column influenced by ballistic sedimentation or impact gardening and containing less than the 100 m "gigaton" ice thickness threshold defined above. For any given cold trap, the total thickness of the gardened regolith zone varied significantly across Monte Carlo runs. Figure 4.9 demonstrates that the distribution of total ice thickness for 10,000 model runs varies from 1 to 100 m for Pre-Nectarian and Nectarian cold traps, while younger cold traps tend to retain between 1 to 10 m.

We also observed a slight trend with latitude, finding that median total ice in the gardened layer declines towards the South Pole. In particular, Faustini, Cabeus B and Cabeus retained the thickest gardened layers with median total ice of ∼20 m. The smallest gardened layers occurred in the youngest and most poleward cold traps, namely Shoemaker, de Gerlache, Slater, Sverdrup, Wiechert J and Shackleton, each retaining <10 m median ice thickness. Wiechert J and Shackleton were the only cold traps which retained <1 m of total ice in the majority of runs and exceeded this threshold in only 10% and 1% of runs, respectively.

For comparison, we contrasted our results with 10,000 model runs which did not account for ballistic sedimentation (Figure 4.9). As expected, the total amount of ice retained in each cold trap was greater when ballistic sedimentation was excluded. In addition, thick, pristine ice layers were disrupted by ballistic sedimentation, causing the gardened regolith to be much more extensive in this work relative to the previous model by Cannon et al. (2020).

The distributions of total ice thickness for some of the Nectarian cold traps are bimodal in model runs without ballistic sedimentation (Figure 4.9), with one concentration of model runs retaining ∼100 m of ice and another concentration retaining ∼10 m of ice. This bimodal distribution is due to the precise timing and sequencing of the Nectarian basin ice delivery events that overlap in formation ages. The craters with bimodal ice thickness distributions form around the same time as several significant basin formation and ice delivery events, whereas the craters with simple ice thickness distributions have basin formation and ice delivery events exclusively outside of their age distributions. The bimodal thickness distributions are therefore attributed to the precise sequencing of basin ejecta delivery, ballistic sedimentation, and ice delivery around the time of cold trap formation. Therefore, cold trap age and the ages of nearby craters and basins can distinguish a "gigaton" ice deposit from a thin gardened layer ice deposit for Nectarian cold traps.

In addition to total ice, we also illustrate the possible distributions of ice with depth for Faustini, Haworth, Amundsen, Cabeus, de Gerlache, and Slater craters in Figure 4.10 using a kernel density estimation (KDE)

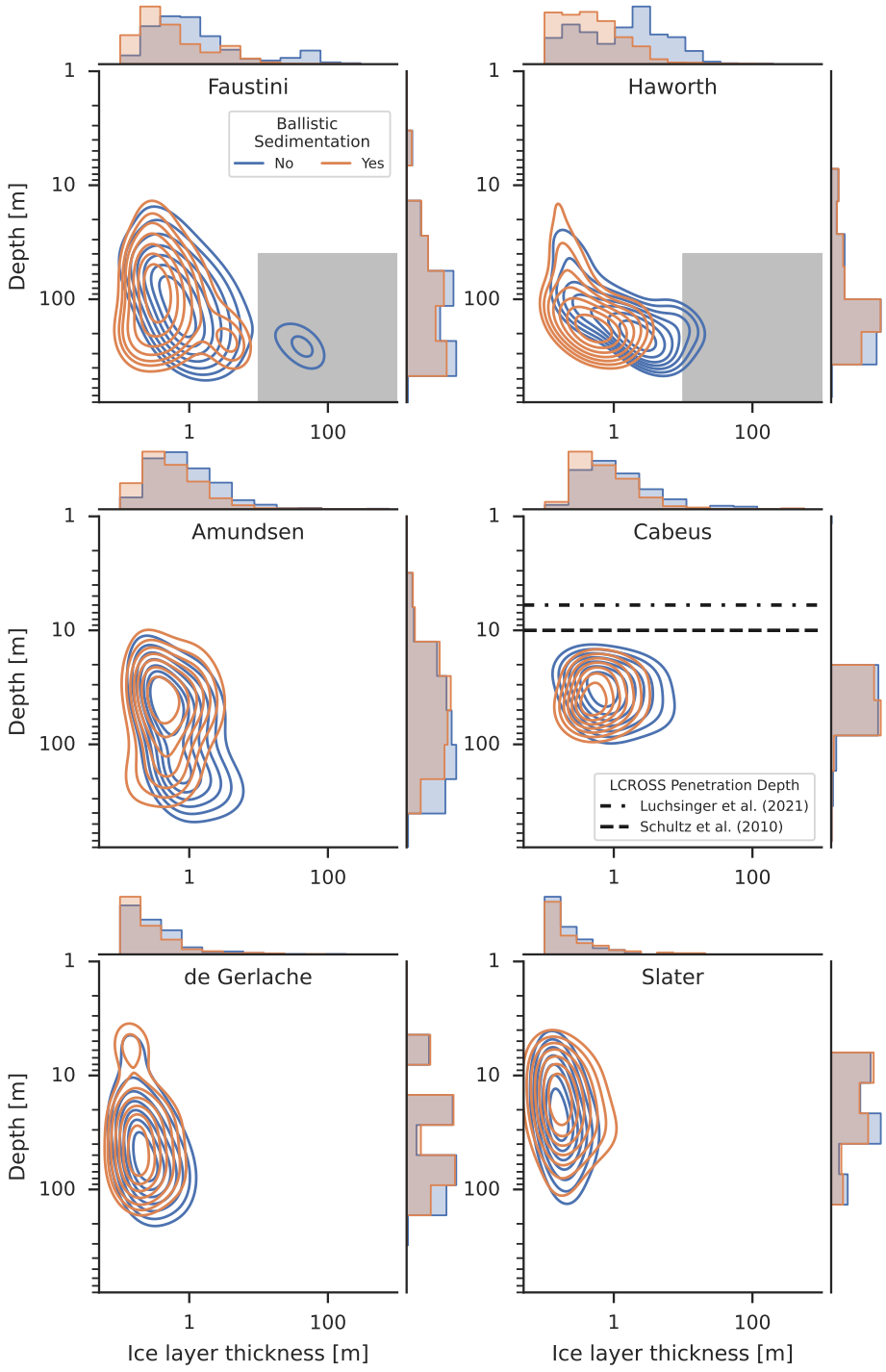

Figure 4.10: Thickness of ice layers with depth for 10,000 model runs, represented as kernel density estimation (KDE) contour plots for Faustini, Haworth, Amundsen, Cabeus, de Gerlache, and Slater craters. Blue contours represent model runs without ballistic sedimentation, and brown contours represent model runs with ballistic sedimentation and contour centers represent the most likely thicknesses with depth. Shaded regions indicate "gigaton" zones, where layer thickness exceeds 10 m. For Cabeus, horizontal lines denote LCROSS maximum excavation depth (Schultz et al., 2010; Luchsinger et al., 2021).

contour plot of ice thickness vs. depth. The contours represent the number of times an ice layer of the corresponding thickness was present at the corresponding depth over 10,000 model runs, both with (blue) and without (brown) ballistic sedimentation effects. Gray boxes in the top two plots indicate the gigaton deposit zone. In this figure, we have indicated two possible excavation depths from the LCROSS impact for Cabeus (Schultz et al., 2010; Luchsinger et al., 2021).

For Faustini, Haworth, and Amundsen, the three oldest cold traps, the blue ballistic sedimentation contours are shifted to the left relative to the brown contours, which represent model runs with no ballistic sedimentation. The shift in the blue contours represents ice deposits that have been disrupted and reduced in thickness. Individual ice layers in the gigaton deposit zone, indicated by gray boxes, only occur in some model runs without ballistic sedimentation, and only for Faustini and Haworth craters. The contour lines for Cabeus, de Gerlache, and Slater are less affected by ballistic sedimentation. Faustini and de Gerlache both contain ice deposits within the uppermost 6 m of regolith in some model runs, potentially making these craters high priority for missions with depth sensitivity greater than 1 m. However, the depth and temporal resolution of the MoonPIES model limits its ability to predict surface expression of ice.

In Figure 4.11, we present a boxplot of ice concentration for all cold traps within the uppermost 6 m. The boxes denote the first and third quartiles, while the whiskers denote the 99th percentile, and the individual points represent outliers above the 99th percentile. At least 75% of model runs predicted no ice retention in the uppermost 6 m. We calculated how often the cold traps retained 0.3 m of ice in the upper 6 m, comparable to the ∼5% concentration measured during the LCROSS impact into Cabeus crater (Colaprete et al., 2010). None of the cold traps met or exceeded this threshold in the majority of model runs (Faustini and de Gerlache craters were the most likely at 22% and 8% of model runs, respectively). Most cold traps, including Cabeus crater, only retained 0.3 m of ice in a maximum of 1% of model runs. Therefore, the MoonPIES model may underpredict ice near the surface, which we discuss in §4.5.2.

4.5 Discussion

4.5.1 Gigaton ice deposit distribution

Previous work by Cannon et al. (2020) described deposits containing up to hundreds of meters of ice as "gigaton" deposits. When accounting for ballistic sedimentation in the MoonPIES model, we found that gigaton deposits of ice are rarely large coherent sheets. Instead, modeled stratigraphy columns are more likely to contain thinner layers that have been disrupted and reduced in size (Figure 4.10). In rare cases, the total ice thickness retained in our model reached 100 m, typically when large volumes of ice were delivered by large icy impactors. Ice retention also depended on the precise sequencing of cold trap formation and

ballistic sedimentation events.

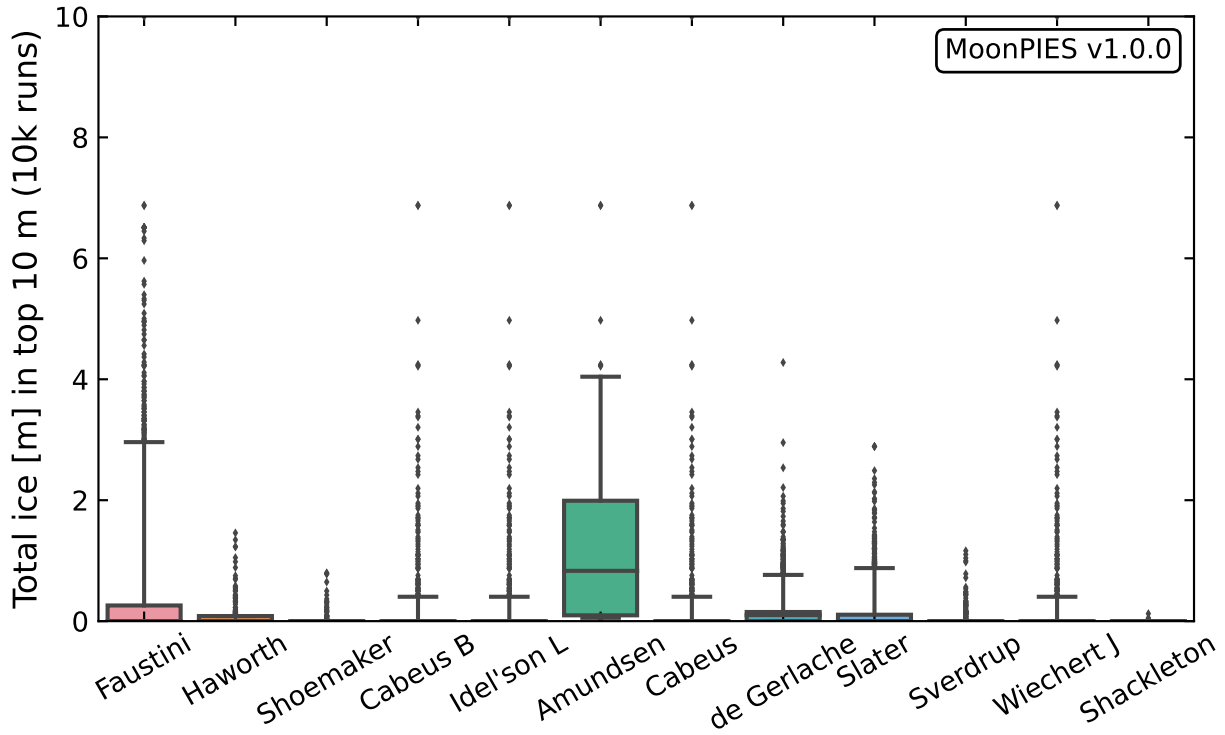

Figure 4.11: Boxplot of ice retained in each modeled cold trap to a depth of 6 m (the LCROSS impact is thought to have excavated 6–10 m into Cabeus crater; Schultz et al. 2010; Luchsinger et al. 2021). Boxes denote the first and third quartiles and whiskers denote the 99th percentile. Points denote outliers above the 99th percentile value. At least 75% of runs predicted 0 m ice retention in the upper 6 m for all cold traps except Faustini and de Gerlache.

4.5.2 Ice disruption in gardened layers

Our model predicted that most ice layers stored within polar cold traps would have been disrupted by either impact gardening and/or ballistic sedimentation. We found that cold traps farther from the pole were more likely to retain thicker ice deposits, due to the MoonPIES model treatment of ballistic transport to the south polar region, wherein the majority of ballistically transported ice comes to rest in the first cold trap encountered (Moores, 2016). We note that our model only tracks deposition of ice by primary delivery processes and does not track the redeposition of ice that is lost from a particular cold trap, nor the interchange of ice between our target cold traps and seasonal or micro cold traps (Kloos et al., 2019; Hayne et al., 2021). Therefore, the gardened layers are conservative estimates of total ice storage. Secondary ice mobility processes such as redeposition and thermal pumping (Schorghofer & Aharonson, 2014; Schorghofer & Williams, 2020) could result in larger ice deposits than those modeled here, particularly in the case of

near-surface expression of ice deposits.

In the MoonPIES model, the expression of near-surface ice in a gardened regolith was primarily determined by the thickness of the final ejecta deposition event(s) or large quantities of ice delivered by impacts near the end of a model run. The lack of surface ice observed follows from our treatment of impact gardening, which typically removed more ice than the average deposition from all sources in any given timestep post-Nectarian (Figure 4.6). Our Monte Carlo treatment is consistent with the analytical results of Costello et al. (2021) who predicted that impact gardening would have removed all ice to a depth of 1 m since 1 Ga or 3m since 3 Ga. The surface expressions of ice are almost entirely unconstrained by the MoonPIES model, due to the sensitivity of surface expression to short term events within the most recent timesteps, as seen in Figure 4.11. MoonPIES also does not consider redeposition of lost ice into neighboring cold traps, thermal pumping, or other ice modification processes that may affect surface expression of ice, again contributing to the inability of the MoonPIES model to predict surface expression.

The particular scenario where ice was retained at the surface in our model was when large icy impactors delivered ice very recently, which could be linked to the large polar ice deposits at Mercury (Moses et al., 1999). However, such a scenario is unlikely the case at the Moon due to the absence of massive ice deposits at the surface or in the shallow subsurface (Li et al., 2018; Campbell et al., 2006; Neish et al., 2011). Instead, surface ice is more likely the result of present-day production of ice by the solar wind on timescales shorter than 10 Myr (Benna et al., 2019) or surface-subsurface exchange (e.g., through thermal pumping; Schorghofer & Aharonson 2014) not modeled here. Our model is therefore most relevant for subsurface ice exploration at depths of 3-10 m and greater.

4.5.3 The nature of buried ice below polar cold traps

Our model aggregates ice delivery to the south pole from solar wind, volcanic outgassing, and impact delivery. Using published rates of solar wind deposition (Housley et al., 1973; Benna et al., 2019) and volcanic outgassing (Needham & Kring, 2017), the ice deposition rate in all cold traps is many orders of magnitude smaller than the impact gardening rate at any point in time (Figure 4.6). Therefore, our model predicts that large buried ice deposits would be primarily sourced from impacts.

Impactors in this work included contributions from both asteroids and comets, an update from previous work considering only asteroids (Cannon et al., 2020). We assumed a constant comet proportion of 5% as a conservative estimate of typically reported values (5%–17%; Joy et al. 2012; Liu et al. 2015). At this proportion, comet ice contributions were comparable to asteroid ice due to the greater ice concentration, despite lower retention on average due to greater impact speeds (Ong et al., 2010). We also allowed basin

impactors to be icy at the same rates as other impactors. On average, basins contributed about 2 m of ice per basin-era timestep (1 m each from asteroidal and cometary basins; Figure C.4). However, as stochastic events, many runs delivered no basin ice, while rare large basin impactors in other runs exceeded all other ice sources. In addition, basin ice delivery events produced deep early ice layers which were more likely to be retained over geologic time. Basin ice abundance and retention depended heavily on the sequence of basin events, their impactor composition and randomly assigned speed. Improved constraints on the fraction of cometary and asteroidal impactors over lunar history, as well as the ages and composition of basin impactors, would dramatically improve our understanding of deep water ice deposits at the lunar poles.

4.5.4 Implications for lunar ice exploration

The MoonPIES model explores ice delivery, retention, and removal over geologic time scales. However, human exploration occurs on human time scales, during which short term ice deposition and removal can occur. These short term ice behaviors can lead to surface expressions of ice that are not captured by our model. Additionally, the true ice distribution is the result of a long stochastic history that we can only partially constrain, as illustrated by the variance in possible outcomes over 10,000 model runs (Figure 4.9). In particular, the bimodal distributions caused by uncertainty in the precise sequencing in crater and basin formation events indicate that precise sequencing of crater and basin ages is critical to the ability to precisely model and predict the thickness of ancient ice deposits.

Our model predicts that the disruption of ice by impact gardening and ballistic sedimentation would cause large coherent ice deposits at depth to be unlikely. We found that the gigaton deposits observed in Cannon et al. (2020) would be rare and, if present, likely to be disturbed and present only in incoherent layers. Therefore, well-defined contacts between lithic and icy layers are unlikely to be detected with radar, consistent with inconclusive space-borne radar studies (Spudis et al., 1998; Campbell et al., 2006; Patterson et al., 2017). If the LCROSS impactor excavated 10 m of material, it could have sampled a region that MoonPIES predicts could be populated by ice; however, if it only excavated 6 m of material, it would have sampled only the surface expression ice. Deposits beyond 6 m may have formed a layer of harder material that prevented excavation, as suggested by Luchsinger et al. (2021). Additionally, ground-penetrating radar (GPR) may present an opportunity to probe for ice layers beneath cold traps (Kring, 2007, 2020) with deeper penetration depths than orbital radar. GPR may also allow thinner ice layers to be detected by using higher frequencies than orbital radar. Although our predictions indicate that fully coherent thick ice layers are rare, changes in dielectric properties or partially preserved layers of ice may be observable with ground penetrating radar. While Faustini, Haworth, and Shoemaker retained similar quantities of ice as other cold

traps over all depths (Figure 4.9), most ice was concentrated near the base of their columns (Figure 4.10). The most valuable targets for radar assuming penetration depth of 100 m (Fa, 2013) would be Amundsen, Cabeus, Cabeus B, and Idel'son L, which each retained >= 4 m of ice in the upper 100 m in half of model runs (> 1 m in 95% of runs). Faustini, Haworth, Shoemaker, and de Gerlache may also be targets of interest, retaining >= 1 m of ice in the upper 100 m in half of model runs (> 0.2 m in 95% of runs).

The Artemis exploration zone is centered on the lunar south pole, which lies on the rim of Shackleton crater. Our model does not predict ice retention in Shackleton crater in the vast majority of model runs, due to its relatively recent formation age and proximity to the south pole, consistent with orbital observations(Haruyama et al., 2008; Zuber et al., 2012). However, the absence of large subsurface ice layers in our model does not preclude the discovery of ice near the surface of Shackleton crater. Ice redistribution or a recent icy impactor could result in near-surface ice in the Shackleton cold trap. If a significant quantity of ice was discovered at depth below Shackleton, it would suggest that our model underestimates subsurface ice storage and could indicate that other cold traps may also store ice more efficiently than predicted here. Future exploration of south polar cold traps would therefore provide crucial constraints on our understanding of recent and historical ice delivery, as well as the potential for geologic deposits of ice at depth.

4.6 Conclusion

Understanding the location, quantity, and form of buried ice is critical for future mission planning. Impact cratering is thought to be the main source of polar ice, while ejecta from impact craters may preserve ice deposits over geologic time. However, impact crater ejecta could mix and volatilize ice through ballistic sedimentation. We developed a thermal model to predict ice loss due to ballistic sedimentation. We applied our findings to a Monte Carlo polar ice and stratigraphy model and determined that ballistic sedimentation disrupts "gigaton" style deposits reported by Cannon et al. (2020). Ice deposits in out model had smaller volume and layer sizes, particularly for older and deeper modeled ice layers.

We applied our model to cold trap regions within the Artemis exploration zone. We found that Amundsen, Cabeus, Cabeus B, and Idel'son L craters retained the greatest quantities of ice potentially detectable with ground penetrating radar. We found significant variance in model predictions for near-surface ice deposits, indicating that shorter term processes dominate ice retention in the upper 10 m. Although our model is inconclusive for surface level deposits, Faustini, de Gerlache, and Amundsen craters retained the greatest quantities in the upper 6 m, and may be better targets for instruments with < 10 m depth sensitivity than other cold traps in this study. Of the modeled cold traps, Shackleton was least likely to retain subsurface ice due to its young formation age, proximity to the pole, and lack of preserving ejecta layers deposited after

its formation. Model variance due to the precise sequencing of cold trap formation, ejecta deposition, and ice delivery events will be constrained by dating samples returned by upcoming missions from the Artemis program. We showed that basin ice and ejecta delivery play crucial roles in retention of ice at the lunar south pole. Buried ice deposits beneath lunar polar cold traps have likely been exposed to reworking by ballistic sedimentation, and are thinner and less extensive than previously reported.

4.7 Open Research

The MoonPIES Python package is open source and publicly available on GitHub (`https://github.com/cjtu/moonpies`) for use under the MIT license. The version of the model used in this work (v1.0.0) is installable at `https://doi.org/10.5281/zenodo.7055800` (Tai Udovicic et al., 2022a). All data generated in this work (Data Sets S1 to S7, Appendix C) are available at `https://doi.org/10.5281/zenodo.7058818` (Tai Udovicic et al., 2022b)

4.8 Acknowledgements

This work was supported by the 2021 Exploration Science Summer Internship hosted by the Lunar and Planetary Institute (LPI) and the Universities Space Research Association (USRA). Funding was provided by the NASA Solar System Exploration Research Virtual Institute (NNXA14AB07A, PI D. A. Kring). The authors thank J. Stopar, E. Costello, and P. Hayne for critical conversations that aided the development of this work.

Chapter 5

Discussion & Conclusion

Over the three preceding chapters, I presented three investigations into the origin and distribution of water on the Moon. Some of the key outstanding questions that I sought to answer were: *How quickly is the lunar surface altered due to space weathering? Does OH / H_2O migrate across the lunar surface on daily timescales? How much ice could be buried below permanently shadowed regions near the south pole?* Taken together in the context of recent developments in the study of lunar hydration, these investigations reveal important constraints on the origin and behavior of water on the lunar surface. Here, I summarize my findings and look ahead to the future lunar missions that will usher in a new era of understanding water on the Moon and beyond.

In chapter 2, *Manuscript I: New Constraints on the Lunar Optical Space Weathering Rate*, I investigated the rate of space weathering in the lunar highlands over the last 1 Ga. Since space weathering processes, including solar wind irradiation and micrometeorite bombardment, have been shown to produce OH / H_2O in lunar regolith analogs, understanding the rate of space weathering over time is one component of understanding the active production of water on the lunar surface (see §1.5). Although we lack a clear understanding of exactly how the majority of the widespread lunar OH / H_2O was produced and where it is stored in the regolith, it has been hypothesized that water production can be a direct result of submicroscopic iron ($smFe^0$) formation (Housley et al., 1973). Therefore, understanding $smFe^0$ formation rate may be a proxy for understanding OH / H_2O formation. Through my analysis of the ejecta of Copernican lunar craters, I found that $smFe^0$ accumulates at a predictable rate in logarithmic time. This means that each unit increase of $smFe^0$ in the regolith takes about 10 times longer than the last. Although the exact formation mechanism of $smFe^0$ and whether it is related to OH / H_2O formation is debated, the slowing rate of $smFe^0$ accumulation may be related to a slower rate of OH / H_2O production in mature lunar soils. However, maps of the widespread 3 µm feature do not show signs of OH / H_2O depletion near fresh craters, unlike maps of $smFe^0$. This would indicate that OH / H_2O abundance is native to the lunar regolith or that it saturates on much shorter timescales than $smFe^0$ ($\sim$1 Ga). An endogenic source of the widespread OH / H_2O signature was

suggested by Chang'E 5 observations which showed that surface OH / H_2O measurements predicted similar abundances of OH as were found in apatite grains of returned samples (Liu et al., 2022). However, previous studies of Apollo samples showed that OH content was related to solar wind implantation in agglutinitic glass (Liu et al., 2012). Therefore, it appears that a combination of endogenic and exogenic OH / H_2O is present in the regolith, but which source (or relative combination of the two) produces the widespread OH / H_2O signature is still unknown.

In a recently published paper which follows on from the publication of chapter 2 (Tai Udovicic et al., 2021a), Jordan et al. (2022) developed a model which accounted for surface space weathering and mixing by impact gardening. As a co-author on this work, I determined that nanophase and microphase iron are well-correlated in their accumulation over time. Although chapter 2 suggested that the different rates of accumulation of nanophase and microphase iron could indicate independent processes acting at each scale, the correlation between the two and consideration of impact gardening argue in favor of a consistent set of processes for both $smFe^0$ sizes. The Jordan et al. (2022) model accounts for the depth of penetration of space weathering and the timescale over which surface weathering products are mixed into the subsurface. The best fit space weathering penetration depths exceeded the penetration depth of typical solar wind irradiation, but were consistent with the penetration depths of micrometeorites. Also, the penetration depth derived for nanophase iron was indistinguishable from that of microphase iron, indicating consistency between the formation processes of each size of $smFe^0$. These results suggest that micrometeorites must be central to the formation of $smFe^0$ at the rates determined in chapter 2. However, micrometeorites produce agglutinates which have been shown to contain solar wind implanted OH (Liu et al., 2012), and it is still unclear if the solar wind is a necessary precursor to produce the observed rates of $smFe^0$ production (§1.5). More work is needed to understand the relative contributions of the solar wind and micrometeorites to $smFe^0$ and OH / H_2O production.

In chapter 3, *Manuscript II: Roughness Reveals Persistent OH/H_2O on the Moon from Equatorial to High Latitudes*, I investigated the widespread 3 µm OH / H_2O absorption feature and its variability with latitude and local time. To accurately interpret the OH / H_2O 3 µm feature, I updated and validated a thermal model that accounts for the roughness of the lunar surface. Using the roughness thermal model to correct Moon Mineralogy Mapper (M^3) spectra, I found that the 3 µm absorption feature was prominent regardless of local time and latitude, in contrast to previous investigations that did not account for roughness (Clark et al., 2011; Li & Milliken, 2017). This strong persistent OH / H_2O signature indicates that hydroxyl or water is present in all lunar regolith in detectable quantities, regardless of location and time of day. Since I observed no significant variation in OH / H_2O regardless of terrain composition, it would appear that either the abundance of OH / H_2O is close to uniform across the lunar surface or that the portion of the 3 µm

signature resolvable in M^3 data is saturated at typical lunar surface OH / H_2O abundances. If the surface is uniform in OH / H_2O content, it is unlikely that endogenic water is the primary source since interior water content would be expected to change as lunar magma evolved; the highlands, maria, and pyroclastic deposits formed at different points in lunar magmatic history and would be unlikely to sequester the same quantity of water/hydroxyl. Therefore, barring instrument saturation, the uniformity in OH / H_2O feature would suggest that it is a natural consequence of space weathering, independent of surface composition. This is consistent with recent laboratory experiments which found that solar wind ion irradiation of lunar samples introduces a strong and broad OH feature which dominates the 3 µm region (McLain et al., 2021). Since no variation is observed in the 3 µm feature with surface age, a solar wind implanted source of OH / H_2O must quickly saturate to the uniform value observed across the surface. Although we cannot distinguish OH from H_2O at 3 µm, recent observations at 6 µm by the Stratospheric Observatory for Infrared Astronomy (SOFIA) gave direct evidence of H_2O (and not just OH) on the daylit lunar surface (Honniball et al., 2020). Consistent with our 3 µm observations, the 6 µm feature does not show signs of diurnal variation, indicating it is likely trapped in impact glasses or hydrated minerals (Honniball et al., 2022). Therefore, the widespread 3 µm feature may be sensing the strongly-bound H_2O observed by SOFIA. To unravel the relative contributions of OH and H_2O to the widespread 3 µm feature, we require observations that capture the full 3 µm absorption feature with better spatial and thermal calibration. More *in-situ* infrared measurements from landers coupled with sample return (e.g., Chang'E 5; Liu et al. 2022) will also be critical to ground-truth these remotely observed signatures and correlate them with the measured abundances of OH / H_2O in the regolith.

From the results of chapter 2 and chapter 3, it appears that the widespread OH / H_2O on the Moon is explainable by space weathering, or perhaps endogenic sources, and does not require any source of daily migrating H_2O. Surface OH / H_2O that can survive the high temperatures and harsh space environment throughout the lunar day is unlikely to be easily extracted from the regolith. Therefore, in chapter 4, *Manuscript III: Buried Ice Deposits in Lunar Polar Cold Traps were Disrupted by Ballistic Sedimentation*, I investigated possible water ice reservoirs below south polar permanently shadowed regions (PSRs). Previous work suggested that large, relatively pure layers of water ice could be preserved below layers of ejecta from nearby craters (Cannon et al., 2020; Kring, 2020). However, those studies did not account for the heating and mixing (*ballistic sedimentation*) of buried ice as crater ejecta is deposited into a permanently shadowed region (PSR). To address this gap, I developed a thermal model that estimates the quantity of ice lost during a given ballistic sedimentation event. I also made several key updates to the previous ice and ejecta stratigraphy model and investigated how much ballistic sedimentation would disturb buried ice layers. I found that total ice retention fell when accounting for ballistic sedimentation, but that meters-thick layers could still exist below several PSRs. Most of the remaining water ice layers were 10s to 100s of meters

below the surface. Therefore, the model predicts that the majority of buried water ice occurs below the depth of typical drill cores (∼1 m) and would require deeper subsurface probing methods to detect. In addition to informing the potential depth of water ice layers, this investigation also made predictions about the properties of ice we expect to find below the surface. We found that most ice layers were influenced by ballistic sedimentation. Therefore, we infer that most large ice deposits have been mixed into the regolith and are unlikely to remain as coherent layers. In addition, any water ice found near the surface, where our model finds little to no ice, is more likely to have been produced *in-situ* by space weathering or delivered very recently. Alternatively, ice layers may migrate to subsurface stability zones at depth through thermal effects not accounted for in this model (Schorghofer & Aharonson, 2014). The ice predictions in this study are valuable for ongoing mission planning efforts as the NASA Artemis program prepares to send robotic and human missions to the south polar region. If these exploratory missions confirm that usable quantities of water ice exist on or below PSRs, it could revolutionize the future of space exploration. Since H_2O can be readily synthesized into costly rocket propellant (Kornuta et al., 2019) lunar water could significantly lower the cost of space travel throughout the Solar System. Through these three studies, I have unraveled part of the complex tapestry of water interactions on the lunar surface. With many missions planned to further characterize lunar OH / H_2O *in-situ* and from orbit, the insights gained here will help plan and interpret the coming deluge of data which promises to revolutionize our understanding of water on the Moon.

5.1 Conclusion

Through the three investigations presented here, I found evidence for a predictable space weathering rate, a prominent widespread OH / H_2O feature that survives the lunar day, and buried water ice layers near the lunar south pole. The space weathering rates derived in chapter 2 may be useful for tracking the production of OH / H_2O, but more work is needed to determine the precise mechanism and source of $smFe^0$ on the Moon. Taken together with the observation in chapter 3 that OH / H_2O is not diurnally migrating, it appears that space weathering could be the primary source of the widespread water / hydroxyl signature. However, since the widespread OH / H_2O survives the harsh lunar day, it is probably tightly sequestered in impact glasses or hydrated minerals. Therefore, the widespread OH / H_2O is unlikely to be easily extracted from the surface in usable quantities. In chapter 4, I searched for usable lunar water near the lunar south pole, where permanently shadowed regions may contain water ice reservoirs. By improving a previous model of polar ice stratigrphy, I predicted that large ancient ice deposits could be present 10s to 100s of meters below the the surface. The investigations here contribute a few pieces to the puzzling origin and distribution of water on the Moon. With an unprecedented number of remote and *in-situ* missions planned this decade

to observe the widespread OH / H_2O feature, and possibly sample water ice near the south pole, we are presently on the cusp of a new chapter of understanding water on the Moon and beyond.

Several upcoming landed missions will investigate the *in-situ* space weathering and hydration environment on the Moon. In particular, Lunar Vertex will land at the Reiner Gamma lunar swirl and will help characterize the relative space weathering effects of solar wind and micrometeorite bombardment (Blewett et al., 2022). The NIRVSS instrument has a hyperspectral near-infrared spectrometer which will search for variability in the widespread OH / H_2O feature from a lander in the Lacus Mortis mare region (Roush et al., 2020). The L-CIRiS instrument will land near the south pole to characterize the thermal properties and OH / H_2O content of micro-cold traps (small areas capable of trapping water outside the large PSRs; Hayne et al. 2019). These missions will be complemented by a host of orbital and flyby spacecraft missions which will characterize OH / H_2O widespread on the lunar surface and in polar PSRs. Among these are a polar hydrogen mapper, LunaH-Map (Hardgrove et al., 2020); a hyperspectral visible to near-infrared mapper, Lunar Ice Cube (Malphrus et al., 2019); a hyperspectral near-infrared and multispectral mid-infrared mapper, Lunar Trailblazer (Ehlmann et al., 2022); and a rover which will search for volatiles in PSRs, VIPER (Colaprete et al., 2019). In addition, the NASA Artemis program intends to return humans to the lunar surface for the first time since the end of the Apollo era five decades ago. Artemis plans to return the first samples from the lunar south pole, which have the potential to revolutionize our understanding of water on the Moon. These crewed and uncrewed missions promise to rapidly advance our understanding of lunar OH / H_2O, its endogenic and exogenic source(s), and its availability for use in future space exploration. At turning points like these, it is critical to look forward and lay the groundwork upon which future breakthrough discoveries will be built. Through the investigations presented here, I advanced our understanding of water on the Moon in the spirit of open and collaborative science. As we begin a new generation of human space exploration, it is crucial to prioritize ethical, sustainable, open and reproducible science *now* as a foundation for all future generations to build upon.

Acronyms

CC BY 4.0 Creative Commons Attribution 4.0

CLSE Center for Lunar Science and Exploration

CSV comma-separated values

DAPS Department of Astronomy and Planetary Science

DOI Digital Object Identifier

FINESST Future Investigators in NASA Earth and Space Science and Technology

GRL Geophysical Research Letters

ISRO Indian Space Research Organisation

JAXA Japan Aerospace Exploration Agency

LAMP Lyman Alpha Mapping Project

LCROSS Lunar Crater Observation and Sensing Satellite

LDAP Lunar Data Analysis Program

LPI Lunar and Planetary Institute

LRO Lunar Reconnaissance Orbiter

LROC Lunar Reconnaissance Orbiter Camera

M^3 Moon Mineralogy Mapper

MI Multiband Imager

MIT Massachusetts Institute of Technology

MoonPIES Moon Polar Ice and Ejecta Stratigraphy

NASA National Aeronautics and Space Administration

NAU Northern Arizona University

OMAT Optical Maturity

PIXEL Planetary Instrumentation Experimentation and Exploration Laboratory

PSR permanently shadowed region

SELENE SELenological and ENgineering Explorer

smFe^0 submicroscopic iron

SOFIA Stratospheric Observatory for Infrared Astronomy

SSERVI Solar System Exploration Research Virtual Institute

TOPS Transform to Open Science

USRA Universities Space Research Association

WAC Wide Angle Camera

Appendix A

Supplementary Information for Chapter 2: Manuscript I

Supplementary material for chapter 2, *Manuscript I: New Constraints on the Lunar Optical Space Weathering Rate* is listed here. It describes supplemental data sets available at `https://doi.org/10.1029/2020GL092198` that are required to reproduce each figure (Tai Udovicic et al., 2021a). Supplemental figures describe the spatial distribution of the sampled craters and the sensitivity of the derived fits.

Data Set S1.

Data Set S1 is a comma separated values (csv) file of all craters used in the Global analysis and is sufficient to reproduce Figure 2. Its columns are: Name, Latitude (Lat), Longitude (Lon), Radius, Mean, Standard deviation and Size (number of valid pixels) of nanophase iron (mean_npfe, std_npfe, size_npfe), and microphase iron (mean_mpfe, std_mpfe, size_mpfe), Dataset (ds), and Reference (Ref). Dataset is abbreviated as a two letter code, corresponding to: Cold Spot (cs), OMAT young (oy), OMAT Intermediate (oi), OMAT Old (oo), LPI Copernican (lc), LPI Eratosthenian (le), and LPI Imbrian (li). Refer to the Reference of each crater for details about age determination and methodology.

Data Set S2.

Data Set S2 is a comma separated values (csv) file of all craters used in the Highlands analysis and is sufficient to reproduce the data and fits in Figure 3 and Figure S1. Its columns are: Name, Latitude (Lat), Longitude (Lon), Radius, Age, Lower Age error (Agelow), Upper Age error (Ageupp), Mean, Standard deviation and Size (number of valid pixels) of nanophase iron (mean_npfe, std_npfe, size_npfe), and microphase iron (mean_mpfe, std_mpfe, size_mpfe), Dataset (ds), and Reference (Ref). Dataset is abbreviated as a two letter code, corresponding to: Cold Spot (cs), Chronology (ch), and Rock Abundance (ra). Refer to the Reference of each crater for details about age determination and methodology.

Data Set S3.

Data Set S3 is a comma separated values (csv) file of the LPI Highlands Saturation range craters and is sufficient to reproduce the saturation ranges shown on Figure 3 and Figure S1. Its columns are: Name, Latitude (Lat), Longitude (Lon), Radius, Age, Mean, Standard deviation and Size (number of valid pixels)

of nanophase iron (mean_npfe, std_npfe, size_npfe), and microphase iron (mean_mpfe, std_mpfe, size_mpfe), Dataset (ds), and Reference (Ref) for each crater used to produce the highlands saturation ranged in Fig. 3. Dataset is set to "hlsat" for "LPI Highlands Saturation". Refer to the Reference of each crater for details about age determination and methodology.

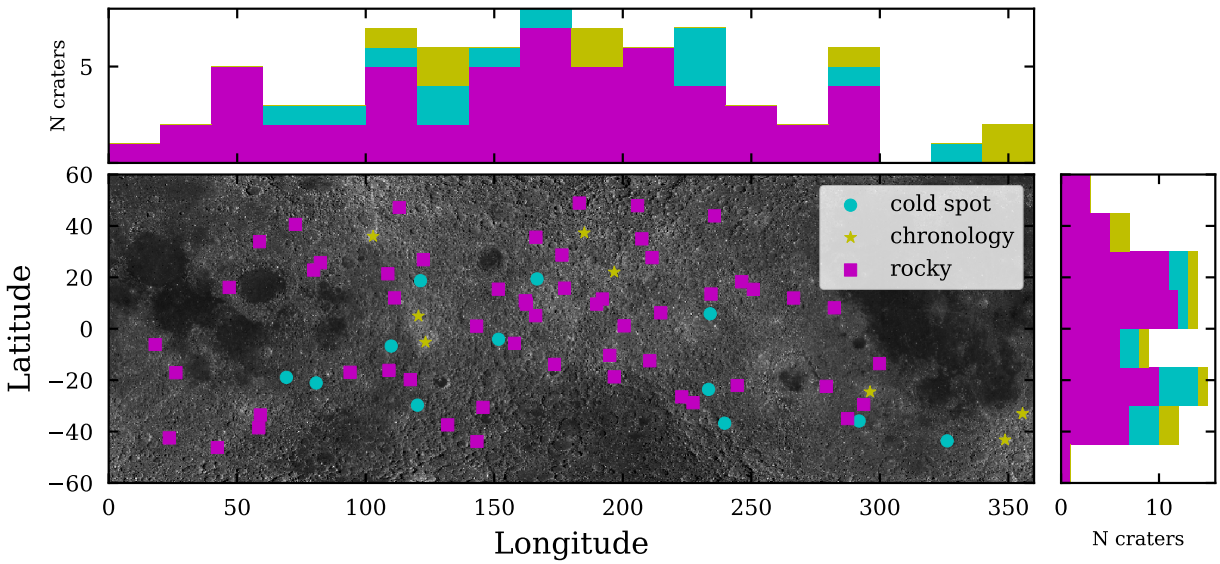

Figure A.1: Distribution of dated highlands craters in our sample shown on the Lunar Reconnaissance Orbiter (LRO) Wide Angle Camera (WAC) mosaic (Speyerer et al., 2011). Stacked histograms show the number of cold spot, chronology, and rocky highlands craters in each 20^o longitude bin (top) and each 15^o latitude bin (right).

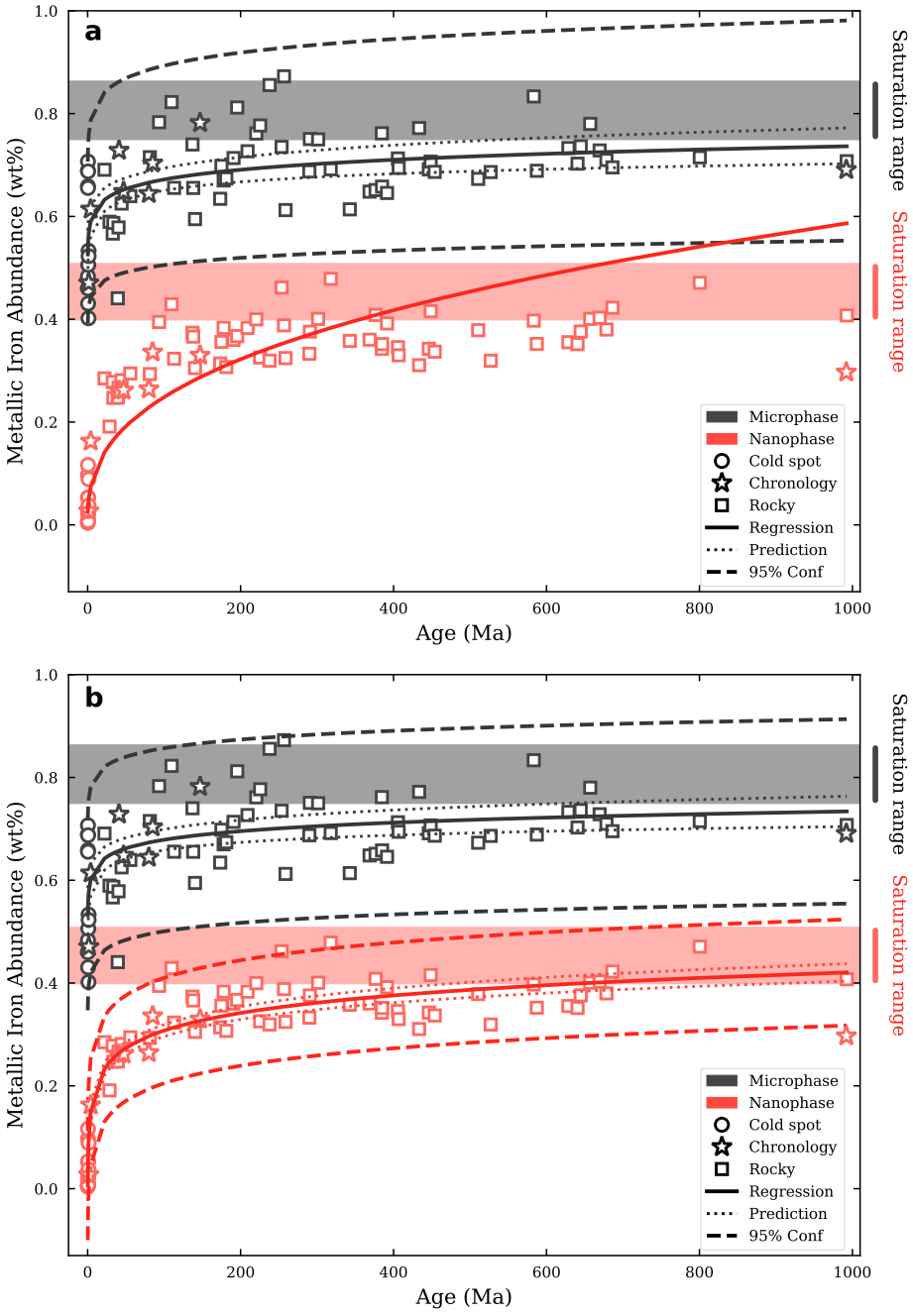

Figure A.2: Linear-linear axis plots of fits in Fig. 3. **a** Power law fits in Fig. 3a shown on linear axes. **b** Logarithmic fits in Fig. 3b shown on linear axes.

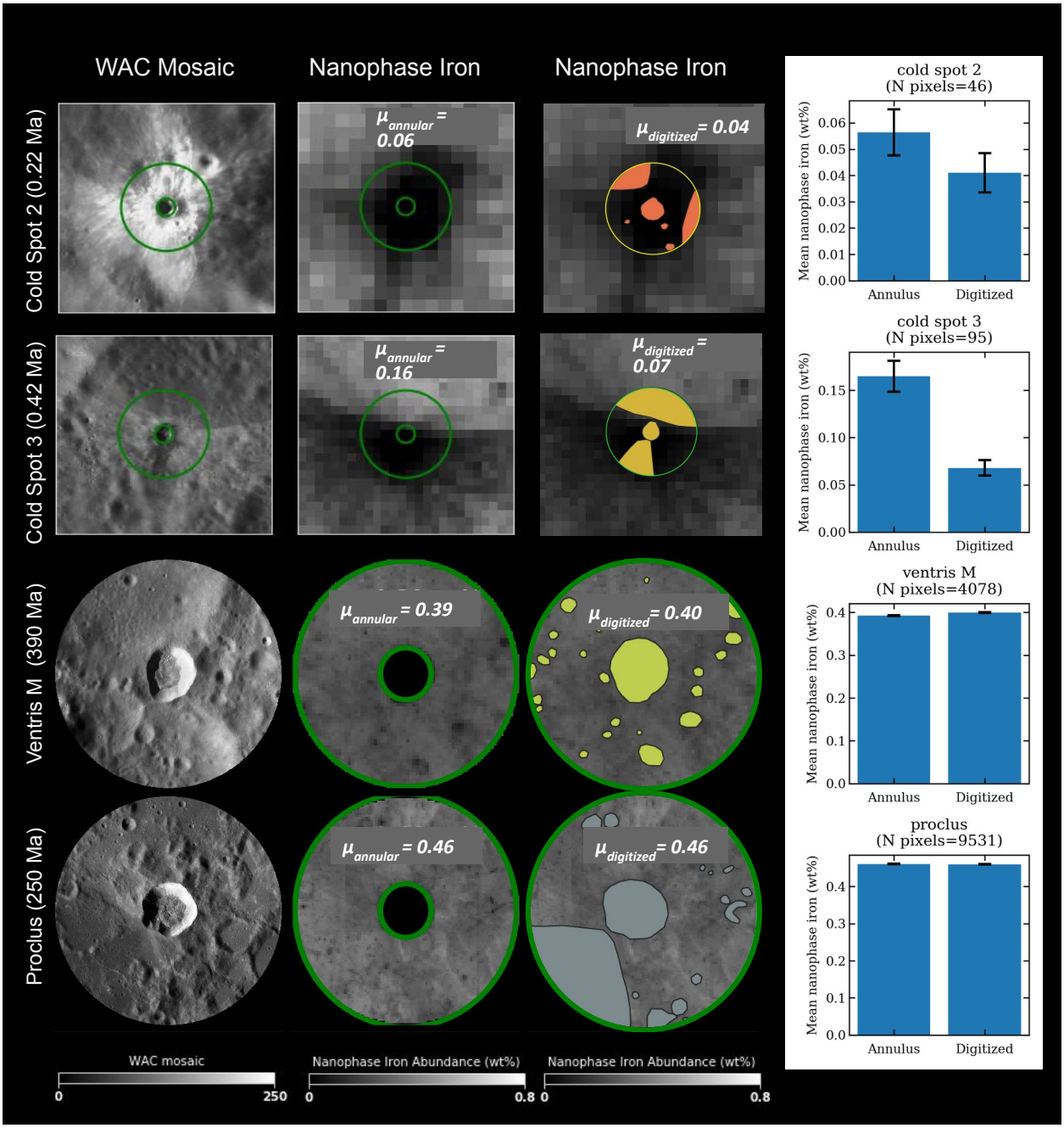

Figure A.3: We test the influence of ejecta anomalies on the mean annular nanophase and microphase iron of four craters. We find that digitizing asymmetric ejecta and excluding small superposed craters may reduce the mean and standard error nanophase iron of smaller craters in our sample. Digitizing ejecta anomalies of larger craters appears to have negligible effects.

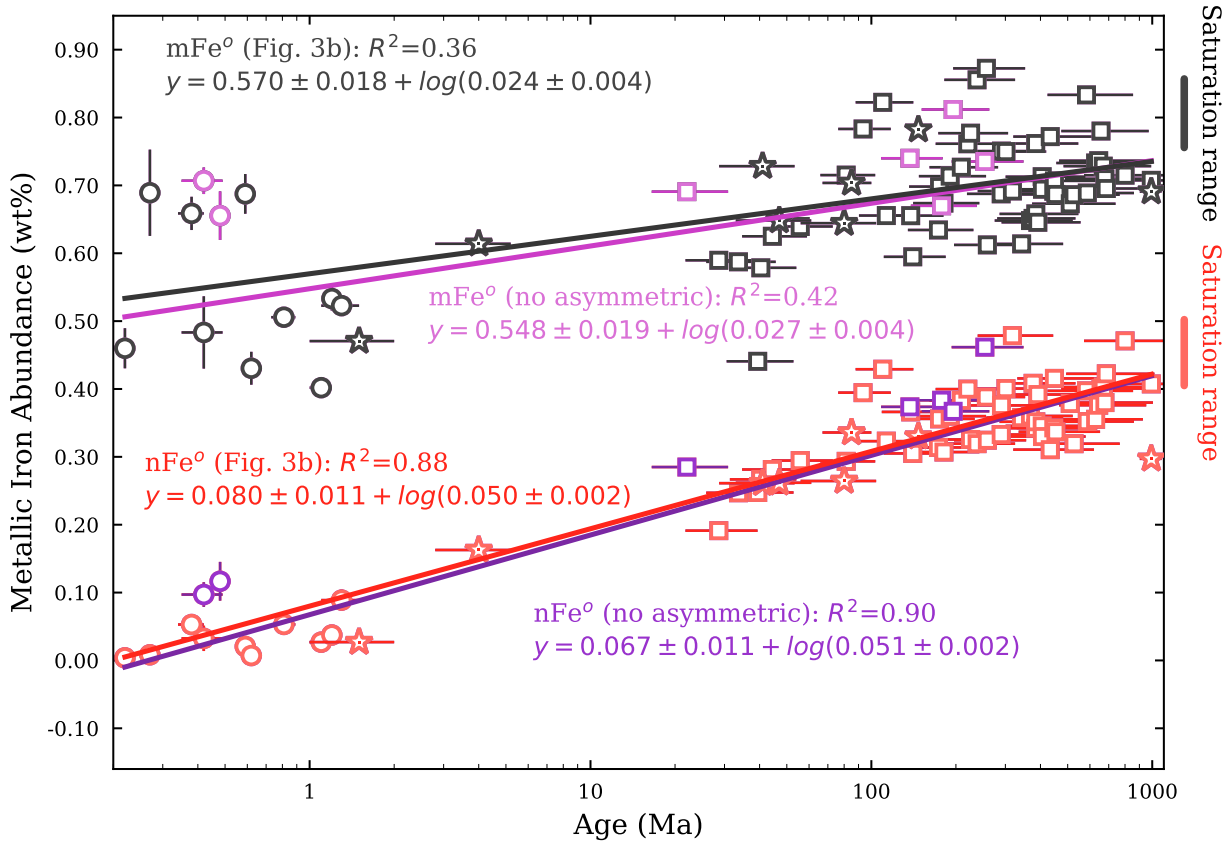

Figure A.4: We test the influence of craters with asymmetric ejecta on our logarithmic fits (Fig. 3b). We plot in purple the 7/75 asymmetric ejecta craters in our highlands sample (9%); 0 are chronology craters, 2/12 are cold spot craters (17%), and 5/75 are rock abundance craters (9%). We note that nanophase and microphase iron of asymmetric ejecta craters systematically plot above our fits, consistent with the ejecta annulus incorporating mature background material in these cases. Despite being systematically enhanced, the overall effect of removing these points is negligible and the new fits are well within the 95% confidence intervals of the presented in Fig. 3b.

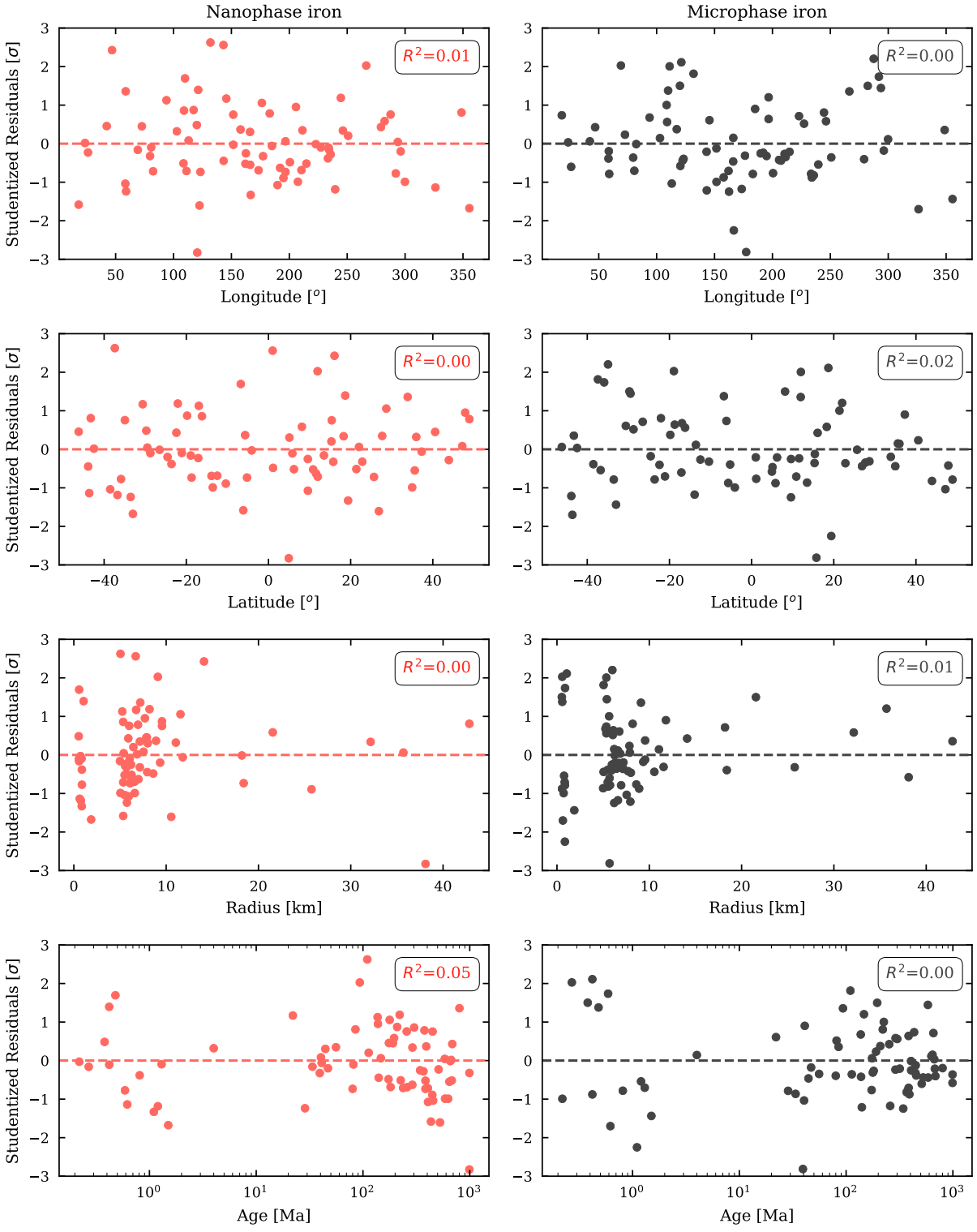

Figure A.5: Studentized residuals of the linear-logarithmic fits (Fig. 3b) with longitude, latitude, crater radius, and age. We observe no systematic bias in the residuals of our fit with location, crater size, or age.

Appendix B

Supplementary Information for Chapter 3: Manuscript II

Supplementary material for chapter 3, *Manuscript II: Roughness Reveals Persistent OH/H_2O on the Moon from Equatorial to High Latitudes* is listed here. It includes a table of model parameters used in the KRC thermal model to produce diurnal temperatures of surface facets in a variety of orientations and local conditions described in §3.3.

Table B.1: Model parameters used to run surface temperature predictions in KRC. Case-sensitive parameter names correspond to the named parameters in the Davinci KRC interface (https://krc.mars.asu.edu/).

	Parameter	Value	Description
Lookup Variables	lat	-85°–85°	Latitude (35 bins in 5° increments)
	ALBEDO	0.05–0.225	Bolometric albedo (6 bins in 0.035 increments)
	SLOPE	0°–90°	Surface slope (19 bins in 5° increments)
	SLOAZI	0°–360°	Surface azimuth (19 bins in 20° increments)
	DELLS	4°	L_s step size (90 bins spanning 0°–360°)
Thermal Parameters	EMISS	0.96	Emissivity
	thick	0.05	Upper layer thickness [m]
	DENSITY	1100	Upper layer density [kg/m^3]
	DENS2	1800	Lower layer density [kg/m^3]
	lbound	18	Interior heat flow [mW/m^2]
	PhotoFunc	0.045/albedo	Photometric function (Keihm-style with Vasavada et al. (2012) scaling, relative to 0.045 albedo)
Temperature-dependent parameters	SphUp0/SphLo0	602.88098583	Specific heat capacity (Hayne et al., 2017) expressed as 4th-order polynomial ($c0 + c1 \cdot T + c2 \cdot T^2 + c3 \cdot T^3$)
	SphUp1/SphLo1	235.98988249	
	SphUp2/SphLo2	-29.59742178	
	SphUp3/SphLo3	-3.78707193	
	ConUp0	0.00133644	Upper layer conductivity (Feng et al., 2020) expressed as 4th-order polynomial ($c0 + c1 \cdot T + c2 \cdot T^2 + c3 \cdot T^3$)
	ConUp1	0.00073150	
	ConUp2	0.00033250	
	ConUp3	0.00005038	
	ConLo0	0.00634807	Lower layer conductivity (Feng et al., 2020) expressed as 4th-order polynomial ($c0 + c1 \cdot T + c2 \cdot T^2 + c3 \cdot T^3$)
	ConLo1	0.00347464	
	ConLo2	0.00157938	
	ConLo3	0.00023930	
Model Setup Parameters	body	Moon	Target body
	k_style	Moon	Conductivity style (Moon for airless bodies)
	LKofT	T	Temperature-dependent conductivity
	FLAY	0.01	First layer thickness [m]
	RLAY	1.3	Layer thickness multiplier
	N1	26	Number of layers
	N24	288	Timesteps per day (5 min steps)
	DJUL	0	Start date

Appendix C

Supplementary Information for Chapter 4: Manuscript III

Supplementary material for chapter 4, *Manuscript III: Buried Ice Deposits in Lunar Polar Cold Traps were Disrupted by Ballistic Sedimentation* is listed here. It contains descriptions of supplementary datasets S1 to S7 (ds01.csv to ds07.csv) needed to reproduce figures in chapter 4 (Tai Udovicic et al., 2022b). Supplemental figures describe additional parameters and sensitivity of the Moon Polar Ice and Ejecta Stratigraphy (MoonPIES) model. Python code that generated each figure is available in the `moonpies` repository on GitHub at `https://github.com/cjtu/moonpies` (Tai Udovicic et al., 2022a).

Data Sets S1 and S2.

The comma-separated values (CSV) files, "ds01.csv" and "ds02.csv" contain modeled craters and basins, respectively, in tabular format with columns for their name, latitude (degrees), longitude (degrees), diameter (km), age (Ga), lower and upper age uncertainties (Ga) and references. Data Set S1 has additional columns for the PSR centroid latitude (degrees), longitude (degrees), and total PSR area (km^2) for craters hosting a permanently shadowed region (PSR). Unnamed craters follow the numbering scheme of Cannon et al. (2020). Data Set S2 has three options for basin diameter: main ring, inner ring, and Bouguer (Neumann et al., 2015). Main ring diameter is used for this work.

Data Set S3 and S4.

CSV files, "ds03.csv" contains the mean melt fraction and "ds04.csv" contains the standard deviation melt fraction derived using the ballistic sedimentation thermal model developed in this work. The first row defines ejecta temperatures and the first column defines mixing ratios (target:ejecta). These data are shown in Figure 4. See §2.3.3 for methodology.

Data Set S5.

CSV file, "ds05.csv" contains the ballistic hop efficiency used to compute ice delivery to each modeled coldtrap, expressed as a percentage of total ice delivered to the south polar region. These data are displayed in Figure S1.

Data Set S6.

CSV file, "ds06.csv" contains aggregated data resulting from 10,000 MoonPIES Monte Carlo runs which was used to produce Figures 9 and 11. Columns are multi-indexed by cold trap name, whether ballistic sedimentation was applied (bsed, no_bsed) and the total thickness of ice layers to depths of 6 m, 10 m, 100 m ice, and total as well as the total depth of the column for all generated stratigraphy columns from all 10,000 runs.

Data Set S7.

CSV file, "ds07.csv" contains aggregated layering data resulting from 10,000 MoonPIES Monte Carlo runs which was used to produce Figure 10. Columns are multi-indexed by cold trap name, whether ballistic sedimentation was applied (bsed, no_bsed) and the ice, depth, and time of formation of each non-zero layer from all generated stratigraphy columns from all 10,000 runs.

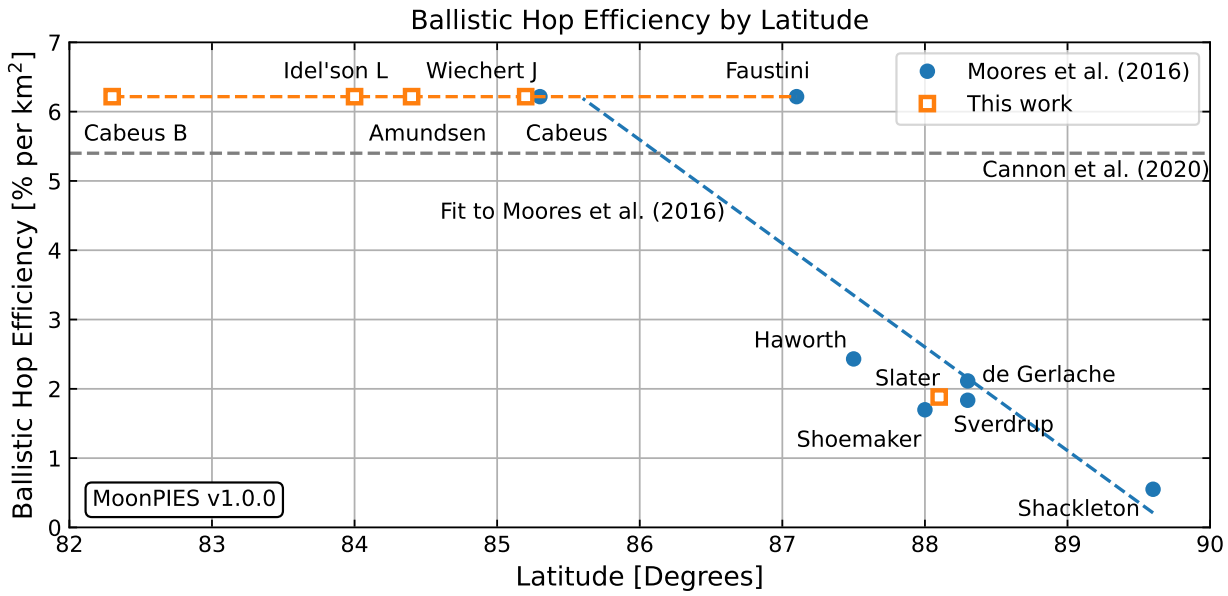

Figure C.1: Ballistic hop efficiency for each cold trap in this work. Blue points are values reported by Moores (2016) and orange squares are those derived here. The average value used in Cannon et al. (2020) is shown in gray.

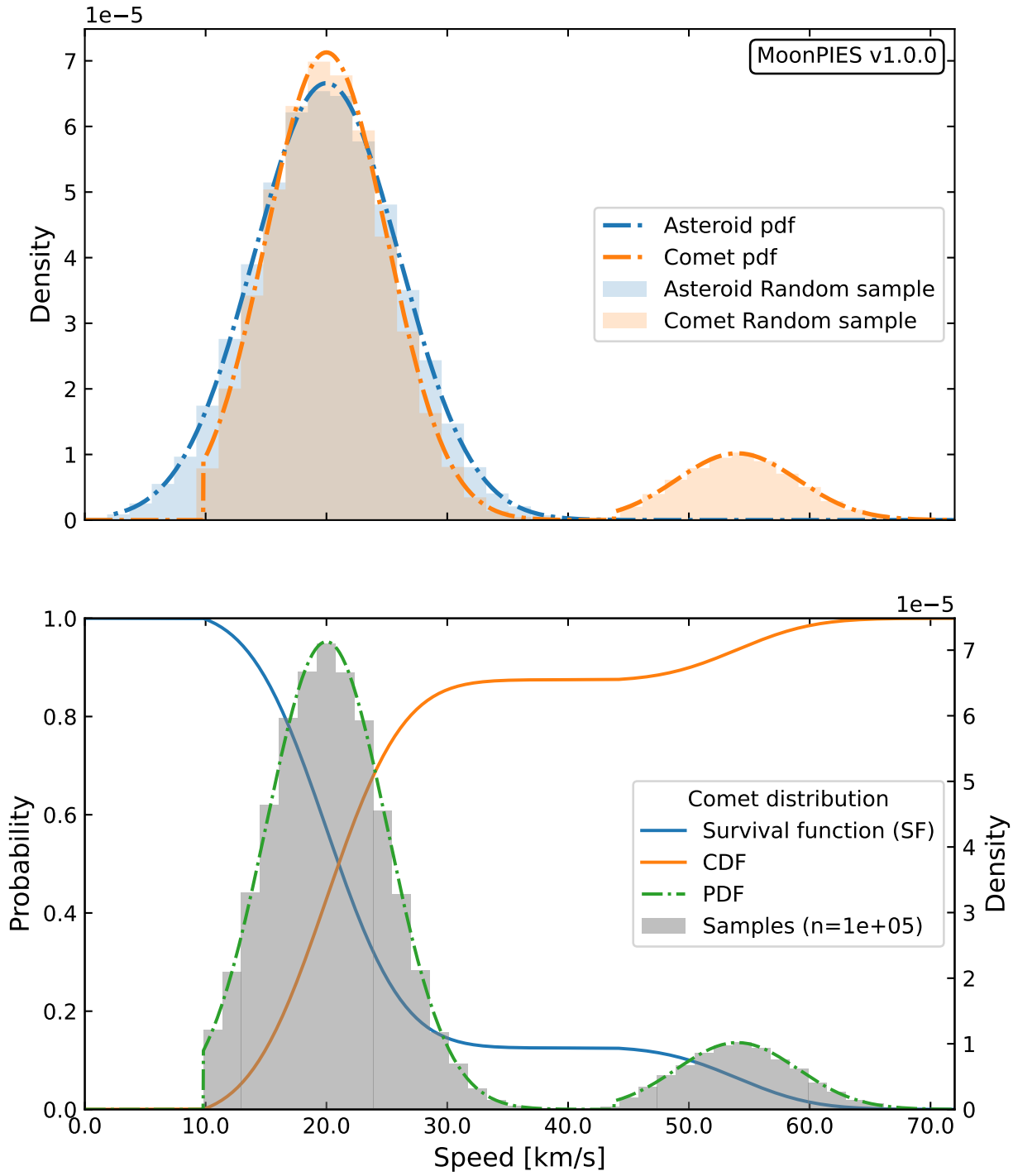

Figure C.2: Comet velocities drawn from bimodal distribution approximating speeds and relative abundances of Jupiter Family Comets and Oort Cloud Comets (Ong et al., 2010).

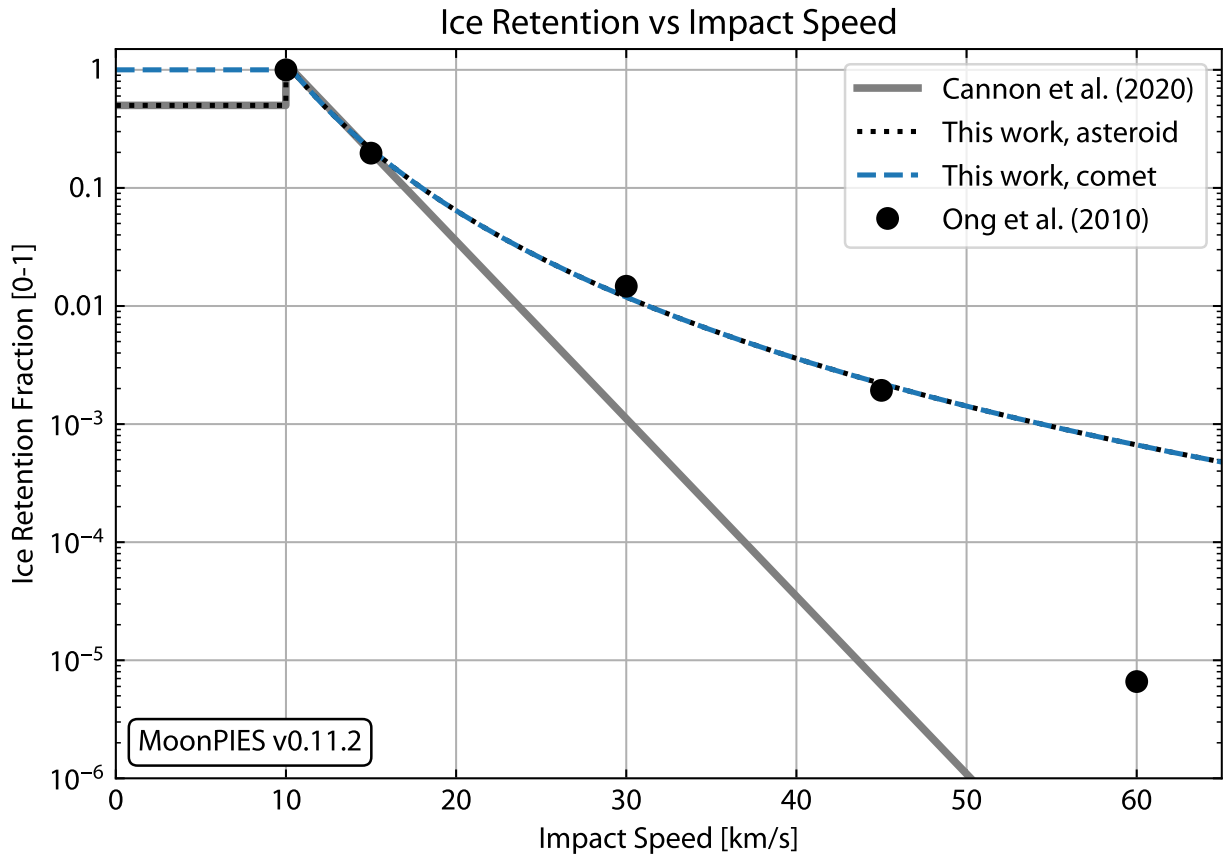

Figure C.3: Mass of impactor retained on the lunar surface vs impact speed from simulations by Ong et al. (2010). The best fit power law is $1.66 \times 10^4 v^{-4.16}$ (excluding the reported outlier at 60 km/s). Our model is insensitive to to the fit at high velocity since high velocity impacts are rare in the model (see Figure C.2) and these velocities correspond to smaller impactors which deliver less ice. Asteroid retention is capped at 50% for consistency with the previous model by Cannon et al. (2020) while comets never have less than 10 km/s.

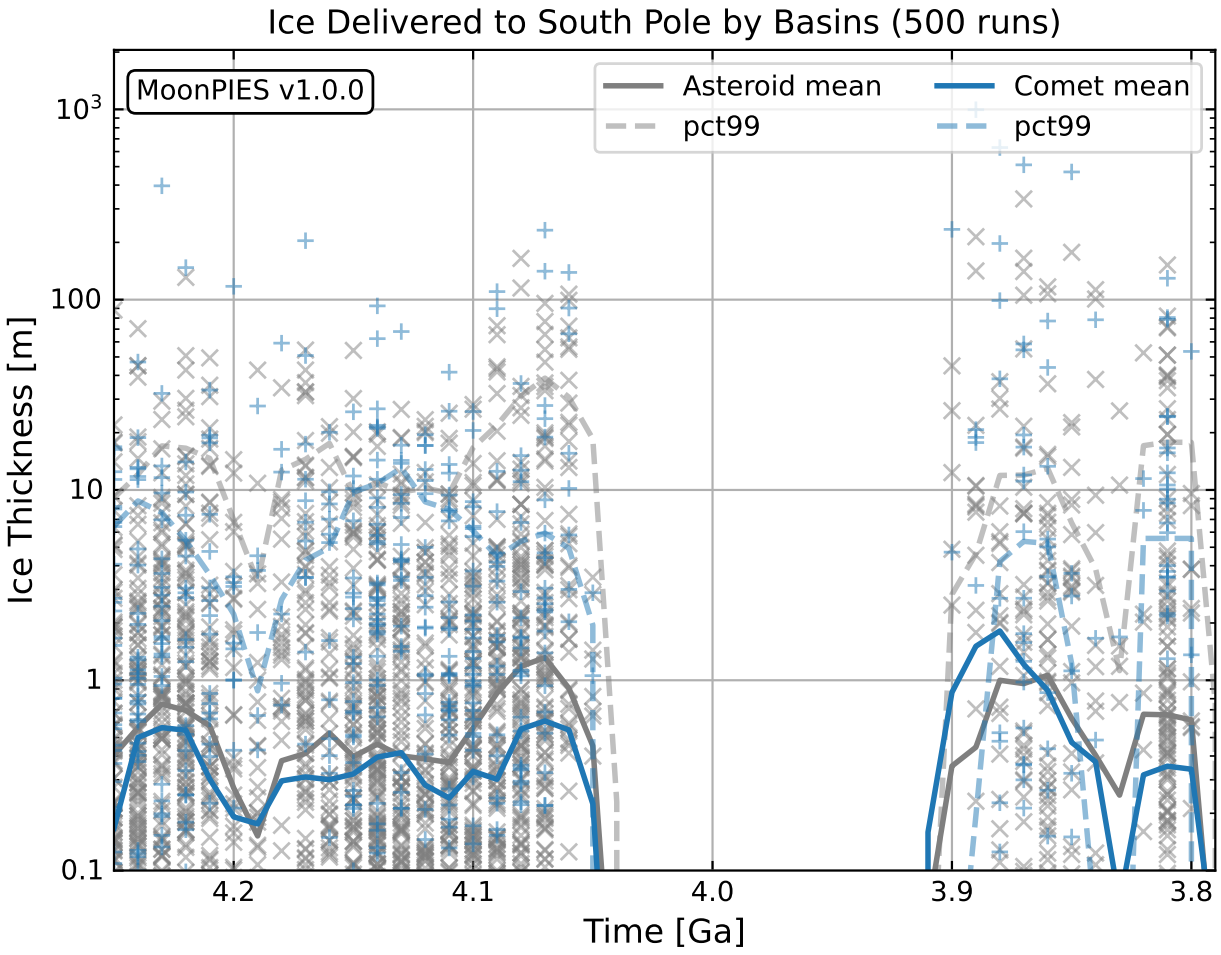

Figure C.4: Ice delivered by asteroidal (grey) and cometary (blue) basins in each 10 Myr timestep over 500 runs. A 30 Myr moving window average (solid) and 99.7th percentile (dashed) show typical and 3 σ basin ice at each timestep.

References

Aleinov, I., Way, M. J., Harman, C., et al. *2019*, *Modeling a Transient Secondary Paleolunar Atmosphere: 3-D Simulations and Analysis*, Geophysical Research Letters, 46, 5107, doi: 10.1029/2019gl082494

Arnold, J. R. *1979*, *Ice in the Lunar Polar Regions*, Journal of Geophysical Research: Solid Earth, 84, 5659, doi: 10.1029/jb084ib10p05659

Artemieva, N. A., & Shuvalov, V. V. *2008*, *Numerical Simulation of High-Velocity Impact Ejecta Following Falls of Comets and Asteroids onto the Moon*, Solar System Research, 42, 329, doi: 10.1134/s0038094608040059

Ashley, J. W., Robinson, M. S., Hawke, B. R., et al. *2012*, *Geology of the King Crater Region: New Insights into Impact Melt Dynamics on the Moon*, Journal of Geophysical Research: Planets, 117, doi: 10/gksdcd

Asphaug, E., & Benz, W. *1994*, *Density of Comet Shoemaker–Levy 9 Deduced by Modelling Breakup of the Parent 'Rubble Pile'*, Nature, 370, 120, doi: 10.1038/370120a0

Bahcall, J. N., Pinsonneault, M. H., & Basu, S. *2001*, *Solar Models: Current Epoch and Time Dependences, Neutrinos, and Helioseismological Properties*, The Astrophysical Journal, 555, 990, doi: 10.1086/321493

Baker, M. *2016*, *1,500 Scientists Lift the Lid on Reproducibility*, Nature, 533, 452, doi: 10.1038/533452a

Bandfield, J. L., & Edwards, C. S. *2008*, *Derivation of Martian Surface Slope Characteristics from Directional Thermal Infrared Radiometry*, Icarus, 193, 139, doi: 10/bfvjnc

Bandfield, J. L., Hayne, P. O., Williams, J. P., Greenhagen, B. T., & Paige, D. A. *2015*, *Lunar Surface Roughness Derived from LRO Diviner Radiometer Observations*, Icarus, 248, 357, doi: 10/f6zq8v

Bandfield, J. L., Poston, M. J., Klima, R. L., & Edwards, C. S. *2018*, *Widespread Distribution of OH/H2O on the Lunar Surface Inferred from Spectral Data*, Nature Geoscience, 11, 173, doi: 10/gc6mz7

Benna, M., Hurley, D. M., Stubbs, T. J., Mahaffy, P. R., & Elphic, R. C. *2019*, *Lunar Soil Hydration Constrained by Exospheric Water Liberated by Meteoroid Impacts*, Nature Geoscience, 12, 333, doi: 10.1038/s41561-019-0345-3

Bickel, V. T., Moseley, B., Hauber, E., et al. *2022*, *Cryogeomorphic Characterization of Shadowed Regions in the Artemis Exploration Zone*, Geophysical Research Letters, 49, doi: 10.1029/2022GL099530

Blewett, D. T., Halekas, J., Ho, G. C., et al. *2022*, *Lunar Vertex: PRISM Exploration of Reiner Gamma*, Lunar and Planetary Science Conference, 2678, 1131

Bohnsack, D., Potten, M., Pfrang, D., Wolpert, P., & Zosseder, K. *2020*, *Porosity–Permeability Relationship Derived from Upper Jurassic Carbonate Rock Cores to Assess the Regional Hydraulic Matrix Properties of the Malm Reservoir in the South German Molasse Basin*, Geothermal Energy, 8, 12, doi: 10.1186/s40517-020-00166-9

Braden, S. E., & Robinson, M. S. *2013*, *Relative Rates of Optical Maturation of Regolith on Mercury and the Moon*, Journal of Geophysical Research: Planets, 118, 1903, doi: 10.1002/JGRE.20143@10.1002/(ISSN)2169-9100.MESSENGER1

Bradley, J. P., Ishii, H. A., Gillis-Davis, J. J., et al. *2014*, *Detection of Solar Wind-Produced Water in Irradiated Rims on Silicate Minerals*, Proceedings of the National Academy of Sciences, 111, 1732, doi: 10.1073/pnas.1320115111

Britt, D. T., & Pieters, C. M. *1994*, *Darkening in Black and Gas-Rich Ordinary Chondrites: The Spectral Effects of Opaque Morphology and Distribution*, Geochimica et Cosmochimica Acta, 58, 3905, doi: 10/fwvm8w

Brown, P., Spalding, R. E., ReVelle, D. O., Tagliaferri, E., & Worden, S. P. *2002*, *The Flux of Small Near-Earth Objects Colliding with the Earth*, Nature, 420, 294, doi: 10.1038/nature01238

Campbell, D. B., Campbell, B. A., Carter, L. M., Margot, J.-L. L., & Stacy, N. J. S. *2006*, *No Evidence for Thick Deposits of Ice at the Lunar South Pole*, Nature, 443, 835, doi: 10/fwjwdm

Cannon, K. M., Deutsch, A. N., Head, J. W., & Britt, D. T. *2020*, *Stratigraphy of Ice and Ejecta Deposits at the Lunar Poles*, Geophysical Research Letters, 47, doi: 10.1029/2020gl088920

Carrillo-Sánchez, J. D., Nesvorný, D., Pokorný, P., Janches, D., & Plane, J. M. C. *2016*, *Sources of Cosmic Dust in the Earth's Atmosphere*, Geophysical Research Letters, 43, 11,979, doi: 10.1002/2016GL071697

Carslaw, H. S., & Jaeger, J. C. 1959, Conduction of Heat in Solids, 2nd edn. (Oxford : Clarendon Press)

Cassidy, W., & Hapke, B. *1975*, *Effects of Darkening Processes on Surfaces of Airless Bodies*, Icarus, 25, 371, doi: 10/bsh4wm

CBPFOCPNSS, Space Studies Board, Division on Engineering and Physical Sciences, & National Academies of Sciences, Engineering, and Medicine. 2018, Open Source Software Policy Options for NASA Earth and Space Sciences, Committee on Best Practices for a Future Open Code Policy for NASA Space Science (CBPFOCPNSS) (Washington, D.C.: National Academies Press), 25217, doi: 10.17226/25217

Chauhan, P., Chauhan, M., Verma, P. A., et al. *2021*, *Unambiguous Detection of OH and H2O on the Moon from Chandrayaan-2 Imaging Infrared Spectrometer Reflectance Data Using 3 M m Hydration Feature*, Current Science, 121, 11, doi: 10.18520/cs/v121/i3/391-401

Chin, G., Brylow, S., Foote, M., et al. *2007*, *Lunar Reconnaissance Orbiter Overview: The Instrument Suite and Mission*, Space Science Reviews, 129, 391, doi: 10.1007/s11214-007-9153-y

Christoffersen, R., Dukes, C., Keller, L., Rahman, Z., & Baragiola, R. *2015*, *Problems at the Leading Edge of Space Weathering as Revealed by TEM Combined with Surface Science Techniques*, Space Weathering of Airless Bodies: An Integration of Remote Sensing Data, Laboratory Experiments and Sample Analysis Workshop, 1878, 2065

Chyba, C. F. *1991*, *Terrestrial Mantle Siderophiles and the Lunar Impact Record*, Icarus, 92, 217, doi: 10.1016/0019-1035(91)90047-w

Clark, R. N. *2009*, *Detection of Adsorbed Water and Hydroxyl on the Moon*, Science, 326, 562, doi: 10/fmsp93

Clark, R. N., Pieters, C. M., Green, R. O., Boardman, J. W., & Petro, N. E. *2011*, *Thermal Removal from Near-Infrared Imaging Spectroscopy Data of the Moon*, Journal of Geophysical Research, 116, E00G16, doi: 10.1029/2010JE003751

Colaprete, A., Andrews, D., Bluethmann, W., et al. *2019*, *An Overview of the Volatiles Investigating Polar Exploration Rover (VIPER) Mission*, American Geophysical Union Fall Meeting, 2019, P34B

Colaprete, A., Schultz, P., Heldmann, J., et al. *2010*, *Detection of Water in the LCROSS Ejecta Plume*, Science, 330, 463, doi: 10.1126/science.1186986

Corripio, J. G. *2003*, *Vectorial Algebra Algorithms for Calculating Terrain Parameters from DEMs and Solar Radiation Modelling in Mountainous Terrain*, International Journal of Geographical Information Science, 17, 1, doi: 10.1080/713811744

Costello, E. S., Ghent, R. R., Hirabayashi, M., & Lucey, P. G. *2020*, *Impact Gardening as a Constraint on the Age, Source, and Evolution of Ice on Mercury and the Moon*, Journal of Geophysical Research: Planets, 125, doi: 10.1029/2019je006172

Costello, E. S., Ghent, R. R., & Lucey, P. G. *2018*, *The Mixing of Lunar Regolith: Vital Updates to a Canonical Model*, Icarus, 314, 327, doi: 10/gksdcp

—. *2021*, *Secondary Impact Burial and Excavation Gardening on the Moon and the Depth to Ice in Permanent Shadow*, Journal of Geophysical Research: Planets, 126, e2021JE006933, doi: 10/gpdvhx

Croft, S. K. *1985*, *The Scaling of Complex Craters*, Journal of Geophysical Research: Solid Earth, 90, C828, doi: 10.1029/jb090is02p0c828

Deutsch, A., Head III, J., & Newmann, G. *2020*, *Analyzing the Ages of South Polar Craters on the Moon: Implications for the Sources and Evolution of Surface Water Ice.*, Icarus, 336, 113455, doi: 10.1016/j.icarus.2019.113455

Deutsch, A. N., Head, J. W., & Neumann, G. A. *2019*, *Age Constraints of Mercury's Polar Deposits Suggest Recent Delivery of Ice*, Earth and Planetary Science Letters, 520, 26, doi: 10.1016/j.epsl.2019.05.027

Ehlmann, B. L., Klima, R. L., Seybold, C. C., et al. *2022*, NASA's Lunar Trailblazer Mission: A Pioneering Small Satellite for Lunar Water and Lunar Geology, in 2022 IEEE Aerospace Conference (AERO) (Big Sky, MT, USA: IEEE), 1–14

Eugster, O. *1999*, *Chronology of Dimict Breccias and the Age of South Ray Crater aMhe Apollo 16 Site*, Meteoritics & Planetary Science, 34, 385, doi: 10/b5jgbw

Fa, W. *2013*, *Simulation for Ground Penetrating Radar (GPR) Study of the Subsurface Structure of the Moon*, Journal of Applied Geophysics, 99, 98, doi: 10.1016/j.jappgeo.2013.08.002

Farhat, M., Auclair-Desrotour, P., Boué, G., & Laskar, J. *2022*, *The Resonant Tidal Evolution of the Earth-Moon Distance*, Astronomy & Astrophysics, 665, L1, doi: 10.1051/0004-6361/202243445

Farmer, V. *1974*, *The Infrared Spectra of Minerals: Mineralogical Society*, London, Monograph, 4, 539

Farrell, W. M., Hurley, D. M., Poston, M. J., et al. *2019*, *The Young Age of the LAMP-observed Frost in Lunar Polar Cold Traps*, Geophysical Research Letters, 46, 8680, doi: 10.1029/2019GL083158

Fassett, C. I., Head, J. W., Smith, D. E., Zuber, M. T., & Neumann, G. A. *2011*, *Thickness of Proximal Ejecta from the Orientale Basin from Lunar Orbiter Laser Altimeter (LOLA) Data: Implications for Multi-Ring Basin Formation*, Geophysical Research Letters, 38, L17201, doi: 10.1029/2011GL048502

Feldman, W. C., Maurice, S., Lawrence, D. J., et al. *2001*, *Evidence for Water Ice near the Lunar Poles*, Journal of Geophysical Research: Planets, 106, 23231, doi: 10.1029/2000je001444

Feng, J., & Siegler, M. A. *2021*, *Reconciling the Infrared and Microwave Observations of the Lunar South Pole: A Study on Subsurface Temperature and Regolith Density*, Journal of Geophysical Research: Planets, 126, e2020JE006623, doi: 10/gm8m5r

Feng, J., Siegler, M. A., & Hayne, P. O. *2020*, *New Constraints on Thermal and Dielectric Properties of Lunar Regolith from LRO Diviner and CE-2 Microwave Radiometer*, Journal of Geophysical Research: Planets, 125, doi: 10/gm9x6m

Fernandes, V., & Artemieva, N. *2012*, *Impact Ejecta Temperature Profile on the Moon—What Are the Effects on the Ar-Ar Dating Method?*, Lunar and Planetary Science Conference, 1367

Fisher, E. A., Lucey, P. G., Lemelin, M., et al. *2017*, *Evidence for Surface Water Ice in the Lunar Polar Regions Using Reflectance Measurements from the Lunar Orbiter Laser Altimeter and Temperature Measurements from the Diviner Lunar Radiometer Experiment*, Icarus, 292, 74, doi: 10.1016/j.icarus.2017.03.023

Gaddis, L. R., Boardman, J., Malaret, E., et al. *2016*, *Status of Restoring Moon Mineralogy Mapper Data to Full Spatial and Photometric Accuracy*, Lunar and Planetary Science Conference, doi: 10/cnn2h6

Gault, D. E., Hörz, F., Brownlee, D. E., et al. *1974*, *Mixing of the Lunar Regolith*, Lunar Science Conference, 3, 2365

Ghent, R. R., Hayne, P. O., Bandfield, J. L., et al. *2014*, *Constraints on the Recent Rate of Lunar Ejecta Breakdown and Implications for Crater Ages*, Geology, 42, 1059, doi: 10/f6rgdj

Gillies, S., et al. *2013*, Rasterio: Geospatial Raster I/O for Python Programmers

Gladstone, G. R., Retherford, K. D., Egan, A. F., et al. *2012*, *Far-Ultraviolet Reflectance Properties of the Moon's Permanently Shadowed Regions*, Journal of Geophysical Research: Planets, 117, E00H04, doi: 10.1029/2011JE003913

Glotch, T. D., Bandfield, J. L., Lucey, P. G., et al. *2015*, *Formation of Lunar Swirls by Magnetic Field Standoff of the Solar Wind.*, Nature Communications, 6, 6189, doi: 10/f63h28

Goswami, J., & Annadurai, M. *2009*, *Chandrayaan-1: India's First Planetary Science Mission to the Moon*, Current science, 486

Green, R. O., Pieters, C., Mouroulis, P., et al. *2011*, *The Moon Mineralogy Mapper (M 3) Imaging Spectrometer for Lunar Science: Instrument Description, Calibration, on-Orbit Measurements, Science Data Calibration and on-Orbit Validation*, Journal of Geophysical Research, 116, E00G19, doi: 10/d4vn8r

Grier, J. A., McEwen, A. S., Lucey, P. G., Milazzo, M., & Strom, R. G. *2001*, *Optical Maturity of Ejecta from Large Rayed Lunar Craters*, Journal of Geophysical Research, 106, 32847, doi: 10/cczr33

Grumpe, A., Wöhler, C., Berezhnoy, A. A., & Shevchenko, V. V. *2019*, *Time-of-Day-Dependent Behavior of Surficial Lunar Hydroxyl/Water: Observations and Modeling*, Icarus, 321, 486, doi: 10/gksdcw

Grün, E., Horanyi, M., & Sternovsky, Z. *2011*, *The Lunar Dust Environment*, Planetary and Space Science, 59, 1672, doi: 10.1016/j.pss.2011.04.005

Guo, D., Fa, W., Wu, B., Li, Y., & Liu, Y. *2021*, *Millimeter- to Decimeter-Scale Surface Roughness of the Moon at the Chang'e-4 Exploration Region*, Geophysical Research Letters, 48, doi: 10/gnr6b9

Hapke, B. *1973*, *Darkening of Silicate Rock Powders by Solar Wind Sputtering*, The Moon, 7, 342, doi: 10/b9bjp5

—. *2001*, *Space Weathering from Mercury to the Asteroid Belt*, Journal of Geophysical Research: Planets, 106, 10039, doi: 10/bzhsk6

Hardgrove, C., Starr, R., Lazbin, I., et al. *2020*, *The Lunar Polar Hydrogen Mapper CubeSat Mission*, IEEE Aerospace and Electronic Systems Magazine, 35, 54, doi: 10/ghfqnf

Harris, C. R., Millman, K. J., van der Walt, S. J., et al. *2020*, *Array Programming with NumPy*, Nature, 585, 357, doi: 10.1038/s41586-020-2649-2

Haruyama, J., Ohtake, M., Matsunaga, T., et al. *2008*, *Lack of Exposed Ice Inside Lunar South Pole Shackleton Crater*, Science, 322, 938, doi: 10.1126/science.1164020

Hayne, P. O., Aharonson, O., & Schörghofer, N. *2021*, *Micro Cold Traps on the Moon*, Nature Astronomy, 5, 169, doi: 10.1038/s41550-020-1198-9

Hayne, P. O., Osterman, D. P., Donaldson Hanna, K., & Paige, D. A. *2019*, *A Compact Instrument for Mineralogical and Thermophysical Studies of the Moon from the Lunar Surface*, American Geophysical Union Fall Meeting, 2019, P31C

Hayne, P. O., Hendrix, A., Sefton-Nash, E., et al. *2015*, *Evidence for Exposed Water Ice in the Moon's South Polar Regions from Lunar Reconnaissance Orbiter Ultraviolet Albedo and Temperature Measurements*, Icarus, 255, 58, doi: 10/f7dvw3

Hayne, P. O., Bandfield, J. L., Siegler, M. A., et al. *2017*, *Global Regolith Thermophysical Properties of the Moon From the Diviner Lunar Radiometer Experiment*, Journal of Geophysical Research: Planets, 122, 2371, doi: 10/gcv52c

Head, J. W., Wilson, L., Deutsch, A. N., Rutherford, M. J., & Saal, A. E. *2020*, *Volcanically Induced Transient Atmospheres on the Moon: Assessment of Duration, Significance, and Contributions to Polar Volatile Traps*, Geophysical Research Letters, 47, doi: 10.1029/2020GL089509

Helfenstein, P., & Shepard, M. K. *1999*, *Submillimeter-Scale Topography of the Lunar Regolith*, Icarus, 141, 107, doi: 10.1006/icar.1999.6160

Hemingway, D. J., Garrick-Bethell, I., & Kreslavsky, M. A. *2015*, *Latitudinal Variation in Spectral Properties of the Lunar Maria and Implications for Space Weathering*, Icarus, 261, 66, doi: 10/gksdcz

Hendrix, A. R., Hurley, D. M., Farrell, W. M., et al. *2019*, *Diurnally Migrating Lunar Water: Evidence From Ultraviolet Data*, Geophysical Research Letters, 46, 2417, doi: 10.1029/2018GL081821

Hermalyn, B. *2012*, *Scouring the Surface: Ejecta Dynamics and the LCROSS Impact Event*, Icarus, 218, 654, doi: 10.1016/j.icarus.2011.12.025

Hess, N. C. L., Carlson, D. J., Inder, J. D., et al. *2016*, *Python for Data Analysis*, Lunar and Planetary Science Conference, 65, 2208

Hiesinger, H., Van Der Bogert, C. H., Pasckert, J. H., et al. *2012*, *How Old Are Young Lunar Craters?*, Journal of Geophysical Research: Planets, 117, doi: 10/c8hq9f

Honniball, C. I., Lucey, P. G., Arredondo, A., Reach, W. T., & Malaret, E. R. *2022*, *Regional Map of Molecular Water at High Southern Latitudes on the Moon Using 6 Mm Data From the Stratospheric Observatory for Infrared Astronomy*, Geophysical Research Letters, 49, doi: 10.1029/2022GL097786

Honniball, C. I., Lucey, P. G., Ferrari-Wong, C. M., et al. *2020*, *Telescopic Observations of Lunar Hydration: Variations and Abundance*, Journal of Geophysical Research: Planets, doi: 10/gksdc2

Hörz, F., Gall, H., Hüttner, R., & Oberbeck, V. *1977*, Shallow Drilling in the 'Bunte Breccia' Impact Deposits, Ries Crater, Germany, in Impact and Explosion Cratering: Planetary and Terrestrial Implications, 425–448

Hörz, F., Ostertag, R., & Rainey, D. A. *1983*, *Bunte Breccia of the Ries: Continuous Deposits of Large Impact Craters*, Reviews of Geophysics, 21, 1667, doi: 10.1029/rg021i008p01667

Housley, R. M., Grant, R. W., & Paton, N. *1973*, *Origin and Characteristics of Excess Fe Metal in Lunar Glass Welded Aggregates*, Lunar Science Conference, 4, 2737

Hoyer, S., & Hamman, J. *2017*, *Xarray: N-D Labeled Arrays and Datasets in Python*, Journal of Open Research Software, 5, 10, doi: 10.5334/jors.148

Hunter, J. D. *2007*, *Matplotlib: A 2D Graphics Environment*, Computing in Science & Engineering, 9, 90, doi: 10.1109/MCSE.2007.55

Hurley, D. M., Cook, J. C., Retherford, K. D., et al. *2017*, *Contributions of Solar Wind and Micrometeoroids to Molecular Hydrogen in the Lunar Exosphere*, Icarus, 283, 31, doi: 10.1016/j.icarus.2016.04.019

Igami, Y., Muto, S., Takigawa, A., et al. *2021*, *Structural and Chemical Modifications of Oxides and OH Generation by Space Weathering: Electron Microscopic/Spectroscopic Study of Hydrogen-Ion-Irradiated Al2O3*, Geochimica et Cosmochimica Acta, 315, 61, doi: 10.1016/j.gca.2021.09.031

Jacobs, T. D. B., Junge, T., & Pastewka, L. *2017*, *Quantitative Characterization of Surface Topography Using Spectral Analysis*, Surface Topography: Metrology and Properties, 5, 013001, doi: 10.1088/2051-672X/aa51f8

Jeffers, S., Manley, S., Bailey, M., & Asher, D. *2001*, *Near-Earth Object Velocity Distributions and Consequences for the Chicxulub Impactor*, Monthly Notices of the Royal Astronomical Society, 327, 126, doi: 10.1046/j.1365-8711.2001.04747.x

Johnson, B. C., Collins, G. S., Minton, D. A., et al. *2016*, *Spherule Layers, Crater Scaling Laws, and the Population of Ancient Terrestrial Impactors*, Icarus, 271, 350, doi: 10/f8hv8f

Jordan, A., Shusterman, M., & Tai Udovicic, C. *2022*, *Modeling the Production of Submicroscopic Iron in the Lunar Highlands*, Icarus, 387, 115184, doi: 10.1016/j.icarus.2022.115184

Joy, K. H., Zolensky, M. E., Nagashima, K., et al. *2012*, *Direct Detection of Projectile Relics from the End of the Lunar Basin–Forming Epoch*, Science, 336, 1426, doi: 10.1126/science.1219633

Keller, L. P., & Clemett, S. J. *2001*, *Formation of Nanophase Iron in the Lunar Regolith*, Lunar and Planetary Science Conference, 2097

Keller, L. P., & McKay, D. S. *1993*, *Discovery of Vapor Deposits in the Lunar Regolith*, Science, 261, 1305, doi: 10/fhsrd4

—. *1997*, *The Nature and Origin of Rims on Lunar Soil Grains*, Geochimica et Cosmochimica Acta, 61, 2331, doi: 10/fmb5w5

Keller, L. P., & Zhang, S. *2015*, *Rates of Space Weathering in Lunar Soils*, Laboratory Experiments and Sample Analysis Workshop, 1878, 2056

Kieffer, H. H. *2013*, *Thermal Model for Analysis of Mars Infrared Mapping*, Journal of Geophysical Research: Planets, 118, 451, doi: 10.1029/2012JE004164

Kloos, J. L., Moores, J. E., Sangha, J., Nguyen, T. G., & Schorghofer, N. *2019*, *The Temporal and Geographic Extent of Seasonal Cold Trapping on the Moon*, Journal of Geophysical Research: Planets, 124, 1935, doi: 10.1029/2019je006003

Kornuta, D., Abbud-Madrid, A., Atkinson, J., et al. *2019*, *Commercial Lunar Propellant Architecture: A Collaborative Study of Lunar Propellant Production*, REACH, 13, 100026, doi: 10.1016/j.reach.2019.100026

Korycansky, D. G., Plesko, C. S., Jutzi, M., Asphaug, E., & Colaprete, A. *2009*, *Predictions for the LCROSS Mission*, Meteoritics & Planetary Science, 44, 603, doi: 10.1111/j.1945-5100.2009.tb00755.x

Kring, D. A. *1995*, *The Dimensions of the Chicxulub Impact Crater and Impact Melt Sheet*, Journal of Geophysical Research, 100, 16979, doi: 10.1029/95JE01768

—. *2005*, *Hypervelocity Collisions into Continental Crust Composed of Sediments and an Underlying Crystalline Basement: Comparing the Ries (∼24 Km) and Chicxulub (∼180 Km) Impact Craters*, Geochemistry, 65, 1, doi: 10.1016/j.chemer.2004.10.003

—. *2007*, *Guidebook to the Geology of Barringer Meteorite Crater, Arizona (Aka Meteor Crater), Lunar and Planetary Institute, Houston TX.*, LPI Contribution

—. *2020*, *Exploring the Consequences of Ballistic Sedimentation on Potential South Polar Ice Deposits on the Moon*, European Lunar Symposium

Kuiper, G. P. *1952*, *The Atmospheres of the Earth and Planets.*, Chicago

Landis, M. E., Hayne, P. O., Williams, J.-P., Greenhagen, B. T., & Paige, D. A. *2022*, *Spatial Distribution and Thermal Diversity of Surface Volatile Cold Traps at the Lunar Poles*, The Planetary Science Journal, 3, 39, doi: 10.3847/PSJ/ac4585

Laura, J., Hare, T. M., & Gaddis, L. R. *2013*, *Using Python, an Interactive Open-Source Programming Language, for Planetary Data Processing*, Lunar and Planetary Science Conference, doi: 10/gksdc7

Lawrence, D. J., Feldman, W. C., Elphic, R. C., et al. *2006*, *Improved Modeling of Lunar Prospector Neutron Spectrometer Data: Implications for Hydrogen Deposits at the Lunar Poles*, Journal of Geophysical Research, 111, E08001, doi: 10.1029/2005JE002637

Lemelin, M., Lucey, P. G., Gaddis, L. R., Hare, T., & Ohtake, M. *2016*, *Global Map Products from the Kaguya Multiband Imager at 512 Ppd: Minerals, FeO, and OMAT*, Lunar and Planetary Science Conference

Li, S., Lucey, P. G., Milliken, R. E., et al. *2018*, *Direct Evidence of Surface Exposed Water Ice in the Lunar Polar Regions.*, Proceedings of the National Academy of Sciences of the United States of America, 115, 8907, doi: 10/gd75rh

Li, S., & Milliken, R. E. *2017*, *Water on the Surface of the Moon as Seen by the Moon Mineralogy Mapper: Distribution, Abundance, and Origins*, Science Advances, 3, e1701471, doi: 10/gbxnkv

Liu, J., Sharp, M., Ash, R., Kring, D., & Walker, R. *2015*, *Diverse Impactors in Apollo 15 and 16 Impact Melt Rocks: Evidence from Osmium Isotopes and Highly Siderophile Elements*, Geochimica et Cosmochimica Acta, 155, 122, doi: 10.1016/j.gca.2015.02.004

Liu, J., Liu, B., Ren, X., et al. *2022*, *Evidence of Water on the Lunar Surface from Chang'E-5 in-Situ Spectra and Returned Samples*, Nature Communications, 13, 3119, doi: 10.1038/s41467-022-30807-5

Liu, T., Michael, G., Wünnemann, K., Becker, H., & Oberst, J. *2020*, *Lunar Megaregolith Mixing by Impacts: Spatial Diffusion of Basin Melt and Its Implications for Sample Interpretation*, Icarus, 339, 113609, doi: 10.1016/j.icarus.2019.113609

Liu, Y., Guan, Y., Zhang, Y., et al. *2012*, *Direct Measurement of Hydroxyl in the Lunar Regolith and the Origin of Lunar Surface Water*, Nature Geoscience, 5, 779, doi: 10.1038/ngeo1601

Loeffler, M. J., Dukes, C. A., & Baragiola, R. A. *2009*, *Irradiation of Olivine by 4 keV He+: Simulation of Space Weathering by the Solar Wind*, Journal of Geophysical Research: Planets, 114, E03003, doi: 10/cdm8hp

Losiak, A., Wilhelms, D., Byrne, C., et al. *2015*, *A New Lunar Impact Crater Database, Updated by Ohman, T., 2015.*, Lunar and Planetary Science Conference, 1532

Lucey, P. G., Blewett, D. T., & Hawke, B. R. *1998*, *Mapping the FeO and TiO2 Content of the Lunar Surface with Multispectral Imagery*, Journal of Geophysical Research: Planets, 103, 3679, doi: 10/c8dxq2

Lucey, P. G., Costello, E. S., Hurley, D. M., et al. *2020*, *Relative Magnitudes of Water Sources to the Lunar Poles*, Lunar and Planetary Science Conference, 2319

Lucey, P. G., & Noble, S. K. *2008*, *Experimental Test of a Radiative Transfer Model of the Optical Effects of Space Weathering*, Icarus, 197, 348, doi: 10/dmzgmm

Lucey, P. G., & Riner, M. A. *2011*, *The Optical Effects of Small Iron Particles That Darken but Do Not Redden: Evidence of Intense Space Weathering on Mercury*, Icarus, 212, 451, doi: 10/djx697

Lucey, P. G., Petro, N., Hurley, D. M., et al. *2021*, *Volatile Interactions with the Lunar Surface*, Geochemistry, 125858, doi: 10.1016/j.chemer.2021.125858

Luchsinger, K., Chanover, N., & Strycker, P. *2021*, *Water within a Permanently Shadowed Lunar Crater: Further LCROSS Modeling and Analysis*, Icarus, 354, 114089, doi: 10.1016/j.icarus.2020.114089

Malaret, E., Battisti, A., & Gaddis, L. *2019*, *2019 Status of Geometric Restoration of Moon Mineralogy Mapper Data*, Lunar and Planetary Science Conference, doi: 10/cnn2h6

Malphrus, B. K., Brown, K. Z., Garcia, J., et al. *2019*, *The Lunar IceCube EM-1 Mission: Prospecting the Moon for Water Ice*, IEEE Aerospace and Electronic Systems Magazine, 34, 6, doi: 10/gksddc

Mazarico, E., Neumann, G., Smith, D., Zuber, M., & Torrence, M. *2011*, *Illumination Conditions of the Lunar Polar Regions Using LOLA Topography*, Icarus, 211, 1066, doi: 10.1016/j.icarus.2010.10.030

Mazrouei, S., Ghent, R. R., Bottke, W. F., Parker, A. H., & Gernon, T. M. *2019*, *Earth and Moon Impact Flux Increased at the End of the Paleozoic*, Science, 363, 253, doi: 10/czs2

McCubbin, F. M., Steele, A., Hauri, E. H., et al. *2010*, *Nominally Hydrous Magmatism on the Moon*, Proceedings of the National Academy of Sciences, 107, 11223, doi: 10.1073/pnas.1006677107

McFadden, J., Garrick-Bethell, I., Sim, C. K., Kim, S. S., & Hemingway, D. *2019*, *Iron Content Determines How Space Weathering Flux Variations Affect Lunar Soils*, Icarus, 333, 323, doi: 10/gksddf

McGetchin, T. R., Settle, M., & Head, J. W. *1973*, *Radial Thickness Variation in Impact Crater Ejecta: Implications for Lunar Basin Deposits*, Earth and Planetary Science Letters, 20, 226, doi: 10/fbk55q

McIntosh, I. M., Nichols, A. R., Tani, K., & Llewellin, E. W. *2017*, *Accounting for the Species-Dependence of the 3500 Cm^{-1} H_2O_t Infrared Molar Absorptivity Coefficient: Implications for Hydrated Volcanic Glasses*, American Mineralogist, 102, 1677, doi: 10.2138/am-2017-5952CCBY

McKay, D. S., Heiken, G. H., Taylor, R. M., et al. *1972*, *Apollo 14 Soils: Size Distribution and Particle Types*, Lunar and Planetary Science Conference, 3, 983

McLain, J. L., Loeffler, M. J., Farrell, W. M., et al. *2021*, *Hydroxylation of Apollo 17 Soil Sample 78421 by Solar Wind Protons*, Journal of Geophysical Research: Planets, 126, doi: 10.1029/2021JE006845

Melosh, H. J. *1989*, *Impact Cratering: A Geologic Process*, New York: Oxford University Press; Oxford: Clarendon Press, 49, 245, doi: 10/dkrz9r

Miller, R. S., Lawrence, D. J., & Hurley, D. M. *2014*, *Identification of Surface Hydrogen Enhancements within the Moon's Shackleton Crater*, Icarus, 233, 229, doi: 10.1016/j.icarus.2014.02.007

Miller, R. S., Nerurkar, G., & Lawrence, D. J. *2012*, *Enhanced Hydrogen at the Lunar Poles: New Insights from the Detection of Epithermal and Fast Neutron Signatures: NEW INSIGHTS INTO LUNAR HYDROGEN*, Journal of Geophysical Research: Planets, 117, n/a, doi: 10.1029/2012JE004112

Miyakawa, T. *2020*, *No Raw Data, No Science: Another Possible Source of the Reproducibility Crisis*, Molecular Brain, 13, 24, s13041, doi: 10.1186/s13041-020-0552-2

Moon, S., Paige, D. A., Siegler, M. A., & Russell, P. S. *2021*, *Geomorphic Evidence for the Presence of Ice Deposits in the Permanently Shadowed Regions of Scott-E Crater on the Moon*, Geophysical Research Letters, 48, doi: 10.1029/2020GL090780

Moores, J. E. *2016*, *Lunar Water Migration in the Interval between Large Impacts: Heterogeneous Delivery to Permanently Shadowed Regions, Fractionation, and Diffusive Barriers: PSR Ballistic Migration Heterogeneity*, Journal of Geophysical Research: Planets, 121, 46, doi: 10.1002/2015je004929

Morota, T., Haruyama, J., Miyamoto, H., et al. *2009*, *Formation Age of the Lunar Crater Giordano Bruno*, Meteoritics & Planetary Science, 44, 1115, doi: 10/bfjtrv

Morris, R. *1980*, *Origins and Size Distribution of Metallic Iron Particles in the Lunar Regolith*, Lunar and Planetary Science Conference, 1697

Moses, J. I., Rawlins, K., Zahnle, K., & Dones, L. *1999*, *External Sources of Water for Mercury's Putative Ice Deposits*, Icarus, 137, 197, doi: 10.1006/icar.1998.6036

NAS, Committee on Toward an Open Science Enterprise, Board on Research Data and Information, & Policy and Global Affairs. 2018, Open Science by Design: Realizing a Vision for 21st Century Research (Washington, D.C.: National Academies Press), 25116, doi: 10.17226/25116

Needham, D. H., & Kring, D. A. *2017*, *Lunar Volcanism Produced a Transient Atmosphere around the Ancient Moon*, Earth and Planetary Science Letters, 478, 175, doi: 10.1016/j.epsl.2017.09.002

Neish, C. D., Bussey, D. B. J., Spudis, P., et al. *2011*, *The Nature of Lunar Volatiles as Revealed by Mini-RF Observations of the LCROSS Impact Site*, Journal of Geophysical Research: Planets, 116, doi: 10.1029/2010JE003647

Nelson, D. M., Koeber, S. D., Daud, K., et al. *2014*, *Mapping Lunar Maria Extents and Lobate Scarps Using LROC Image Products*, Lunar and Planetary Science Conference, 85281, 2861

Nettles, J. W., Staid, M., Besse, S., et al. *2011*, *Optical Maturity Variation in Lunar Spectra as Measured by Moon Mineralogy Mapper Data*, Journal of Geophysical Research: Planets, 116, E00G17, doi: 10/df53cw

Neukum, G., Ivanov, B. A., & Hartmann, W. K. *2001*, *Cratering Records in the Inner Solar System in Relation to the Lunar Reference System*, Space Science Reviews, 96, 55, doi: 10/cf54nf

Neumann, G. A., Zuber, M. T., Wieczorek, M. A., et al. *2015*, *Lunar Impact Basins Revealed by Gravity Recovery and Interior Laboratory Measurements*, Science Advances, 1, e1500852, doi: 10.1126/sciadv.1500852

Noble, S. K., Pieters, C. M., & Keller, L. P. *2007*, *An Experimental Approach to Understanding the Optical Effects of Space Weathering*, Icarus, 192, 629, doi: 10/dvzngr

NRC, Committee on the Scientific Context for Exploration of the Moon, Space Studies Board, & Division on Engineering and Physical Sciences. 2007, The Scientific Context for Exploration of the Moon (Washington, D.C.: National Academies Press), 11954, doi: 10.17226/11954

Oberbeck, V. R. *1975*, *The Role of Ballistic Erosion and Sedimentation in Lunar Stratigraphy*, Reviews of Geophysics, 13, 337, doi: 10/bcxqfb

Oberst, J., Christou, A., Suggs, R., et al. *2012*, *The Present-Day Flux of Large Meteoroids on the Lunar Surface—A Synthesis of Models and Observational Techniques*, Planetary and Space Science, 74, 179, doi: 10.1016/j.pss.2012.10.005

Ohtake, M., Haruyama, J., Matsunaga, T., et al. *2008*, *Performance and Scientific Objectives of the SELENE (KAGUYA) Multiband Imager*, Earth, Planets and Space, 60, 257, doi: 10/gksddj

Ong, L., Asphaug, E. I., Korycansky, D., & Coker, R. F. *2010*, *Volatile Retention from Cometary Impacts on the Moon*, Icarus, 207, 578, doi: 10.1016/j.icarus.2009.12.012

Onorato, P. I. K., Uhlmann, D. R., & Simonds, C. H. *1978*, *The Thermal History of the Manicouagan Impact Melt Sheet, Quebec*, Journal of Geophysical Research, 83, 2789, doi: 10.1029/jb083ib06p02789

Orgel, C., Michael, G., Fassett, C. I., et al. *2018*, *Ancient Bombardment of the Inner Solar System: Reinvestigation of the "Fingerprints" of Different Impactor Populations on the Lunar Surface*, Journal of Geophysical Research: Planets, 123, 748, doi: 10.1002/2017je005451

Paige, D. A., Siegler, M. A., Zhang, J. A., et al. *2010a*, *Diviner Lunar Radiometer Observations of Cold Traps in the Moon's South Polar Region*, Science, 330, 479, doi: 10.1126/science.1187726

Paige, D. A., Foote, M. C., Greenhagen, B. T., et al. *2010b*, *The Lunar Reconnaissance Orbiter Diviner Lunar Radiometer Experiment*, Space Science Reviews, 150, 125, doi: 10/b7d6jr

Patterson, G. W., Stickle, A. M., Turner, F. S., et al. *2017*, *Bistatic Radar Observations of the Moon Using Mini-RF on LRO and the Arecibo Observatory*, Icarus, 283, 2, doi: 10.1016/j.icarus.2016.05.017

Perkel, J. *2016*, *Democratic Databases: Science on GitHub*, Nature, 538, 127, doi: 10.1038/538127a

Petro, N. E., & Pieters, C. M. *2004*, *Surviving the Heavy Bombardment: Ancient Material at the Surface of South Pole-Aitken Basin*, Journal of Geophysical Research: Planets, 109, doi: 10.1029/2003je002182

—. *2006*, *Modeling the Provenance of the Apollo 16 Regolith*, Journal of Geophysical Research, 111, E09005, doi: 10.1029/2005je002559

Pieters, C. M., & Noble, S. K. *2016*, *Space Weathering on Airless Bodies*, Journal of Geophysical Research: Planets, 121, 1865, doi: 10/f9cm7w

Pieters, C. M., Taylor, L. A., Noble, S. K., et al. *2000*, *Space Weathering on Airless Bodies: Resolving a Mystery with Lunar Samples*, Meteoritics & Planetary Science, 35, 1101, doi: 10/b5prx3

Pieters, C. M., Pieters, C. M., Boardman, J., et al. *2009*, *The Moon Mineralogy Mapper (M3) on Chandrayaan-1*, Current Science, 96, 500, doi: 10.2307/24105459

Pokorný, P., Janches, D., Sarantos, M., et al. *2019*, *Meteoroids at the Moon: Orbital Properties, Surface Vaporization, and Impact Ejecta Production*, Journal of Geophysical Research: Planets, doi: 10/gksddn

QGIS. *2021*, QGIS Geographic Information System, Open Source Geospatial Foundation

Reback, J., jbrockmendel, McKinney, W., et al. *2022*, Pandas-Dev/Pandas: Pandas 1.4.2, Zenodo, doi: 10.5281/zenodo.6408044

Rivkin, A. S., Davies, J. K., Johnson, J. R., et al. *2003*, *Hydrogen Concentrations on C-class Asteroids Derived from Remote Sensing*, Meteoritics & Planetary Science, 38, 1383, doi: 10.1111/j.1945-5100.2003.tb00321.x

Robinson, M. S., Brylow, S. M., Tschimmel, M., et al. *2010*, *Lunar Reconnaissance Orbiter Camera (LROC) Instrument Overview*, Space Science Reviews, 150, 81, doi: 10/ckjthh

Roush, T. L., Colaprete, A., Cook, A., et al. *2020*, *NIRVSS Aboard CLPS*, Lunar and Planetary Science Conference

Rubanenko, L., Schorghofer, N., Greenhagen, B. T., & Paige, D. A. *2020*, *Equilibrium Temperatures and Directional Emissivity of Sunlit Airless Surfaces With Applications to the Moon*, Journal of Geophysical Research: Planets, 125, doi: 10/gksdds

Rubanenko, L., Venkatraman, J., & Paige, D. A. *2019*, *Thick Ice Deposits in Shallow Simple Craters on the Moon and Mercury*, Nature Geoscience, 12, 597, doi: 10.1038/s41561-019-0405-8

Saal, A. E., Hauri, E. H., Cascio, M. L., et al. *2008*, *Volatile Content of Lunar Volcanic Glasses and the Presence of Water in the Moon's Interior*, Nature, 454, 192, doi: 10.1038/nature07047

Salih, A. L., Grumpe, A., Wöhler, C., & Hiesinger, H. *2016*, *Construction of an Age Map of the Region Around the Young Lunar Crater Hell Q*, International Journal of Simulation Systems, Science, and Technology, 17, doi: 10/gksddt

Sasaki, S., Nakamura, K., Hamabe, Y., Kurahashi, E., & Hiroi, T. *2001*, *Production of Iron Nanoparticles by Laser Irradiation in a Simulation of Lunar-like Space Weathering*, Nature, 410, 555, doi: 10/cv5p4t

Schorghofer, N., & Aharonson, O. *2014*, *The Lunar Thermal Ice Pump*, The Astrophysical Journal, 788, 169, doi: 10.1088/0004-637x/788/2/169

Schorghofer, N., & Williams, J.-P. *2020*, *Mapping of Ice Storage Processes on the Moon with Time-dependent Temperatures*, The Planetary Science Journal, 1, 54, doi: 10.3847/psj/abb6ff

Schultz, P. H., Hermalyn, B., Colaprete, A., et al. *2010*, *The LCROSS Cratering Experiment*, Science, 330, 468, doi: 10.1126/science.1187454

SDMWG. *2018*, NASA Science Mission Directorate's Strategy for Data Management and Computing for Groundbreaking Science 2019-2024, Tech. rep., Strategic Data Management Working Group (SDMWG)

Sharpton, V. L. *2014*, *Outcrops on Lunar Crater Rims: Implications for Rim Construction Mechanisms, Ejecta Volumes and Excavation Depths: Outcrops Constrain Crater Rim Components*, Journal of Geophysical Research: Planets, 119, 154, doi: 10.1002/2013JE004523

Shepard, M. K., Brackett, R. A., & Arvidson, R. E. *1995*, *Self-Affine (Fractal) Topography: Surface Parameterization and Radar Scattering*, Journal of Geophysical Research, 100, 11709, doi: 10.1029/95JE00664

Shoemaker, E. M., & Hackman, R. J. *1962*, Stratigraphic Basis for a Lunar Time Scale, in The Moon, ed. Z. Kopal & Z. K. Mikhailov, Vol. 14 (IAU Symposium 14), 289–300

Siegler, M., Paige, D. A., Williams, J.-P., & Bills, B. *2015*, *Evolution of Lunar Polar Ice Stability*, Icarus, 255, 78, doi: 10.1016/j.icarus.2014.09.037

Sim, C. K., Kim, S. S., Lucey, P. G., Garrick-Bethell, I., & Choi, Y. J. *2017*, *Asymmetric Space Weathering on Lunar Crater Walls*, Geophysical Research Letters, 44, 11,273, doi: 10/gctbr6

Speyerer, M. E. J., Robinson, M. S., & Denevi, B. W. *2011*, *Lunar Reconnaissance Orbiter Camera Global Morphological Map of the Moon*, Lunar and Planetary Science Conference

Spudis, P. D., Nozette, S., Lichtenberg, C., et al. *1998*, *The clementine bistatic radar experiment: Evidence for ice on the moon*, Solar System Research, 32, 17

Spudis, P. D., Bussey, D. B. J., Baloga, S. M., et al. *2013*, *Evidence for Water Ice on the Moon: Results for Anomalous Polar Craters from the LRO Mini-RF Imaging Radar: EVIDENCE FOR ICE ON THE MOON*, Journal of Geophysical Research: Planets, 118, 2016, doi: 10.1002/jgre.20156

Stacy, N. J. S., Campbell, D. B., & Ford, P. G. *1997*, *Arecibo Radar Mapping of the Lunar Poles: A Search for Ice Deposits*, Science, 276, 1527, doi: 10.1126/science.276.5318.1527

Starukhina, L. *2001*, *Water Detection on Atmosphereless Celestial Bodies: Alternative Explanations of the Observations*, Journal of Geophysical Research: Planets, 106, 14701, doi: 10.1029/2000JE001307

Stolper, E. *1982*, *Water in Silicate Glasses: An Infrared Spectroscopic Study*, Contributions to Mineralogy and Petrology, 81, 1, doi: 10.1007/BF00371154

Suggs, R., Moser, D., Cooke, W., & Suggs, R. *2014*, *The Flux of Kilogram-Sized Meteoroids from Lunar Impact Monitoring*, Icarus, 238, 23, doi: 10.1016/j.icarus.2014.04.032

Sunshine, J. M., Farnham, T. L., Feaga, L. M., et al. *2009*, *Temporal and Spatial Variability of Lunar Hydration as Observed by the Deep Impact Spacecraft.*, Science, 326, 565, doi: 10/bwhhjm

Svetsov, V., & Shuvalov, V. *2015*, *Water Delivery to the Moon by Asteroidal and Cometary Impacts*, Planetary and Space Science, 117, 444, doi: 10.1016/j.pss.2015.09.011

Tai Udovicic, C. *2017*, Craterpy: A Python Library for Impact Crater Data Science, doi: 10.5281/ZENODO.1009679

Tai Udovicic, C., Mazrouei, S., Ghent, R., & Costello, E. *2016*, *A Fresh Look at Aging Lunar Ejecta: Insights from Optical Maturity (OMAT) and Rock Abundance (RA)*, American Geophysical Union Fall Meeting

Tai Udovicic, C. J., Costello, E. S., Ghent, R. R., & Edwards, C. S. *2021a*, *New Constraints on the Lunar Optical Space Weathering Rate*, Geophysical Research Letters, 48, doi: 10/gmpfzn

Tai Udovicic, C. J., Frizzell, K. R., Luchsinger, K. M., Madera, A., & Paladino, T. G. *2022a*, MoonPIES: Moon Polar Ice and Ejecta Stratigraphy Model, Zenodo

—. *2022b*, Supplemental Data Sets for "Buried Ice Deposits in Lunar Polar Cold Traps Were Disrupted by Ballistic Sedimentation", Zenodo

Tai Udovicic, C. J., Haberle, C. W., Edwards, C. S., & Bandfield, J. L. *2021b*, Roughness, Zenodo, doi: 10.5281/ZENODO.5498165

Trang, D., & Lucey, P. G. *2019*, *Improved Space Weathering Maps of the Lunar Surface through Radiative Transfer Modeling of Kaguya Multiband Imager Data*, Icarus, 321, 307, doi: 10/gksdd3

Tye, A., Fassett, C., Head, J., et al. *2015*, *The Age of Lunar South Circumpolar Craters Haworth, Shoemaker, Faustini, and Shackleton: Implications for Regional Geology, Surface Processes, and Volatile Sequestration*, Icarus, 255, doi: 10.1016/j.icarus.2015.03.016

UNESCO. *2021*, Draft Text of the UNESCO Recommendation on Open Science, UNESCO Paris

van der Bogert, C. H., Hiesinger, H., Mcewen, A. S., et al. *2010*, *Discrepancies Between Crater Size-Frequency Distributions on Ejecta and Impact Melt Pools at Lunar Craters: An Effect of Differing Target Properties?*, Lunar and Planetary Science Conference, 2165

Van Rossum, G., & Drake, F. L. 2009, Python 3 Reference Manual (CreateSpace)

Vasavada, A. R., Bandfield, J. L., Greenhagen, B. T., et al. *2012*, *Lunar Equatorial Surface Temperatures and Regolith Properties from the Diviner Lunar Radiometer Experiment*, Journal of Geophysical Research: Planets, 117, n/a, doi: 10/gksdd4

Vasavada, A. R., Paige, D. A., & Wood, S. E. *1999*, *Near-Surface Temperatures on Mercury and the Moon and the Stability of Polar Ice Deposits*, Icarus, 141, 179, doi: 10/b9fhjd

Verma, P. A., Chauhan, M., & Chauhan, P. *2022*, *Lunar Surface Temperature Estimation and Thermal Emission Correction Using Chandrayaan-2 Imaging Infrared Spectrometer Data for H2O & OH Detection Using 3 Mm Hydration Feature*, Icarus, 383, 115075, doi: 10.1016/j.icarus.2022.115075

Vickery, A. *1986*, *Size-Velocity Distribution of Large Ejecta Fragments*, Icarus, 67, 224, doi: 10.1016/0019-1035(86)90105-3

Virtanen, P., Gommers, R., Oliphant, T. E., et al. *2020*, *SciPy 1.0: Fundamental Algorithms for Scientific Computing in Python*, Nature Methods, 17, 261, doi: 10.1038/s41592-019-0686-2

Warren, T., Curtis, R., Shirley, K., et al. *2021*, *Investigating the Thermal Infrared Emission Phase Function of the Lunar Surface Using the Diviner Lunar Radiometer*, Lunar and Planetary Science Conference, 1890

Watson, K., Murray, B. C., & Brown, H. *1961*, *The Behavior of Volatiles on the Lunar Surface*, Journal of Geophysical Research, 66, 3033, doi: 10/cgfh7n

Wehner, G. K. *1961*, *Sputtering Effects on the Moon's Surface*, ARS Journal, 31, 438, doi: 10/gksdfc

Whipple, F. L. *1950*, *A Comet Model. I. The Acceleration of Comet Encke*, The Astrophysical Journal, 111, 375, doi: 10.1086/145272

Wilcoski, A. X., Hayne, P. O., & Landis, M. E. *2021*, *Lunar Polar Water Ice Sourced from Ancient Volcanic Atmospheres*, Exploration Science Forum

Williams, J. P., Paige, D. A., Greenhagen, B. T., & Sefton-Nash, E. *2017*, *The Global Surface Temperatures of the Moon as Measured by the Diviner Lunar Radiometer Experiment*, Icarus, 283, 300, doi: 10/f9h629

Williams, J. P., Bandfield, J. L., Paige, D. A., et al. *2018*, *Lunar Cold Spots and Crater Production on the Moon*, Journal of Geophysical Research: Planets, 123, 2380, doi: 10/gfjqrq

Williams, J.-P., Greenhagen, B. T., Paige, D. A., et al. *2019*, *Seasonal Polar Temperatures on the Moon*, Journal of Geophysical Research: Planets, 124, 2505, doi: 10.1029/2019JE006028

Wöhler, C., Grumpe, A., Berezhnoy, A. A., et al. *2017*, *Temperature Regime and Water/Hydroxyl Behavior in the Crater Boguslawsky on the Moon*, Icarus, 285, 118, doi: 10/f9qz5b

Wolf, R., & Anders, E. *1980*, *Moon and Earth : Compositional Differences Inferred from Siderophiles, Volatiles, and Alkalis in Basalts*, Geochimica et Cosmochimica Acta, 44, 2111, doi: 10.1016/0016-7037(80)90208-2

Xie, M., Liu, T., & Xu, A. *2020*, *Ballistic Sedimentation of Impact Crater Ejecta: Implications for the Provenance of Lunar Samples and the Resurfacing Effect of Ejecta on the Lunar Surface*, Journal of Geophysical Research: Planets, 125, e2019JE006113, doi: 10.1029/2019je006113

Young, E. T., Becklin, E. E., Marcum, P. M., et al. *2012*, *Early Science with SOFIA, the Stratospheric Observatory for Infrared Astronomy*, The Astrophysical Journal, 749, L17, doi: 10.1088/2041-8205/749/2/L17

Zhu, C., Crandall, P. B., Gillis-Davis, J. J., et al. *2019*, *Untangling the Formation and Liberation of Water in the Lunar Regolith*, Proceedings of the National Academy of Sciences of the United States of America, 166, 11165, doi: 10/ggw3d6

Zuber, M. T., Head, J. W., Smith, D. E., et al. *2012*, *Constraints on the Volatile Distribution within Shackleton Crater at the Lunar South Pole*, Nature, 486, 378, doi: 10.1038/nature11216